MICROCOPY RESOLUTION TEST CHART

NATIONAL BUREAU OF STANDARDS-1963-A

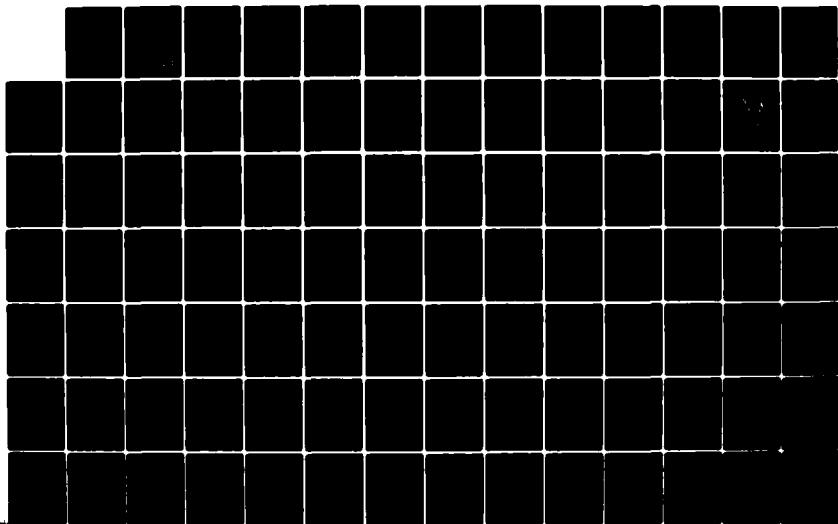AFGL-TR-82-0220

INFRARED RADIANCE STRUCTURE OF THE AURORA AND AIRGLOW

I.L. Kofsky
J. L. Barrett
L. McVay

PhotoMetrics, Inc.
4 Arrow Drive
Woburn, MA 01801

30 June 1982

Scientific Report No. 2

DTIC
ELECTE
JUL 1 8 1983
S
E
D

83 07 18 014

SECURITY CLASSIFICATION OF THIS PAGE (When Data Entered)

REPORT DOCUMENTATION PAGE		READ INSTRUCTIONS BEFORE COMPLETING FORM
1. REPORT NUMBER AFGL-TR-82-0220	2. GOVT ACCESSION NO. AD-A130 468	3. RECIPIENT'S CATALOG NUMBER
4. TITLE (and Subtitle) INFRARED RADIANCE STRUCTURE OF THE AURORA AND AIRGLOW		5. TYPE OF REPORT & PERIOD COVERED Scientific Report No. 2
		6. PERFORMING ORG. REPORT NUMBER PhM-TR-82-02
7. AUTHOR(s) I.L. Kofsky L. McVay J.L. Barrett		8. CONTRACT OR GRANT NUMBER(s) F19628-80-C-0134
9. PERFORMING ORGANIZATION NAME AND ADDRESS PhotoMetrics, Inc. 4 Arrow Drive Woburn, Massachusetts 01801		10. PROGRAM ELEMENT, PROJECT, TASK AREA & WORK UNIT NUMBERS 62101F 767011AF
11. CONTROLLING OFFICE NAME AND ADDRESS Air Force Geophysics Laboratory Hanscom AFB, Massachusetts 01731 Monitor/Robert E. Pierce/OPR		12. REPORT DATE 30 June 82
		13. NUMBER OF PAGES 168
14. MONITORING AGENCY NAME & ADDRESS(if different from Controlling Office)		15. SECURITY CLASS. (of this report) Unclassified
		15a. DECLASSIFICATION/DOWNGRADING SCHEDULE

16. DISTRIBUTION STATEMENT (of this Report)

Approved for public release; distribution unlimited

17. DISTRIBUTION STATEMENT (of the abstract entered in Block 20, if different from Report)

18. SUPPLEMENTARY NOTES

19. KEY WORDS (Continue on reverse side if necessary and identify by block number)

Aurora
Auroral Occurrence
Auroral Irregularities
Airglow Irregularities

Airglow
Infrared Backgrounds
Infrared Surveillance
micrometers

20. ABSTRACT (Continue on reverse side if necessary and identify by block number)

The data base on column intensity and spatial-temporal irregularity structure of $2\frac{1}{2}$ - 7 μm infrared auroral airglow radiations is reviewed, and models of occurrence of sky background clutter in sensor fields are specified. Probabilities and geographic location of auroral particle fluxes, energy conversion efficiencies and relaxation times after excitation, chemi-

DD FORM 1473   EDITION OF 1 NOV 65 IS OBSOLETE

Abstract 20. (continued)

luminescence and fluorescence spectrums of the important radiating species NO, CO_2, N_2 and NO^+ (at $\lesssim 10$ cm^{-1} resolution), characteristic power spectral densities of the fluctuations in input, and methods of calculating sight paths through the upper-atmospheric layers are compiled for use in the auroral model. The existing observations of recurring and episodic variations of hydroxyl vibrational-bands airglow are ordered into a global model of local-average OH 2.7 - $\sim 4\mu$m limb radiance and its inhomogeneity. Intensities of infrared airglows from NO, NO_2, and O_3 are calculated.

The statistical auroral oval defined by a geomagnetic field-disturbance index and magnetic time is taken as the location of occurrence of excitation by incoming electron fluxes (the effect of the proton component is found to be negligible). Hardness of the electrons' energy distribution is shown to have important effects on the noise spectrums and the requirements for information about flux structure. Major shortcomings in input data, which limit the completeness of the auroral model, are in the probabilities of energy deposition into near-limb sight paths making arbitrary angles with the geomagnetic latitude lines, the irregularity of this input power, and (for CO_2 and NO radiation) the statistics of wind shear-induced lateral transport of precursor species. Analysis of existing survey data, which are identified, would permit upgrading of the infrared background-distributions model.

Intensities of both glows depend critically on sight path length through the emitting atmospheric layers. As the average variation of hydroxyl zenith radiance is small, its limb brightness is a sharp maximum at readily-determined intercept latitudes-longitudes. The airglow model calculates expectation spectral radiances and their uncertainties as a function of solar zenith angle, latitude, season, phase of the solar cycle, and magnetic-storm and stratospheric-warming conditions. Amplitudes and frequencies of the spatial fluctuations are estimated from the brightness structure observed at incidence angles to the emitting layer between 10° and 90°; direct information about the statistics of irregularities at lower angles would improve the reliability of the airglow-clutter predictions.

FOREWORD

This report reviews the existing data on the occurrence
of short-wavelength infrared sky background clutter due to
aurora and airglow, and specifies models for calculating
occurrence-probability distributions. Section 1 relates these
non-equilibrium emissions to the thermal radiation from the
lower atmosphere. Section 2 discusses the geographic location
location and frequency of excitation of air by auroral particles
and the ensuing reaction processes that result in infrared radia-
ations, and develops a background-noise occurrence model of scope
commensurate with the available input data (Fig 23). In Section
3 the observations of airglow from hydroxyl molecules are ordered
into a global model of mean limb radiance and its fluctuation
structure (Fig 25). Information on $2-1/2 - 7\mu m$ glows from
the other infrared-active atmospheric species NO, NO_2 and O_3
is presented in two appendixes.

We have attempted to include enough basic information on
luminescence processes in the upper atmosphere to make the re-
port directly useful to designers of measurement systems. The
terminology of auroral radiation and morphology is explained;
a procedure for converting between the coordinate systems of
auroral occurrence and an optical measurement system is given;
example spectral radiance distributions are shown, in engineering
units; and references clarifying (and justifying) all critical
ideas are presented. The report is written at the technical
standard of the geophysics and aerochemistry communities, toward
stimulating thought on how best to improve the input data that
determine reliability and resolution of the models of infrared
clutter.

Accession For	
NTIS GRA&I	☒
DTIC TAB	☐
Unannounced	☐
Justification	
By	
Distribution/	
Availability Codes	
Dist	Avail and/or Special
A	

TABLE OF CONTENTS

5

LIST OF ILLUSTRATIONS

ILLUSTRATIONS (concluded)

LIST OF TABLES

1. Introduction

We review in this report the existing data base on spatial
and temporal structure of the natural infrared aurora and air-
glow, and specify from this information models of the occurrence
of their radiant intensities and inhomogeneities. Definition of
the global distribution of background clutter from the atmosphere
provides standardized, quantitative criteria for design of optical
measurements systems; specifically, the noise spectrums serve in
selecting the wavelength sensitivity bands, spatial resolution,
signal integration times, background-suppression logic, and
other engineering factors that optimize system performance.
Additionally, real-time prediction of geophysical effects on
the sky's radiance -- in particular, the sporadic increases
and irregularities resulting from magnetospheric disturbances --
would permit future measurements systems to mitigate their
impact by changing operating parameters such as wavelength
band intervals.

Aurora (for the purposes of this report) is the luminosity
of high-altitude air resulting from impact excitation by charged
particles, principally electrons with energy near 5 kilo-electron
volts, that flow into the high-latitude atmosphere from the
magnetosphere. We define airglow to be the other non-thermal,
chemical reaction-induced radiations from the earth's upper
atmosphere, with the exceptions of resonant and fluorescent
scattering of sunlight and earthshine and of glows excited by
sporadic local events such as meteor trains and lightning strokes.
Unlike aurora, airglow is virtually never detectable by the
unaided eye because of its low radiance and contrast. The
energy source for airglow radiation is short wavelength photons
from the sun, which with their photoelectrons initiate the
reactions by ionizing and dissociating air molecules. Both

9

types of nonequilibrium emission originate from altitudes above about 70 km, where photochemistry plays an important part in determining the species concentrations and the low collision rates favor depopulation of excited states of molecules and atoms by emission of ultraviolet, visible, and infrared radiation.

1.1. Context of Auroral-Airglow Clutter Background

The relation of airglow and aurora to the other infrared backgrounds presented to a measurement platform by the earth's atmosphere and surface is illustrated schematically in Figure 1. In the troposphere and stratosphere ($<\sim 50$ km) the populations of excited states of the air molecules are controlled by collisions; that is, the radiational and kinetic temperatures of the gas are effectively the same. The spectral radiance of this thermal emission is determined by transport of radiation across the temperature and species-concentration profiles of the atmosphere. Vibration-rotation bands of minor permanent-dipole species, in particular H_2O and CO_2, play a prominent role in defining the infrared radiation field (as discussed in Section 1.4). Nadir-viewing high altitude sensors see also collisionally-excited radiation and resonant and fluorescent scattering from air species at higher altitudes, and solar photons scattered from molecules and aerosol at lower altitudes (and at some wavelengths, from the earth's surface), with an overlay of non-equilibrium molecular band and atomic line emissions from the upper mesosphere (~ 70 - 90 km) and thermosphere (>90 km).

As the tangent intercept of the sensor's field-of-view moves upward, these latter radiations in general contribute a larger fraction of the signal. The natural spatial and temporal irregularity of auroral-airglow emissions -- the topic reviewed in this report -- then plays an increasingly important part in determining the structure or "clutter" of the total atmospheric background.

10

Altitudes of emission of airglow, aurora, and thermal atmospheric radiations. Escape altitudes of major thermal-emission bands are shown at the left.

EARTH'S MAGNETIC FIELD

--- AURORA ---

CHEMILUMINESCENCE & FLUORESCENCE OF AIR SPECIES

-- EARTHSHINE SCATTERING --

-- AIRGLOW --

HYDROXYL CHEMILUMINESCENCE

-- THERMAL RADIATION --

ABSORPTION/EMISSION BY H_2O, CO_2, O_3, HNO_3, AEROSOLS.....

160 —
140 —
120 —
100 —
80 —
60 —
40 —
20 —

ALTITUDE, KM

CO_2 4.3μm

PENETRATION/ESCAPE ALTITUDE

H_2O/CO_2 2.7μm

BLACKBODY-RADIATING EARTH'S SURFACE
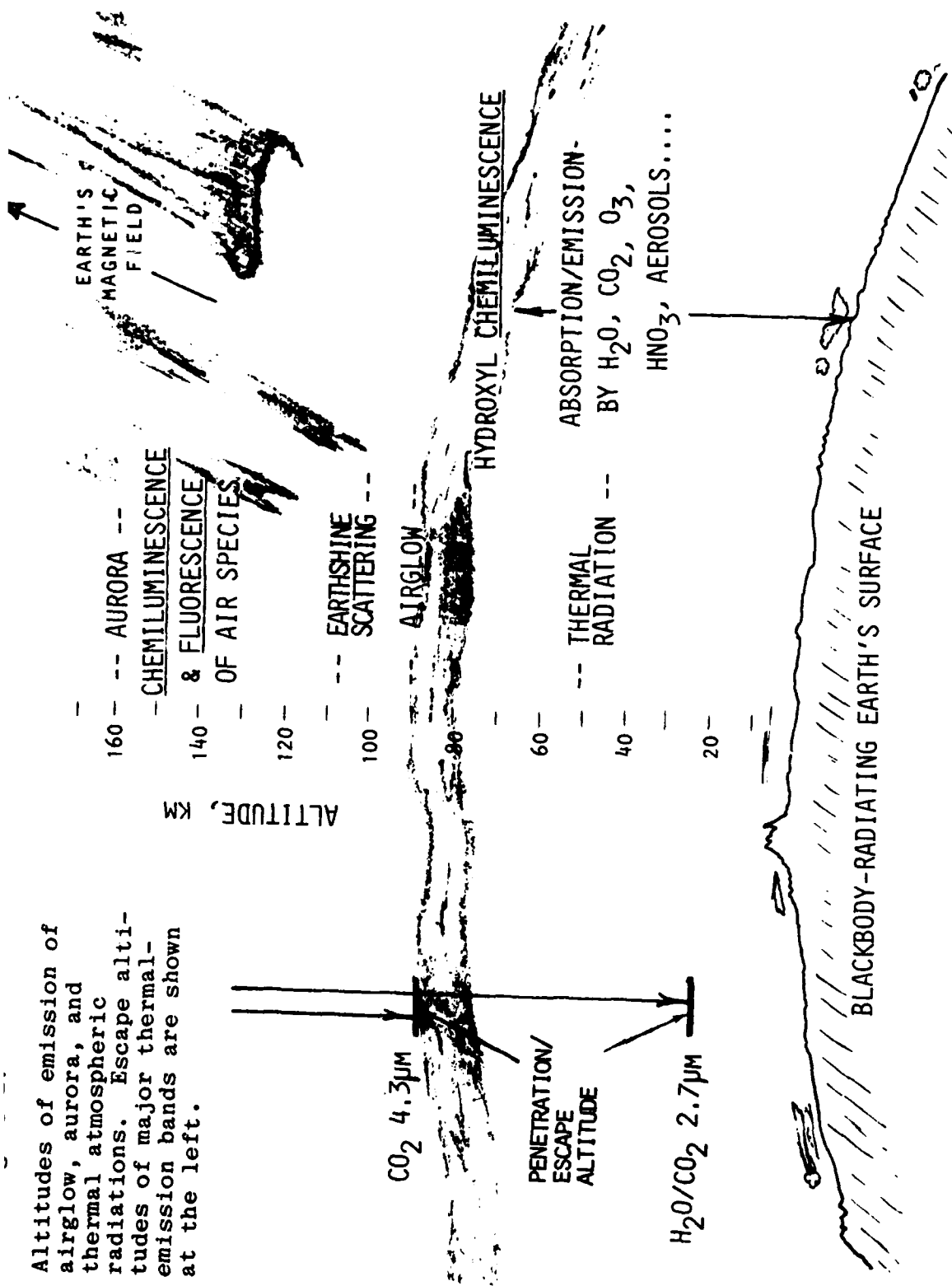
Air Force Geophysics Laboratory has developed computer models of the spatially- and temporally-averaged infrared spectral radiances near the earth's limb (Ref 1), and of the lower atmosphere under prespecified meteorological and instrument-pointing conditions (from LOWTRAN, Ref's 2, 3). These "thermal-emission" calculations omit excitation by auroral particles and all but one of the airglow reactions from the physical processes that populate infrared-emitting states. The limb model (Ref's 1, 4) considers resonant and fluorescent scattering of photons from the sun and earth-lower atmosphere -- which we shall henceforth include with the collisional excitation --, and the airglow from O_3 molecules in a band centered at $9.6\mu m$ (1040 cm^{-1}) produced by recombination of O with O_2. Auroral particle input has some influence on both types of radiation, as dissociation and excitation of ambient molecules increases the concentrations of scattering and reactive species such as NO (this issue of effect of aurora on the "thermal" radiance is not explicitly treated in this report).

Little information exists on the variability in space and time of the atmosphere's thermal infrared radiations. We note that the noise statistics of limb radiances at low and middle latitudes will be measured under a future USAF program, and that data on the lower atmosphere's nadir-hemisphere infrared radiance fluctuations are becoming available from balloon and other high-. altitude measurement platforms.

1.2. Scope of This Report

The scope of the assessment of sky background clutter reported here is outlined in Table 1. As noted, we review 1) what we defined above as airglow and 2) the radiations emitted within a few minutes of the excitation, ionization, and dissociation of air by auroral particles. We have not considered

Table 1. Scope of Assessment of Auroral/Airglow
Infrared Backgrounds

Radiation   Aurora
  Source   Chemiluminescence
                                        Fluorescence
                                        Airglow (chemiluminescence)

Wavelengths of $2\text{-}1/2$ to $7\mu m$
  Emission   (4000 to 1428 cm^{-1})

Resolution of   Spatial: 1 km, 1 km^2
  Typical Measurement   Temporal: 1 sec
                                        Spectral: 10 cm^{-1}
                                              ($0.007\mu m$ at $2\text{-}1/2\mu m$,
                                                $0.05\mu m$ at $7\mu m$)

View Projection   From exoatmospheric sensors

Solar Proton Events -- irradiation of the high-latitude thermo-
sphere, mesosphere, and even stratosphere by protons and other
very energetic charged particles that originate from the sun --,
as they produce essentially-unstructured and weak infrared back-
grounds (Ref 5). (SPE's also occur more rarely than aurora,
albeit over a larger geographic area and with longer persistence
of individual events.)

     We take _fluorescence_ of air to include, in addition
to the radiations from electronic and vibrational states that
are directly populated by impact of incoming particles, those
radiations excited by their energetic secondary electrons and
ultraviolet photons and the complex of secondary, tertiary,...

13

processes (recombination reactions, collisional excitation transfer, cascade radiation) that takes place within a few seconds of the initial deposition of the primary particles' kinetic energy. (We ignore radiation from longer-lived metastable states, as in practice it does not contribute to the infrared background clutter.) The $W^3\Delta_u \rightarrow B^3\pi_g$ (Wu-Benesch) bands of N_2, observed in an EXCEDE artificial-aurora experiment (Ref 6), are an example of an infrared fluorescence feature from high altitude (low pressure) air. Fluorescence at the shorter wavelengths to which the eye and photographic film (and photoemissive detectors) are sensitive is the most familiar feature of aurora, and is commonly used to investigate spatial-temporal distributions of particle input as well as many other aspects of auroral phenomenology.

Chemiluminescence is the conversion into radiation of the exothermicity of chemical reactions, which in the atmosphere involve species produced by the action of either auroral particles or energetic solar photons. Indirect chemiluminescence can also take place, the energy of an excited state being transferred to another atom or molecule. As an example, the reaction of H atoms with O_3 molecules (Section 3) produces vibrationally-excited OH radicals, which either radiate directly or collisionally transfer their energy (via vibrational excitation of N_2 molecules) to CO_2 molecules; which in turn can radiate at another (longer) wavelength. Chemiluminescence is differentiated from thermal emission by being due to conversion of chemical potential, rather than kinetic, energy; hence the initial distribution of vibrational and electronic upper states does not directly reflect the kinetic temperature of the emitting species. (Note that in general no hard and clear boundary exists between chemiluminescence and the slower secondary mechanisms that contribute to what we have called fluorescence, this mild ambiguity turns out to be of no practical importance.)

We have considered only the short- and medium-wavelength
infrared spectral region between 2-1/2 and 7μm (wavenumbers
4000-1428 cm^{-1}), in which high detector sensitivity can be
achieved with liquid-nitrogen cryocooling systems of weight and
lifetime compatible with the capabilities of certain classes of
measurement platforms. The methods developed here for charac-
terizing auroral and airglow background noise can of course also
be applied to the longer wavelength-infrared features, albeit
with less accuracy because their spectral yields are not as well
known (longward of 15μm in particular).

The minimum time and space scales of atmospheric varia-
bility and the measurement wavelength interval(s) have been
selected to illustrate conditions of most interest. We consider
a 1 kilometer footprint on the earth's atmosphere (3 x 10^{-5} radians
at geosynchronous altitude), and henceforth normalize background
radiances to 1 km^2 of radiating area. We take dwell or signal-
integration times down to 1 sec, and spectral widths to 10 wave-
numbers (0.007 and 0.05μm "filter widths" at the short- and
long-wavelength extremes of the infrared band considered). This
modest spectral resolution, which is derived from instrument-
design and intensity considerations, reduces the requirements
for extending analysis of the background spectrum to intervals
comparable to the separation between rotational lines in bands
vibration-rotation bands of atmospheric molecules.

The sight paths considered intercept the atmosphere
from satellite orbit, with emphasis on geosynchronous altitude
(5.632 earth radii). While we have not expressly selected the
minimum background-feature intensity that merits consideration,
a reasonable figure based on a comparison to weakly-radiating
man made sources would be 100 watts emitted isotropically into
4π steradians from 1 km^2 of projected area, which is about
10 w/km^2 ster.

1.3. Overview of Infrared Aurora and Airglow

For further orientation, Table 2 presents a brief out-
line of the characteristics of aurora and airglow that influence
the infrared clutter background, and Figure 2 shows the emission
spectrum measured from a sounding rocket just below the radiating
volumes at a time of intense aurora (Ref 7). The technical issues
in Table 2 will be reviewed quantitatively in Sections 2 and 3.

Spatial and temporal inhomogeneity of auroral infra-
red radiance is principally due to the high variability of the
flux of incoming energetic electrons. The spatial gradients
are generally smoothed (and occasionally enhanced) by upper
atmospheric winds and turbulence. The emitting air volumes tend
to align along the direction of the earth's magnetic field (as
indicated in Fig 1), since these electrons are constrained
within a few meters of a field line (the Larmor radius) between
their occasional large-angle elastic scatterings by atomic
nuclei. Airglow, on the other hand, results from slow chemi-
luminous reactions following long-period solar ultraviolet
irradiation, and hence the time and space scales of its intensity
changes are considerably longer than those of aurora; the short-
period variability of airglow is due principally to atmosphere-
dynamics. Infrared aurora is limited to the range of high
latitudes from which the particle-guiding geomagnetic field
lines extend into the turbulent (due to interaction of the
solar wind; refer to, for example, Ref 8), charged particle-
releasing magnetosphere; airglow, in contrast, is a global
phenomenon because the effects of sunlight illumination of the
upper atmosphere extend to all latitudes/longitudes. The
vertical-column radiance of aurora varies over an enormous
range; the dynamic range of radiance variability of the major
airglow is only about one order of magnitude at a given viewing
projection.

16

Table 2. Technical Background on Infrared Aurora and Airglow

	Aurora	Airglow
Energy Source	Energetic charged particles from the magnetosphere --sporadic input	Ultraviolet photons from the sun --continuous input in daytime
Time Delay between Input and Radiation Output	<<1 sec to ~50 sec, plus a feature persisting >2000 sec	Hours
Geographic Location	Largely confined to latitudes ~10° to 30° from geomagnetic poles	Global -- more variable at high latitudes
Principal Altitude Range of IR Emission	90 to 130 km	80 to 90 km (see also Appendix I and II)
Source of Spatial-Temporal Irregularities	Variability of particle flux due to turbulent interaction of the solar wind with the magnetosphere	Recurring and latitude-dependent due to changes in the sunlight irrad-iance; episodic due to atmosphere dynamics effects caused by geo-magnetic storms, stratospheric warmings, internal atmospheric waves
Range of Radiance Variability (Approximate)	About a factor 10^5 at latitudes where particles enter the atmosphere	± A factor 3

17
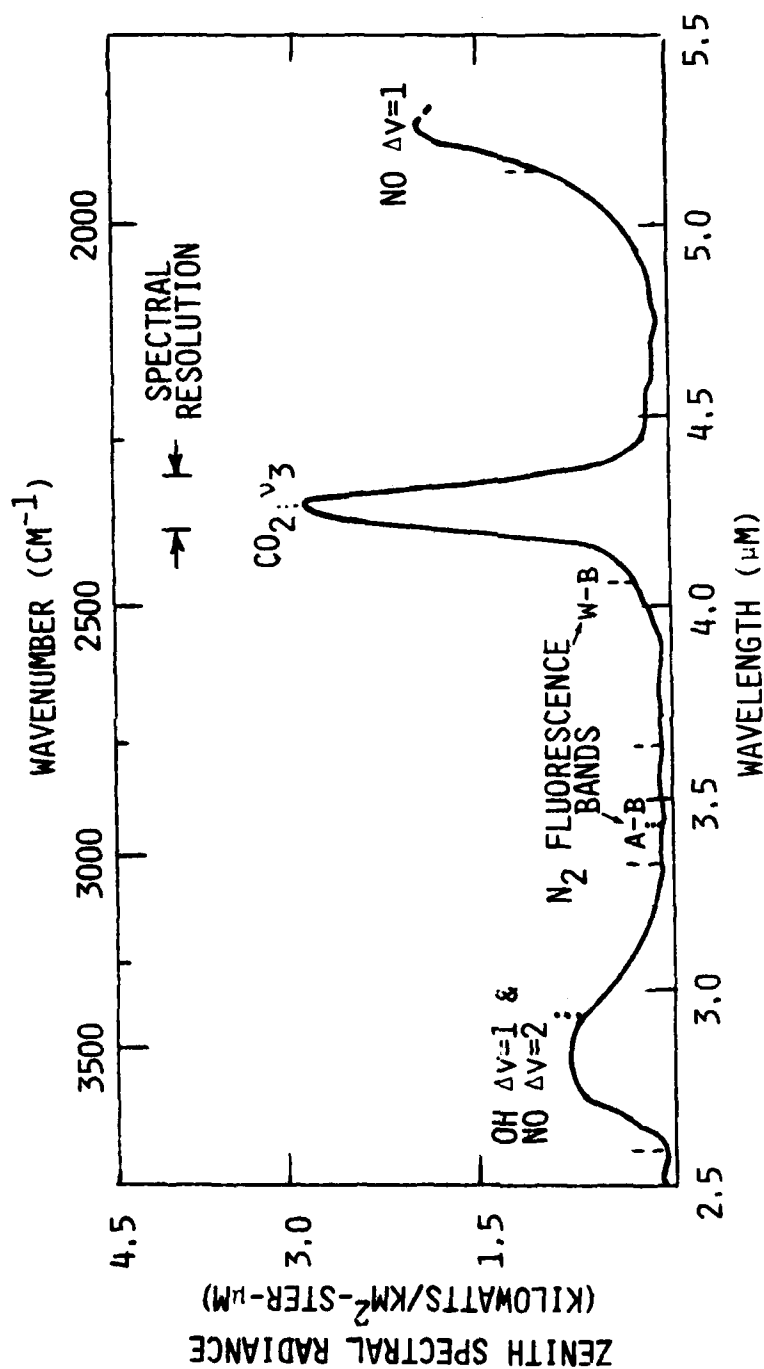
Figure 2. Zenith infrared spectrum of intense aurora (particle energy input ~150 kW/km²) measured from a sounding rocket at 86 km altitude (Ref 7), and positions of N₂ fluorescence bands measured from energetic electron-ejection rocket EXCEDE: Spectral (Ref 6). The spectrum is dominated by vibrational-band chemiluminescence of NO and OH (not spectrally resolved) and emission from CO₂ excited by vibrational and radiation transfer.

1.3.1. Emission Spectrum

A low-resolution infrared spectrum of bright aurora (Fig 2) shows four principal molecular band systems, the vibrational fundamental (labeled $\Delta v = 1$) and first overtone ($\Delta v = 2$) sequences of the nitric oxide molecule, the vibrational fundamental of the hydroxyl radical, and the (001-000) or v_3 transition of carbon dioxide. This strong CO_2 feature lies principally between 4.22 and $4.30\mu m$ at 200 K rotational temperature; we shall refer to it as the $4.3\mu m$ band. It is in part due to scattering of earthshine and thermal emission, in part to the vibrational energy transfer mentioned in Section 1.2, and in part to auroral energy input; this last (complex) process is treated in Section 2.6.2. Fluorescence in several bands of molecular nitrogen also occurs, and although not resolved in this particular spectrum (being much weaker than chemiluminescence) was prominent when electrons of energy about equal to those that produce natural aurora were injected into the lower thermosphere and mesosphere (Ref 6). Fig 2 indicates the wavelengths of some of these fluorescence bands, which are emitted within <<1 sec after the molecules are excited and thus closely reflect the inhomogeneities of the initial particle-energy input pattern.

The fundamental ($\Delta v = 1$) vibrational bands of the ground electronic state of OH, which lie at wavelengths above $2.65\mu m$, overlay the NO overtone radiation. These turn out to be by far the most intense airglow (at any wavelength), and indeed the only one so far detected in the $2-7\mu m$ region (with the exception of the $OH^{\dagger} \rightarrow N_2^{\dagger} \rightarrow CO_2^{\dagger} \rightarrow CO_2 + 4.3\mu m$-photon process noted above). (The symbols $\dagger$ and $*$ indicate vibrationally and electronically excited states respectively.) An infrared airglow from NO, which is largely unstructured and close in peak limb

19

intensity to our nominal threshold of 10 w/km^2 ster, is dis-
cussed in Appendix I. Some other weak (and uncertain) chemilum-
inescent glows from O_3 and NO_2 are reviewed in Appendix II.
OH airglow is excited principally between 80 and 90 km altitude,
at least at night when the emission profile of its shorter-
wavelength vibrational bands (in the $\Delta v = 2$ and higher over-
tone transitions) can be measured from sounding rockets

Auroral emission arises from higher in the atmo-
sphere. The altitude profile of energy deposition depends on
the energy distribution of the incoming charged particles, and
furthermore the efficiency with which these particles' kinetic
energy is converted to radiation in general varies with altitude.
Therefore the infrared aurora's radiance, in vertical as well
as limb projections, depends not only on the total incoming
flux of energy but also on the energies of the individual
charged particles.

1.4. Comparison of Typical Aurora-Airglow and Thermal Radiance Backgrounds

To assess further the potential impact of sky back-
grounds from airglow and aurora relative to the atmosphere's
thermal emissions, we compare some model nadir and limb spec-
tral intensities. Potential AF measurements systems are in
fact stressed by variability in the scene rather than averaged
radiances such as are presented here. To the extent that the
spatial and temporal fluctuations of the non-equilibrium
emissions exceed those of the thermal -- as might be expected
from a sporadic phenomenon such as aurora -- a simple comparison
of mean background intensities underestimates these emissions'
relative effect.

The thermal background from the troposphere and strato-
sphere varies with meteorological conditions, in particular with
the altitude profiles of temperature and water vapor concentra-

tion. For example the six different model atmospheres considered in Ref 2 (LOWTRAN 5 calculations) result in nighttime spectral radiances spanning almost an order of magnitude. In the daytime the wide range of input conditions -- solar zenith angle, earth albedo, and clouds and aerosol, among others -- results in further variability at the short wavelength end of our infrared range. Additionally, the spectral distributions within the aurora-airglow features are subject to some error. In view of the uncertainties in both specifying mean radiances and characterizing the variability, our comparison of typical backgrounds should be considered as only a qualitative measure of the relative contri-tribution to atmospheric clutter made by the non-equilibrium radiations.

1.4.1. Nadir Radiances

Calculated nadir intensities of the hydroxyl-fundamental airglow and a moderately intense aurora are compared with those of the lower atmosphere-earth's surface in Figure 3. As will be done henceforth, the backgrounds are plotted in units of watts per steradian per wavenumber from each km^2 of radiating atmosphere; a wavelength scale is also shown, and units of w/km^2 ster μm are indicated at key points in the plot. Spectral resolution is 20 cm^{-1} for the thermal radiations and about 15 cm^{-1} for the nonequilibrium emissions.

The auroral particle input in Fig 3 is that which results in an output of 35 x 10^9 photons/sec cm^2-column (35 kilorayleighs (kR)) in an air fluorescence feature whose intensity closely follows the energy input rate, the N_2^+ First Negative (0,0) band with head at 0.3914μm. This rate of particle energy input, which is 35 kilowatts/km^2, occurs a few percent of the time at auroral latitudes; roughly 10% of this power is converted to optical radiations. (The input in Fig 2 was about 150 kw/km^2.) The radiances in the nitric oxide bands can be
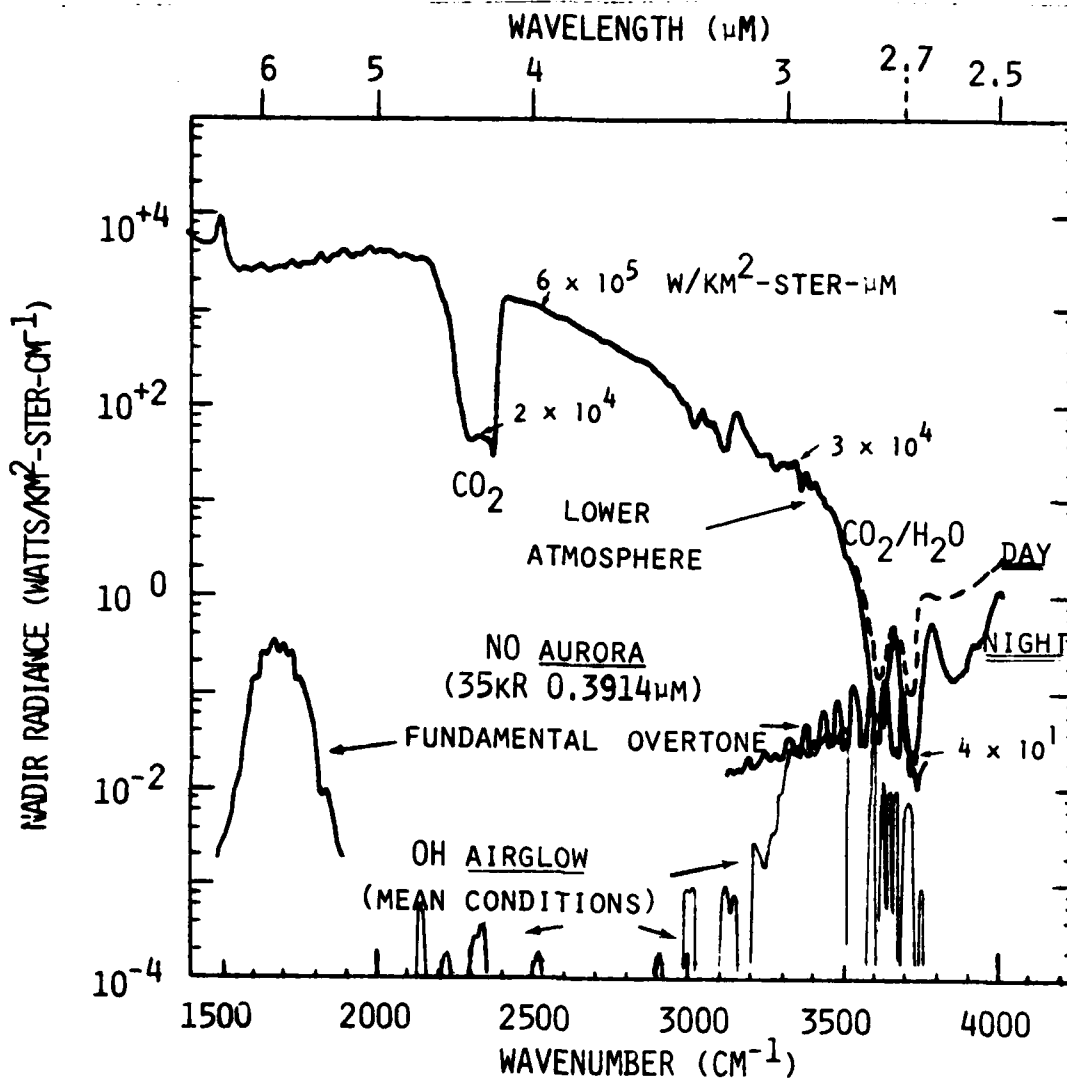
Figure 3. Infrared spectral radiances in the nadir of the mean hydroxyl vibrational-bands airglow, the nitric oxide emissions in 35 kR 0.3914μm aurora, and the thermal emission and sunlight backscatter-int of the lower atmosphere (midlatitude summer conditions, 60° solar zenith angle in the daytime (dashed) curve). Spectral resolution of the thermal background is 20 cm^{-1} (LOWTRAN), of the airglow-aurora ~10 cm^{-1}. Note: These are nominal, model values intended to provide a semiquantitative comparison of atmospheric back-ground intensities; refer to the text.

taken as proportional to the instantaneous rate of energy in-
put when the input is >~5 kw/km^2, so that the NO chemilumin-
escence spectrums in Fig 3 can be moved up or down for other
such high auroral input rates.

As shown, vertical-column brightness in the NO
overtone sequence is about 20 watts/km^2 ster (as described in
Section 2.6.1), and that in the OH fundamental is 13 watts/km^2-
ster (Section 3). The thermal radiance distribution was adapted
from the LOWTRAN calculations in Ref's 2 and 4 for summer (warm)
atmospheres, with its daytime segment taken from SPOT radiation-
transfer code calculations (Ref 9) for the sun at a zenith angle
of 60°.

The comparability of this (intense) aurora and
(normal mean) airglow to the thermal emission at wavenumbers be-
tween ~3400 and 3800 cm^{-1} (wavelengths near 2.7μm) is one of the
most striking features of Fig 3. Qualitatively stated, the strong
absorption-emission bands of the atmosphere's H_2O and CO_2 molecules
in this region of the spectrum make the upwardescaping thermal
radiation intensity characteristic of the kinetic temperatures
near 25 km altitude, which are lower than those at the ground
surface. (This important effect is indicated in Fig 1.) Absorp-
tion of incident and backscattered solar photons by these mole-
cules also reduces the daytime radiance of the nadir hemisphere.

At longer wavelengths (lower wavenumbers), the
thermal background is increased by the combination of a larger
Planck blackbody-radiation envelope and the generally-higher
radiating temperature at lower altitudes. An exception is the
4.3μm CO_2 band, whose effective escape altitude is near the
atmosphere's temperature minimum at 90 km (also indicated in
Fig 1); hence the low sky brightness in this band. Between about
2400 and 2800 cm^{-1} -- 3.4 to 4.2μm -- most of the radiation
reaching nadir-pointing sensors has emerged directly from the
ground or cloud deck; here the "warm" earth and essentially-
transparent atmosphere enhance the thermal radiation relative
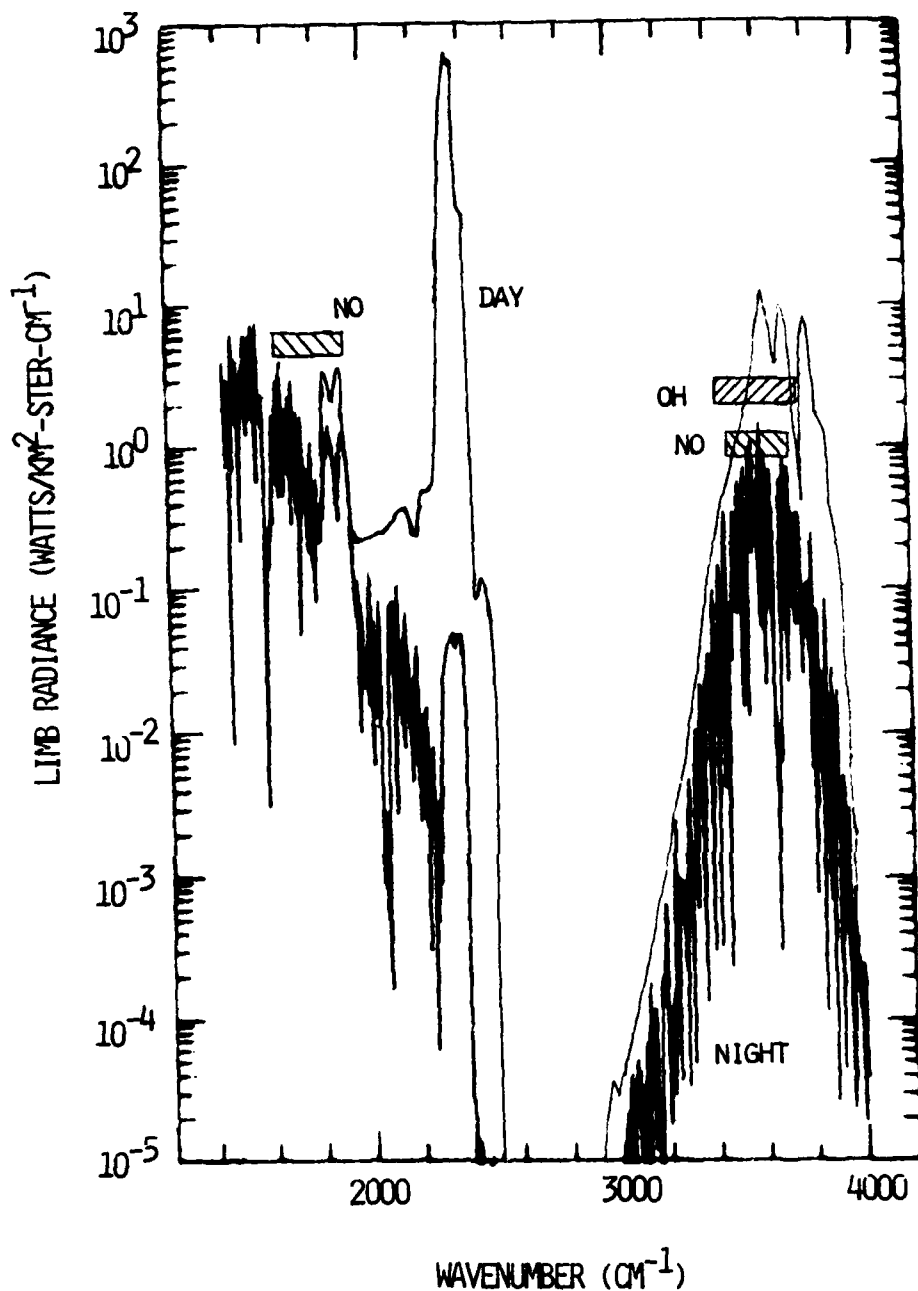
Figure 4. Infrared spectral radiance of the atmosphere's thermal emission at 80 km tangent intercept altitude (from Ref 1) and band-averaged radiances of nitric oxide aurora (35 kR 0.3914μm) and mean hydroxyl airglow. The OH limb radiance, whose spectrum is shown in Fig's 3 and 24, is a maximum at this intercept altitude. A van Rhijn gain factor of 10 has been applied in plotting the NO-band intensities.

ra and airglow. In addition the greatly increased
dy-radiation function (it approaches a maximum near 10μm)
in much more thermal emission near 5.4μm than the NO-
ntal aurora.

1.4.2. Limb Radiance Considerations

In sensor projections that do not intercept
s within a few km of) the earth's surface, those molecular
ons that are absorbed and re-emitted by the atmosphere
the brightest features; that is, the emission spectrum is
d from the nadir view. Additionally, the increased sight
ngths tend to enhance the relative intensity of infrared
and airglow, to which (with the exception of the CO_2
ice band) the overlying atmosphere is optically thin, as
id-integrated surface brightnesses in optically-thick thermal
on features change only slowly with intercept altitude.

We select for an initial comparison of above-
rizon radiances an 80 km tangent intercept (the altitude
sest approach to the earth's surface of a spectrometer's
i-narrow field of view). At this tangent altitude the
path through the mean hydroxyl airglow layer is a maximum;
ie-of-sight of course also passes twice through auroral-
on altitudes. Figure 4 compares model daytime and night-
iermal limb radiances (taken from Ref 1) with nominal,
nber-averaged radiances in the OH and NO bands (the latter
iccompanying 35 kR of 0.3914μm radiation). Note the in-
/ reversal in the CO_2 4.3μm band and the H_2O - CO_2 bands
.7μm, which are identified in Figure 5.

The thermal background in the ~1600-1900 cm^{-1}
-- that is, near 5.4μm -- is three or more orders of
ude below that in nadir projections, and therefore it is
ier large compared to the NO fundamental-band chemilumin-
e. Although the reduction in mean radiance is much less

LIMB RADIANCE (WATTS/KM²-STER (BAND))

10^4
10^3
10^2
10^1
10^0
10^{-1}
10^{-2}
10^{-3}
10^{-4}

H_2O 2.66+2.67 μm
(3770 CM^{-1})
DAY

NIGHT

CO_2 2.69+2.77 μm
(3725 & 3610 CM^{-1},
about equal
intensities)

DAY

DAY
H_2O 2.73 μm
NIGHT (3660 CM^{-1})

H_2O 2.66+2.67 μm
NIGHT

50
100
150

OH AIRGLOW
AURORA

TANGENT INTERCEPT ALTITUDE (KM)
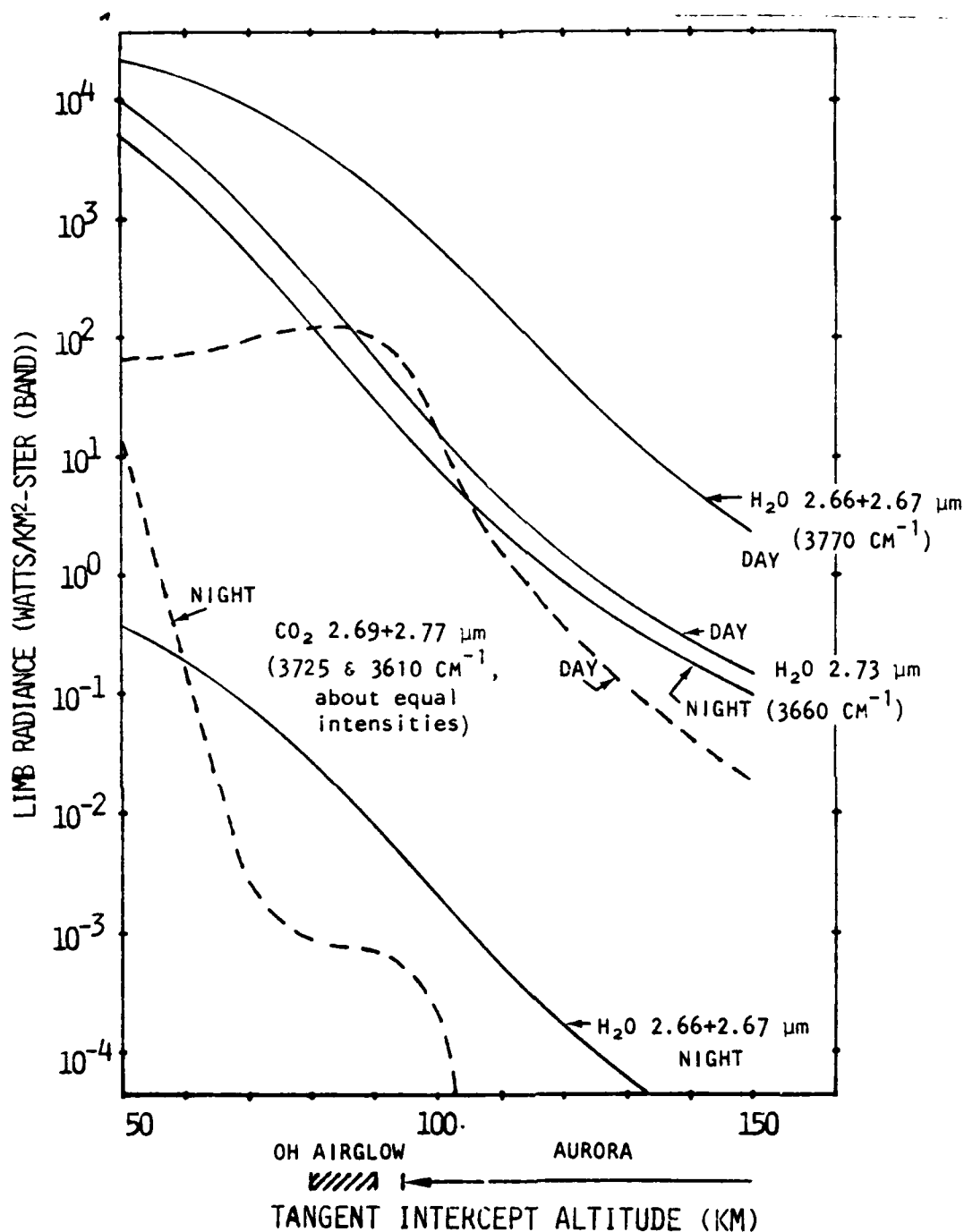
Figure 5. Altitude profiles of radiance due to thermal emission and sunlight-scattering the the H_2O and CO_2 bands near 2.7μm (adapted from Ref 1).[2] The plots show these backgrounds to be about two orders of magnitude weaker at auroral altitudes than at the nighttime hydroxyl airglow altitude.

26

in the 3400 - 3800 cm^{-1} H_2O - CO_2 emission region (at least
for the atmospheric species concentration profiles adopted in
Ref 1, which are subject to revision), the aforementioned effect
of sight path strongly increases airglow-aurora's relative con-
tribution to the sky background. The OH radiation is plotted as
more intense than NO because the maximum increase in path length
is higher through the thinner emitting layer (as will be shown
in the next subsection).

The radiance of the hydroxyl layer decreases
slowly with tangent altitude just above its lower boundary at 80
km (as will also be evident from the next subsection), and then of
course goes to zero at its upper boundary. As Fig 5 shows,
collisionally-excited emission and scattering in the H_2O
bands near 2.7 μm also decreases with altitude. (The daytime
CO_2-band radiances increase slightly to ~90 km before
falling off.) By 115 km tangent altitude these thermal back-
grounds are about two orders of magnitude below those values
shown in Fig 4 for an 80 km intercept. As 115 km is near the
maximum of the emission profile of moderately intense aurora,
the auroral 2.7 μm-band background can be substantially greater
than the thermal background.

We point out once again that these comparisons
refer only to mean sky background intensities rather than fluc-
tuation amplitude within bands of spatial and/or temporal frequency,
and that the thermal radiances vary with atmosphere (and ground-
surface) conditions with the limb subject to particularly
high uncertainty. The model data are intended to put the issue
of spectral intensity of the non-equilibrium radiations into the
context of other infrared backgrounds from the earth's atmosphere.

1.4.2.1. Limb Enhancements

As the distribution of clutter back-
grounds is a strong function of the distribution of sight paths
through the emitting layers, we review briefly the dependence of
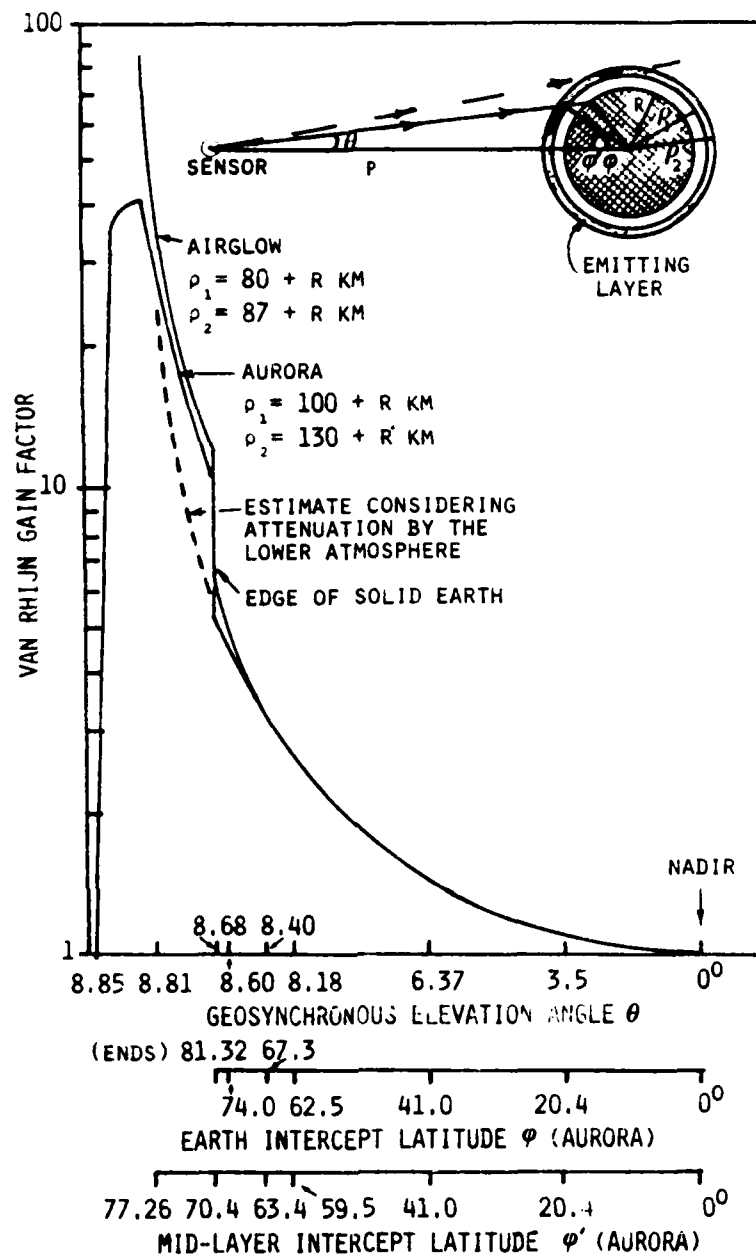
Figure 6. Path length (van Rhijn) gain factors for geo-
synchronous sensors viewing aurora (100-130 km
emission altitude) and hydroxyl airglow (80-87 km).
The projection is illustrated in the diagram at
the top of the graph; the spherical angles λ and
λ' (see text) replace ϕ and ϕ' when the intercept
longitude is not in the sensor's nadir meridian.
The dashed line at tangent intercepts just above
the earth's surface is an estimate that considers
attenuation by the lower atmosphere.

28

radiance of optically-thin (non-scattering, non-absorbing) airglow and aurora on the projection to spaceborne platforms. (A detailed treatment for radiometers having finite field of view below and within airglow layers appears in Ref 10.)

Refer to the diagram in Figure 6, in which height ρ is measured from the earth's center and R = earth radius $\approx$6370 km. The ratio of oblique to vertical volume emission rate-weighted path lengths through a layer is given by the so-called van Rhijn function (Ref's 10,11). For a sensor above a uniform layer of thickness $\rho_2 - \rho_1$ this gain factor is a maximum of $2[(\rho_2 + \rho_1)/(\rho_2 - \rho_1)]^{1/2}$ when the tangent altitude of the sight path is $\rho_1 - R$, that is, when the line of sight just grazes the layer's lower boundary. The maximum van Rhijn gain factor of the nighttime hydroxyl airglow, which has an effective thickness $\rho_2 - \rho_1$ of 7 km, is thus somewhat greater than 80. This multiplier was applied in the estimate of OH limb radiance in Fig 4. Implicit in this calculation is the assumption that the altitude profile of volume emission rate does not vary strongly over the horizontal path, which is 7 x 80 = 560 km. In practice nonuniformity of the hydroxyl emission profile (discussed in Section 3.4) would be expected to result in some reduction of the maximum gain factor.

The effective vertical radiating thickness $\rho_2 - \rho_1$ in intense aurora is about 30 km. The resulting maximum gain factor, 40, would require uniform particle input over 40 x 30 km = 1200 km horizontally, which in fact would be encountered only rarely in nature. Because of aurora's spatially variable volume emission rates, and as an 80 km tangent intercept results in less than the maximum achievable van Rhijn gain, we applied a path length multiplier of only 10 in estimating the NO chemiluminescence intensities in Fig 4.

Referring to Fig 6, the latitude ϕ' of intercept at height ρ of a nadir-meridian sight path from

an equatorial-latitude sensor located at distance P from the
earth's center is related to the path's elevation angle θ by

$$\tan \theta = \rho \sin \phi'/(P - \rho \cos \phi')$$
$$= \sin \phi'/(P/\rho - \cos \phi').$$

Thus

$$\theta = \tan^{-1} [\sin \phi'/(P/\rho - \cos \phi')].$$

Also, from the law of sines,

$$\phi' = \sin^{-1} [(P/\rho) \sin \theta] - \theta.$$

Similarly, the relation between θ and the latitude of intercept
on the earth's surface ϕ (again restricting the sight path to
the meridian in the sensor's nadir) is

$$\theta = \tan^{-1} [\sin \phi/(P/R - \cos \phi)].$$

(When $\rho = R$ the intercept is at the earth's surface.) The path
length from elevation angle θ through a (rectangular, uniform)
layer with upper and lower boundaries ρ_2 and ρ_1 is

$$(\rho_2^2 - P^2 \sin^2\theta)^{1/2} - (\rho_1^2 - P^2 \sin^2\theta)^{1/2} ,$$

when arc $\sin R/P > \theta > 0$;

$$2[(\rho_2^2 - P^2 \sin^2\theta)^{1/2} - (\rho_1^2 - P^2 \sin^2\theta)^{1/2}],$$

when arc $\sin \rho_1/P > \theta >$ arc $\sin R/P$;

$$2(\rho_2^2 - P^2 \sin^2\theta)^{1/2},$$

when arc $\sin \rho_2/P > \theta >$ arc $\sin \rho_1/P$;

and   0,   when $\theta >$ arc $\sin \rho_2/P$.

The van Rhijn factor is just this path-
length divided by the thickness of the layer $\rho_2 - \rho_1$. In practice
the gain does not double discontinuously when the sight path passes
above the solid earth's surface (that is, when sin θ reaches R/P)
because the intervening lower atmosphere attenuates radiation
originating from the back side. When the tangent intercept's
height above the earth's surface is greater than $\rho_1 - R$
(θ greater than sin ρ_1/P; dashed line in Fig 6's diagram)
the path length, but not the gain factor, becomes independent of
this inner boundary height. When P sin $\theta = \rho_1$ the second
term in the second equation above vanishes and the gain factor

reaches its maximum:

$$2[(\rho_2^2 - \rho_1^2)^{1/2}/(\rho_2 - \rho_1)] =$$
$$2[(\rho_2 + \rho_1)/(\rho_2 - \rho_1)]^{1/2}.$$

Limb brightening factors for model spherical shell hydroxyl and intense-auroral profiles, projected to a sensor at equatorial geosynchronous altitude (P = 6.6321R), are shown in Fig 6 as a function of o, ϕ (the intercept latitude on the earth's surface), and ϕ' (taken as the intercept latitude of the auroral emission layer's midpoint). When the line of sight is tangent to the earth's surface $o = 8.68°$, $\phi = 81.32°$, and ϕ' at 115 km midpoint altitude is 70.4°. The abscissa scale in Fig 6 is nonlinear (compressed or (for o) greatly expanded) near the limb, due to the very rapid change in van Rhijn factor with latitude when ϕ' (or ϕ) approaches its upper limit. The above equations show that the sight path factor remains high while the tangent intercept rises through most of the layer, and then rapidly falls off to zero near its upper boundary. Although the maximum gain decreases as the layer width $\rho_2 - \rho_1$ increases, the range of elevation angles o over which it remains near this maximum of course increases with $\rho_2 - \rho_1$.

van Rhijn factors can be readily calculated from the above equations for satellite orbits other than geostationary. The area of earth and infrared airglow-aurora surface accessible to sensor fields of course decreases as the platform's height P - R is decreased. Note that the intercepts cut through aurora-airglow emission altitudes at lower latitudes than those at which they project to ground points; for example, at ground intercepts near the upper-latitude limit of the sight path from geostationary stations the infrared clutter would come from aurora or airglow as much as 11° closer to the equator.

For clarity, the relationships above and Fig 6 were derived for the longitude of intercept points lying on the platform's nadir meridian. The equations and the
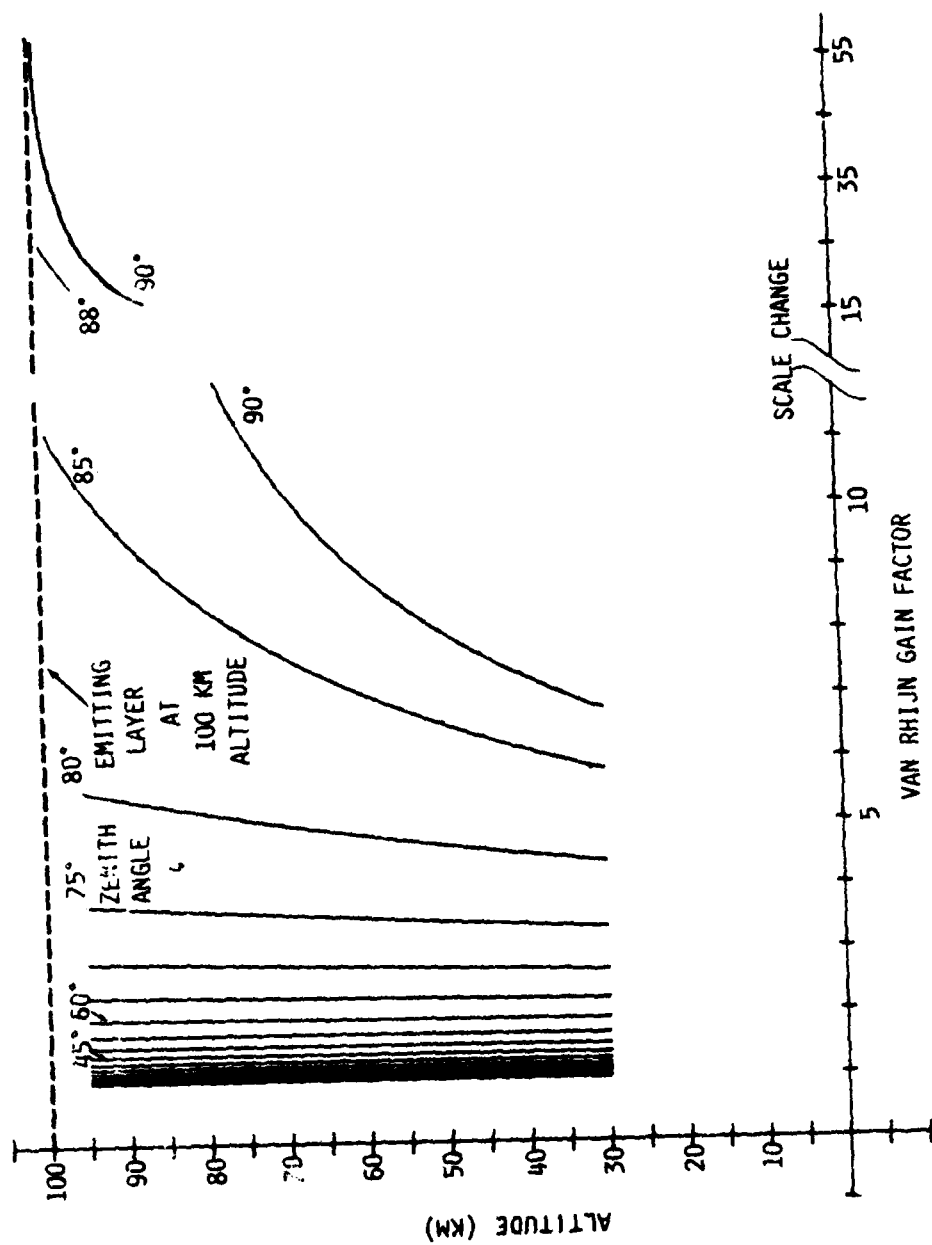
Figure 7. van Rhijn gain factors through a thin emitting layer at 100 km altitude, for narrow-angle sight paths at zenith angles ζ = 0° - 90° from features at altitudes 30 - 99 km. The dependence on ζ and altitude is qualitatively similar for finite layers centered at 115 km (characteristic of aurora) and 84 km (hydroxyl airglow).

two lower abscissa scales in Fig 6 can be generalized to include points on the earth's surface at latitude ϕ (measured from the equator), longitude ψ (measured from the nadir) by replacing ϕ with a new intercept angle λ derived from the simple spherical-triangle relationship $\cos \lambda = \cos \phi \cos \psi$. Similarly, λ' becomes $\cos^{-1}(\cos \phi' \cos \psi')$, where ϕ' and ψ' are the latitude and longitude of the sensor field's intercept on the glow layer. λ or λ' then replaces ϕ or ϕ' in determining the elevation angle θ, which no longer is restricted to the meridian plane illustrated in Fig 6.

Figure 7 (from calculations in Ref 10) further illustrates the impact of oblique projections to the curved earth on the distribution of sky background radiances from airglow or aurora. The plot shows this emitting path length as a function of zenith angle ζ ($=\phi' + \theta$) to the sensor from surveillance targets underneath a narrow radiating layer at 100 km. The dependence of the zenith radiance multiplier on the sensor's zenith angle and the target's altitude is qualitatively similar when layers of finite width are at airglow and auroral altitudes.

1.4.2.2. Effect of Limb Enhancements on Backgrounds Distributions

We have presented the rather detailed atmospheric path-length information in Section 1.4.2.1 because sight paths play a very important part in determining the pro-bability distributions of atmospheric radiance and clutter viewed by spaceborne sensors. The van Rhijn gain factors looking from equatorial geosynchronous altitude are generally high at the high latitudes where aurora occurs. In addition the vertical-column hydroxyl radiance is both uncertain and noisy at high latitudes, because of the perturbations of the mesosphere caused by magneto-spheric substorms and stratospheric warmings.

2. Auroral Infrared Backgrounds

The task of characterizing auroral sky background noise becomes greatly simplified if the phenomenology of particle energy-input occurrence can be treated separately from the aerochemistry that results in infrared emissions. Input to spatially-localized regions would first be specified, and then the efficiencies and (equally important) characteristic times for conversion of energy into individual spectrum features would determine the atmosphere's radiance distribution. Qualitatively speaking, the emission inhomogeneities would be those of this energy input convolved with the time delays and resulting transport associated with excitation of the radiating species.

In practice each infrared output has an essentially linear dependence on energy input; that is, changes in the atmosphere's composition during aurora do not measurably alter the spectral yield or the deposition profile, and furthermore the chemical reactions leading to excitation of individual radiating species proceed independently. In addition the disturbance in the atmosphere does not react back on the disturbance in the magnetosphere responsible for the incoming-particle streams. Hence the two major aspects of the natural-backgrounds question, auroral phenomenology and radiation chemistry of air, can indeed be decoupled and considered separately.

2.1. Data Base on Auroral Occurrence and Aerochemistry

Auroral occurrence phenomenology (Ref 12) has long been a subject of research, principally at institutions located at high latitudes. In contrast, most of the existing information about the chemistry and spectroscopy of auroral infrared results from work done in recent years by Air Force Geophysics Laboratory.

To ensure that no potentially relevant information on auroral (and also airglow) occurrence statistics, spatial/temporal uniformity, and excitation of infrared radiations would be

34

omitted in specifying clutter models, we made computer-assisted
surveys of the technical reports on those topics. Figure 8 is
the logic flow chart of our initial search of scientific journals,
which used the Massachusetts Institute of Technology's Computer-
ized Literature Search Service. The data base was the worldwide
open technical literature (INSPEC) on geophysics, atmosphere
and atmospheric optics, environment, meteorology, and planetary
and space sciences, which includes approximately 150 journals,
22 annual publications, and 60 monographs. The strategy of
Fig 8 resulted in 278 and 112 abstract printouts respectively
for the periods 1969-77 and 1978-81. About 50 further reports
were identified from this source with a somewhat different
logic that used the descriptors auroral morphology, structure,
and inhomogeneity (among others). This latter search strategy
was then applied to the National Technical Information Service
listing of 1964-1981 Government-sponsored (largely DoD and
NASA) research, resulting in identification of 154 reports.

This literature search as expected turned up moderately
useful information on the systematics of auroral energy input
and potentially-applicable unanalyzed data (as discussed in
Section 2.8.3.2), but no comprehensive survey of the distri-
bution of input-particle flux and energy occurrence as a
function of geographic coordinates, time, and magnetosphere
conditions. That is, no previous global model of intensity and
fluctuation structure of aurora, or of airglow, was found.
Additionally, no significant new data on upper-atmospheric
infrared radiation beyond those considered in AFGL's current
planning of field and laboratory measurements were identified.

2.2. Occurrence Phenomenology

The concept of an auroral-occurrence region having a
boundary that varies with a readily-measurable geophysical
parameter provides a starting point for defining physically-

User 45' Date:29apr81 Time 13:40:17 File: 13

Set Items Description
1   715 AURORA?/TI. DE. ID
2   163 AIRGLOW/TI. DE. ID
3   81 NIGHTGLOW/TI. DE. ID
4   1 DAY(W)GLOW/TI. DE. ID
5   17 DAYGLOW/TI. DE. ID
6   0 TWILIGHT(W)GLOW/TI. DE. ID
7   897 1 OR 2 OR 3 OR 4 OR 5 OR 6
8   897 NIGHT(W)GLOW/TI. DE. ID OR S7
9 40096 MEASUR?/TI. DE. ID OR DATA/DF
10 28724 CATA/TI. DE. ID
11   132 9:8
12   49 10:8
13 7216 SPATIAL
14 2629 MOVEMENT
15 4627 MOVING
16 2228 TEMPORAL
17 11226 VARIATION
18   777 VARIANT
19 8392 VARY?
20 7547 FLUCTUAT?
21   574? TURBULEN?
22 45123 13 OR 14 OR 15 OR 16 OR 17 OR 18
23 44346 22-18
24   25 23-11
25   17 23-12
26   39 24OR25
27   230 POWER(W)SPECTRAL(W)DENSIT?
28   1 27+(9OR10)-3
29   39 28OR26
30 5429 CHEMILUMINESCEN? OR VIBRALUMINESCEN? OR FLUORESCEN
31   1 VIBROLUMINESCEN?
32 5430 30OR31
33   513 UPPER(W)ATMOSPHER?
34   201 HIGH(W)ALTITUD?
35 2437 IONOSPHER?
36   12 MESOPHER?
37   80 AERONOM?
38   4 EARTH(W)LIMB?
39 3125 33 OR 34 OR 35 OR 36 OR 37 OR 34
40   21 39-32
41 15556 OBSERV?/TI. DE. ID
42 6029 RECORD?/TI. DE. ID
43 10297 IMAG?/TI. DE. ID
44 4159 PICTUR?/TI. DE. ID
45 5257 PHOTOGRAPH?
46 36194 41OR42OR43OR44OR45
47 35949 FILM?/TI. DE. ID OR VIDEO/TI. DE. ID OR CAMERA
48 64567 46OR47
49   12 NARROW(W)FIELD
50   944 IRREGULAR
51 5735 MODULAT?
52 1404 PULSA?
53 12006 49 OR 50 OR 51 OR 52
54   1 40-(9OR10)+(27OR23)
55 55437 53OR?7OR22

55121577 9OR10OR48

57   912 4OOR8
58   112 57AND56AND55
59 11312 SUNSPOT? OR SUN(W)SPOT? OR SOLA
60   100 58-59

Print 58/5/1-112

Search Time: 0.449   Prints: 112   Descs.: 60

VIEW
MAP
SCAN
TELEVIS
TV
DE. ID OR CAMERA

Figure 8.

Logic chart for the
initial computer
search of the
journal literature
on occurrence and
structure of aurora
and airglow.

36
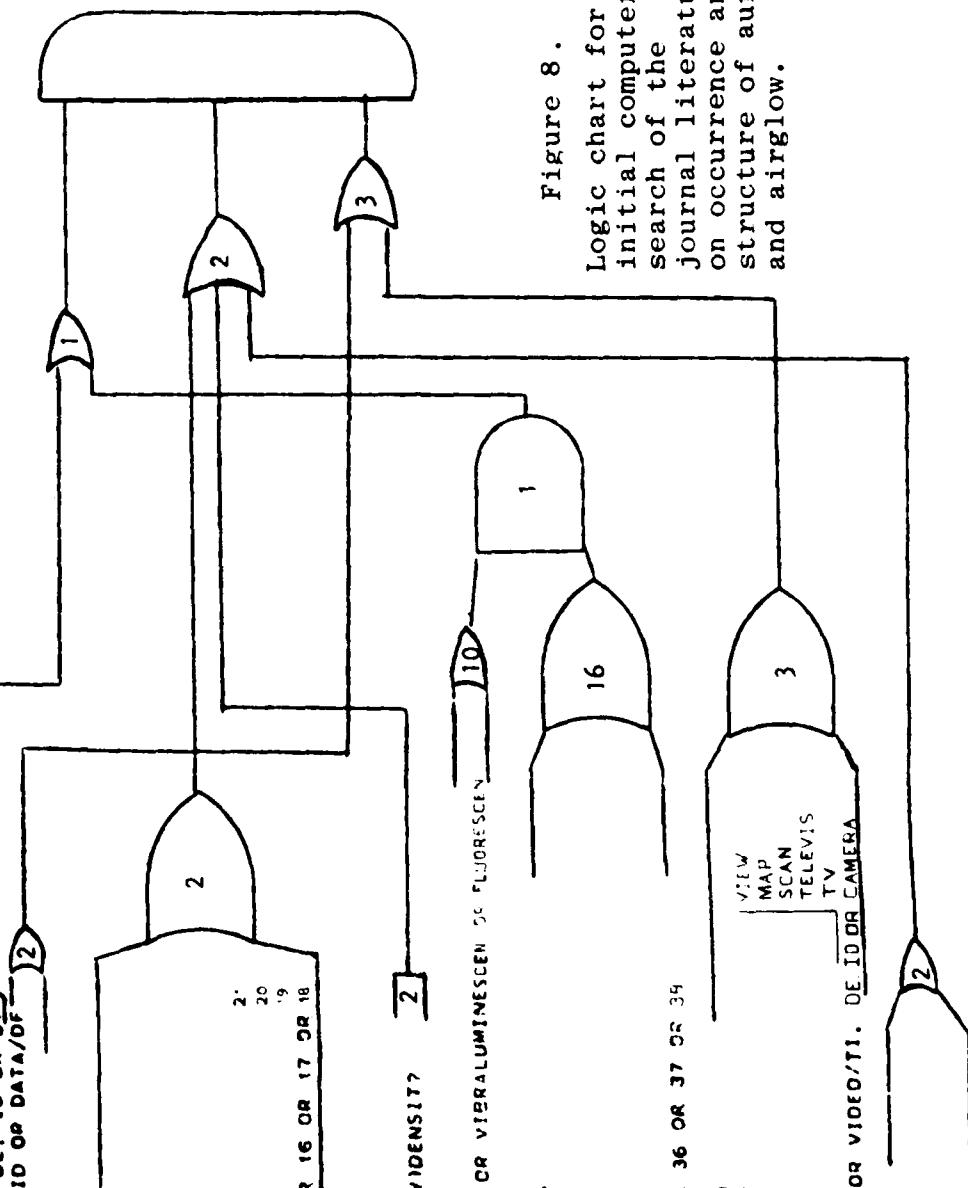
appropriate, frequency distributions of energy input and
spatial-temporal irregularity.

2.2.1. Auroral Oval

One of the first "occurrence" questions to have
been considered was that of probability of visually- or photo-
graphically-detectable aurora appearing in the zenith as a
function of the observer's latitude and longitude. When this
long-standing problem was addressed by analysis of the spatial
and temporal distributions of visible air fluorescence measured
by groundbased wide-angle camera networks, the occurrence data
were found to be ordered by a statistical construct now called
the auroral oval (Ref's 8,13). This oval is, in effect, the
locus of probability >~70% that >~500 w/km^2 energy input rate
(0.3914μm-band brightness >1/2 kilorayleigh) appears over-
head within a 30-min period.

Figure 9 shows the location of this eccentric-
annular occurrence region in the northern hemisphere. Some
particle input also occurs both north and south of this area;
the fluxes in the region poleward of its inner boundary, known
as the polar cap, are generally both low compared to those
within the oval and absorbed at high altitudes where infrared
chemiluminescence is weak and unstructured. The oval rotates
once each day about the earth's geomagnetic pole with its
center displaced roughly 5° away from the sun's direction.
Its latitudinal extent increases with the amplitude of varia-
tions in intensity of the earth's magnetic field, which are
caused by current systems in the ionosphere that are a result
of the same processes that underlie charged-particle flow into
the atmosphere. Hence the area where most auroral energy input
is occuring can be predicted from the magnitude of this dis-
turbance of the field, as is further discussed in Section 2.8.

Visible air-fluorescence and particle-count data
taken from satellites and fluorescence and ionosphere electron
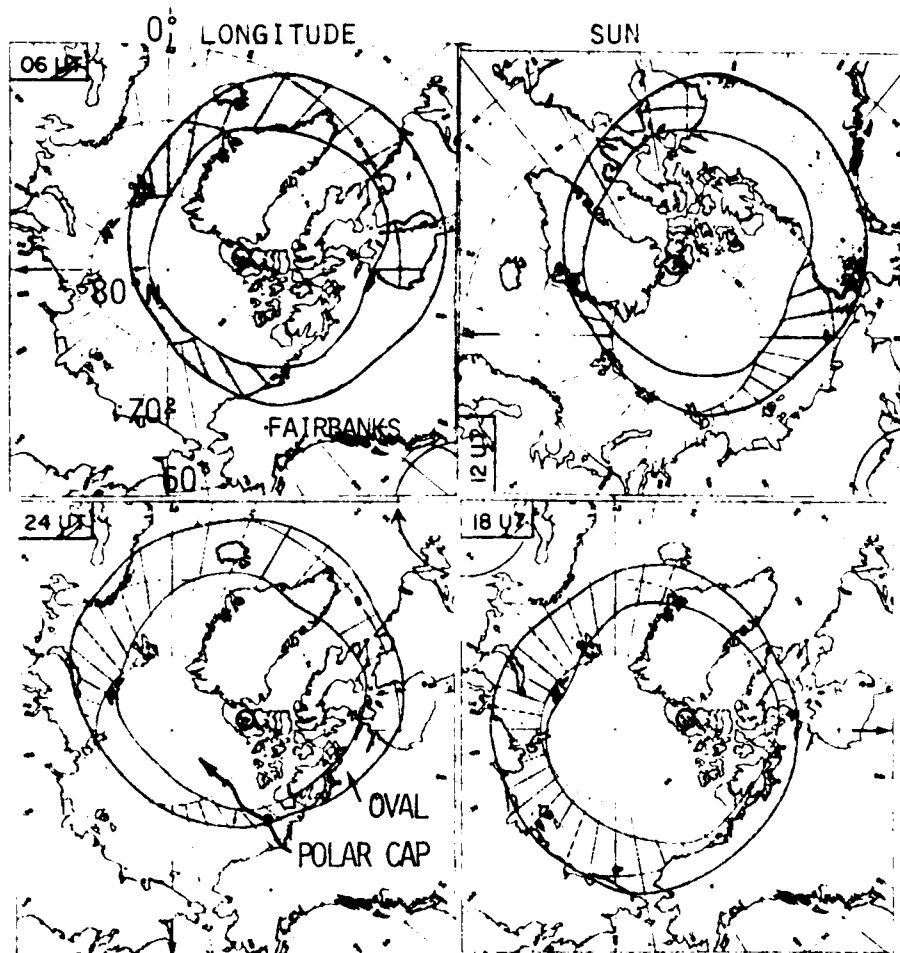
Figure 9.   Location of the "average" northern-
            hemisphere auroral oval (adapted from
            Ref 8).   The eccentric region rotates
            clockwise once per day; refer to section
            2.8.2.   The geomagnetic pole is shown as
            a small circle at the center of each map
            and the direction to the sun is indicated
            with arrows.

38

ity data from aircraft (Ref 14) have shown the auroral
.s to be reasonably well-defined regions of diffuse particle
it in which local higher-flux areas are embedded. USAF's
ir orbiting Defense Meteorological Satellite Program (DMSP)
icles (Ref 15) and the ISIS satellites (Ref 16) have provided
:icularly useful information on the spatial-temporal patterns
input flux and the energy distributions of the incoming
:icles, and imaging photometers on the high eccentricity-
it Dynamics Explorer satellite (Appendix III) are now return-
virtually continuous views of the large-scale pattern of
:gy input into the atmosphere.

2.2.2. Zenith-Flux Occurrence Probabilities

The oval concept localizes occurrence and leads
:he more pertinent question of the probability of magnitude
the zenith flux at each latitude-longitude. These input-
:nsity probabilities can be estimated from the auroral
-fluorescence and particle-spectroscopy data bases, as
l be discussed in Section 2.8; the currently most access-
: data, which we have specified for the flux occurrences,
: from DMSP. The oval's rotation in part defines the diurnal
iation of energy input rate at a given latitude and longitude.

Since the yields of infrared chemiluminescence
i also fluorescence) vary with the excitation altitude,
ral radiances depend on the altitude profiles of energy
osition. That is to say, three-dimensional energy input
bability distributions are needed to determine the sky
kground in both nadir and near-limb sight paths. Fortun-
ly there exists a statistical correlation between total
it flux and altitude distribution that allows the profile
e estimated (Section 2.4.3), which simplifies development
a model of mean volume input rate by eliminating one input
ameter. (Unfortunately, however, as a result of this correla-

tion the amount of energy deposited at each altitude changes
nonlinearly with the total vertically-directed flux -- it can
even go in the opposite direction (Fig 10); thus the fractional
variations in volume excitation rates are not simply proportional
to the corresponding irregularities in energy input rate.)

2.2.3. Line-of-Sight Input Occurrence

As the average van Rhijn factor through the
auroral oval from geosynchronous sensors is comparable to its
maximum value (Section 1.4), the horizontal component of the
sight path is typically of order 10 x the 30-km vertical emission
halfwidth or ~300 km. In most cases this distance exceeds
the distance over which the particle flux is spatially uniform;
that is, the path length is greater than the characteristic
scale or correlation length of the auroral energy input. Thus
multiplying the zenith energy flux at a specified latitude/
longitude by its van Rhijn factor (inside the boundaries of the
oval) would tend to result in too high or too low an input within
the slant-path column. The error due to this broadening of the
distribution of energy input can in principle be corrected by
applying a model of the spatial distribution of zenith flux
along sets of lines of sight.

Intense, discrete aurora -- which is most likely
to degrade exoatmospheric measurements of other phenomena -- is
frequently striated with long axis oriented geomagnetically east-
west, that is, about parallel to the oval's boundaries. This
directionality leads to a qualitatively different pattern of
occurrence of energy input within oblique fields of view inter-
secting the auroral layer at longitudes close to and far from
the sensor's nadir, as the sight path may line up with the
striations -- auroral arcs -- at the higher longitudes and
intersects several arcs near the nadir. The anisotropy of the
energy input flux's spatial correlation thus makes the probability
distribution of slant column input change with sensor azimuth
(or longitude angle ψ) along the auroral oval.

2.2.4. Inhomogeneity Occurrence

Spatial and temporal structure of the input is statistically specified by power spectral densities (PSD's) of the particle fluxes. (As noted, the spatial power spectrum is expected to depend on direction relative to the oval's boundaries.) Such spectrums usually have a continuous frequency distribution, which is characterized by an inner and outer scale, along with excess power at some characteristic frequencies. This limited number of points would serve to describe numerically the input inhomogeneity spectrums. (The magnitude of the auroral flux requires only a single, readily-intercomparable descriptor.) That is, probability distributions of the amplitude and frequency at inner and outer scale and of any discrete Fourier components would quantitatively characterize the statistics of energy input irregularity.

2.2.4.1. Spatial Inhomogeneity

Analysis of auroral imagery data from DMSP (Ref 17) is expected to provide information on the spatial spectrum present in broad (several degrees of latitude or longitude) input-flux segments in the very near future. Similarly off-zenith radiance distributions have also been measured with ground-based photometers, for input to AFGL's "BRIM" procedure for calculating infrared limb brightness structure (Ref 18). These appear to be the only available reduced data directly applicable to modeling the spatial inhomogeneities in auroral particle flux. (Much more such data exist in elevation-scan and photographic photometry records from auroral observatories.)

2.2.4.2. Temporal Inhomogeneity

Temporal fluctuations were also measured for BRIM, but do not extend up to the ~1 Hz frequency

range suggested in Section 1.2. Several observations have been made of large-area quasi-coherent regular pulsations and localized flickering of visible aurora (reviewed in Ref 19). The typical auroral power spectrum, which is measured by photometers having both wide and narrow fields of view, shows a steep decrease with increasing frequency and often a subsidiary peak indicating a 5-10 sec periodicity (Ref 20). This finding suggests that the source of auroral particles has natural frequencies in the range of $1/5-1/10$ sec^{-1}, which has implications in design of measurements sensors.

We have found no information relating temporal power spectrum to the mean energy input rate. Pending availability of better information, we prescribe using a power spectrum of the type reported in Ref's 19 and 20 -- (frequency)$^{\sim -3}$ with a peak centered near $1/7$ sec^{-1} -- to characterize the temporal irregularity of all auroral particle fluxes. (We return to this point in Section 2.8.)

2.2.5. Temporal Correlation of Input Flux

As noted, the spatial distribution of auroral energy input often has a long correlation length, particularly in the east-west direction, as shown by the existence of optical forms having nearly uniform brightness extending tens of degrees in longitude (arcs). Similarly, temporal correlation is evidenced by the persistence of the patterns of particle input that produce these forms.

Lifetimes of discrete, intense aurora present within wide-angle aircraft camera fields (~1000 km diameter circles) have been found to be Poisson-distributed with a most probable duration near 15 min (and a weak secondary occurrence maximum near 120 min) (Ref 21). The average duration of nearly-constant zenith energy input rate would of course be shorter, closer to 2 min. Periods of negligible aurora were

42

found to last for typically 20 min or less, but occasionally also extend to 120 min. The 93 hrs of data from this survey represent an average over the auroral oval and magnetic disturbance conditions from near magnetic midnight (which is when the sun's azimuth is on the night-side of the meridian that passes through the geomagnetic poles and the measurement point). This finding of essentially-random occurrence of moderate auroral activity within areas extending several degrees in latitude and longitude is supported by a recent analysis of DMSP data (Ref 22).

These activity periods may be compared with the ~1-3 hr duration of the magnetospheric substorm (Ref 8), a concept that orders many observations of particle- and space plasma-flux patterns. (At a more fundamental level, it serves in understanding the interaction of the solar wind with the magnetosphere that results in release of the auroral particles.) Models of substorm development (Ref 23, for example) call for systematic changes in the (three-dimensional) spatial distributions of energy input and fluctuation structure in the course of its half-dozen phases. The ~20-min "breakup" phase, during which the particle energy input is highly irregular in space and time as well as on-the-average high across much of the oval, would result in particularly intense and structured sky backgrounds. (The spectrum in Fig 2 was taken from underneath what was interpreted as a breakup.)

Adherence to the largely-heuristic construct of the magnetospheric substorm as the aurorally-active period would require segmenting the auroral occurrence model to conform to its phases. On the other hand the development of individual substorms is so highly variable and unpredictable (as is reviewed in Ref 22, which makes note of the "types" of substorms recently proposed), and the spatial-temporal distributions of

energy input within each phase so poorly quantified, that this
may prove impractical or even undesirable. Furthermore there
exists the contrary evidence (Ref's 21,22) that the lifetimes
of auroral energy input are Poisson-(randomly) distributed --
that is, input does not not follow a predictable course --,
about a mean that is substantially less than the duration of
substorms. In consideration of these uncertainties in duration
and systematics of energy input, and the mechanical difficulties
in implementing segmentation by phase, we recommend that the
first-generation model of auroral infrared background omit
explicit consideration of substorm phenomenology.

2.3. Contribution of Protons

Energetic (~100 keV) protons form part of the incom-
ing charged-particle stream, and contribute a spatially-diffuse
component to the optical aurora. Their deposition altitude
profile does not differ greatly from that of the electrons,
with the peak typically between 115 and 130 km. The presence
of protons was initially recognized from the doppler-shifted
hydrogen atom line emissions in auroral spectra, which are
excited when they pick up an orbital electron from the atmo-
sphere's N_2, O_2, or O to become neutral H atoms. During
the segments of their trajectory that they exist as H^o these
particles are unconstrained by the geomagnetic field, which
results in their being Coulomb-scattered about 50 km (root-
mean-square horizontal displacement) before they reach the end
of their ranges (Ref 11). Thus the distribution of energy
deposition by auroral protons is laterally diffused at a scale
much greater than that of the magnetically-confined auroral
electrons; the spatial spectrum has little power at frequencies
greater than $\sim 10^{-2}$ km^{-1} (other than that due to pre-existing
horizontal structuring of the lower thermosphere's density,
which is small).

The temporal power spectrum of the proton component of

auroral input does not exhibit the ~1/10 sec^{-1} character-
istic peak and is otherwise lacking in high frequency components.
While under a few daytime-auroral conditions protons carry as
much as half of the incoming energy, they contribute <~1/10
of the total column excitation in the strong nighttime auroras
most likely to affect measurements systems performance. Thus
protons make only a very small contribution to the time-vari-
ability of the total atmospheric excitation. For these reasons,
the proton flux can be safely omitted from initial treatments
of infrared background clutter.

2.4. Altitude Profiles

Regularities in the altitude profile of energy depo-
sition by the incoming electrons simplify characterization of
the infrared background. Furthermore the statistical correla-
tion between total input flux and range of excitation altitudes
permits construction of a first-approximation model of the
three-dimensional distribution of initial energy deposition
using only one of the two beam parameters.

2.4.1. Particle Energy Distribution

Kinetic energies and pitch angles (direction of
motion relative to the magnetic field) of the incoming auroral
particles have been measured directly from sounding rockets and
low earth orbiting satellites (see, for example, Ref 24). In
many cases the flux of electrons per unit energy can be approx-
imated by a "Maxwellian" distribution $E^1 exp(-E/\alpha)$, in par-
ticular at energies E >1/3 kilo-electron volts, which represent
most of the total energy input and the penetration down to alti-
tudes where infrared chemiluminescence is favored. With this
particle spectrum the differential flux is a maximum at the
e-folding energy α (which can be interpreted as the "tempera-
ture" of the incoming electron beam), and the average electron

energy is 2α. Normalized to a total energy flux F
($=\int_0^\infty E\,dE\,d\phi/dE$) in watts/km^2, the spectrum becomes

$$d\phi(E)/dE = F \times 3.1 \times 10^{18}\,\alpha^{-3}\,E\,\exp(-E/\alpha),$$

where $d\phi/dE$ is the downward-directed number flux of auroral
electrons per electron volt (eℓ/sec-eV passing through a
horizontal km^2 from the upper hemisphere) and E and α are in
units of eV.

Altitude profiles of energy deposition in model
upper atmospheres by these auroral electrons have been calculated
from their ionization, elastic scattering, and magnetic-confine-
ment properties. (Ref 25 reviews the various computations, all
of which assume that the incoming and secondary electrons are
not further accelerated by collective atmospheric processes
such as electric discharges.) Figure 10 plots these deposition
profiles for Maxwellian energy distributions with α = 600 to
10,000 eV at auroral latitudes, where the earth's magnetic field
lines are nearly vertical. Note that the 115-km peak altitude
and 30-km vertical halfwidth in the example of limb brightness
enhancements in Fig 6 refer to α ≈3000 eV, which is characteristic
of moderately intense aurora.

Altitude profiles such as those in Fig 10 are
typical of auroral excitation even when the incoming electrons'
energy distribution departs from Maxwellian. The deposition
rate decreases at high altitudes because the density of the
atmosphere is decreasing, and toward the bottom side because of
the stopping (and backscattering) of the less-energetic primary
particles.

2.4.2. Optical Diagnostics of the Energy Spectrum

As the auroral beam's characteristic energy α
decreases (increases) the excitation profile moves to higher
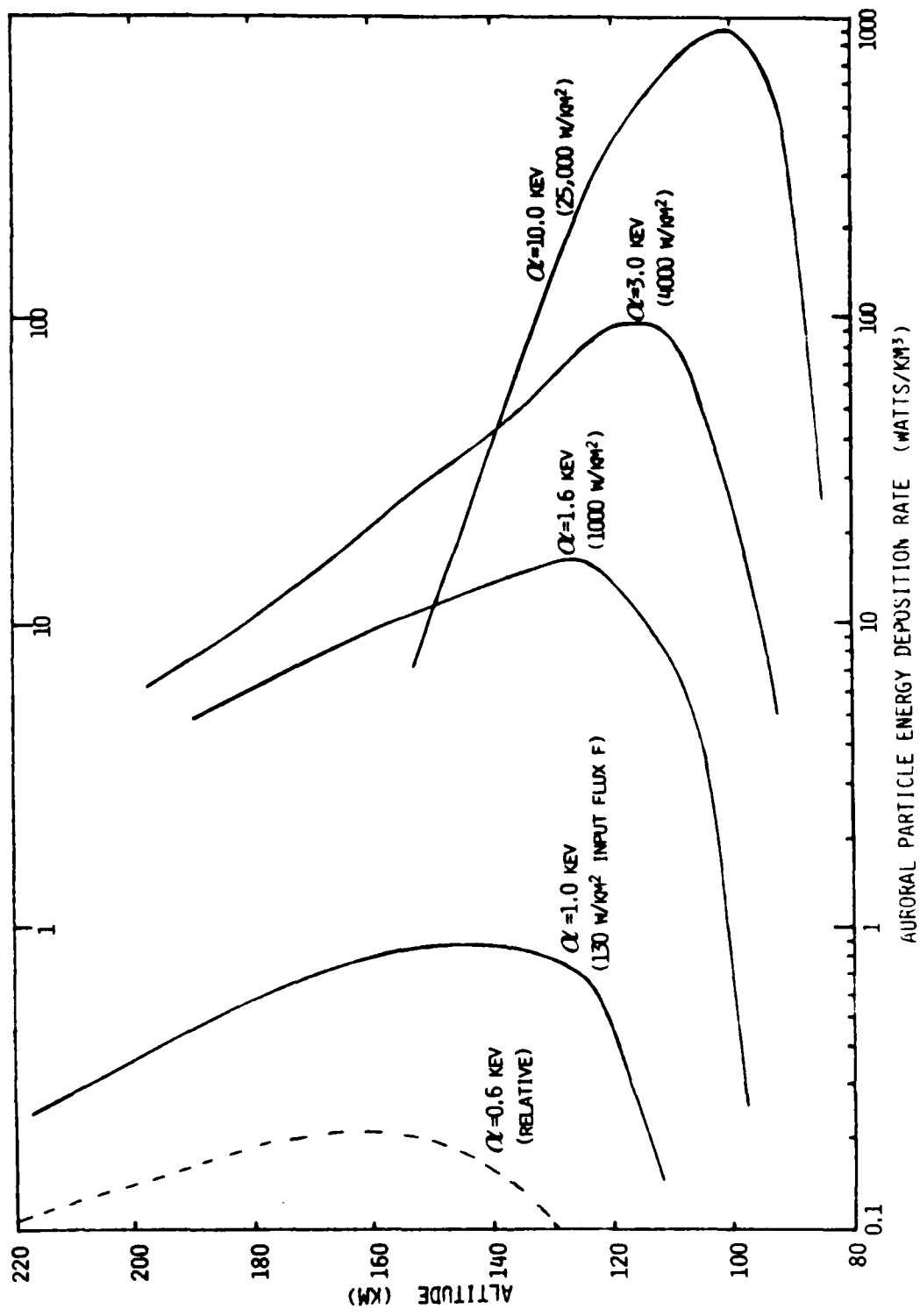
Figure 10. Altitude profiles of energy deposition for five Maxwellian energy parameters. The absolute values on the abscissa assume the total input fluxes in parentheses, which lie on the best-fit line in Fig 11a.

47

(lower) altitudes, where deactivation by collisions is less
(more) probable and the relative concentration of oxygen atoms
is higher (lower). Thus the intensities in emission lines of
O and bands of O_2 and N_2 summed over vertical columns would
be expected to depend on α as well as F. This applies
also to infrared-chemiluminous features, as both the initial
distribution of ionizations, excitations, and dissociations of
ambient species and the subsequent aerochemistry depend on
the relative species concentrations, which vary with altitude.

This principle has been quantified to derive
α for Maxwellian distributions from ratios of near-zenith
radiance of visible auroral features (most notably, in Ref 26)
and nadir radiance in ultraviolet features (Ref's 25,27). (In-
frared emission bands could also be used.) A column intensity
ratio to which α is particularly sensitive and which is readily
experimentally accessible is that of the $0.6300\,\mu m$ line of O to
First Negative bands of N_2^+ (the strong 0.3914 and $0.4278\,\mu m$ bands
provide the best precision). The long-lived metastable upper
state of this red oxygen line is collisionally deactivated below
about 220 km, while the blue-near ultraviolet First Negative
system, which originates from electron impact on N_2 molecules, is
unquenched at all auroral altitudes.

Radiances in these spectroscopic features measured
from ground stations or satellites -- or from aircraft, which
are more accurate because the corrections for scattering of
auroral photons by the atmosphere are very small -- thus permit
estimation of altitude profiles of the energy input. Both the
altitude and halfwidth of the peak in the profile depend on α.
The maximum volume excitation rate also depends on F, to which (as
noted earlier) the column intensities in the N_2^+ bands are closely
proportional. (Actually the ratio $F/(N_2^+\text{-band radiance})$ depends
somewhat on α because the relative concentration of N_2 mole-
cules increases toward lower altitudes, a secondary effect that
is taken into account in Ref 26's model.)

The Maxwellian distribution of course represents
only a two-parameter fit to what is often a structured differ-
ential spectrum with spikes of mono-energetic electrons, par-
ticularly in discrete auroral forms (see, for example, Ref 28).
It underestimates the number of low-energy ($< \sim$300 eV) primaries,
which do not contribute to infrared clutter backgrounds (more
on this shortly) but add to the 0.6300 μm-line radiation.
Furthermore the ratios are recognized as a less-than-perfect
measure of α on both theoretical grounds (the input information
on electron energy dissipation, excitation of molecules and
atoms, and atmosphere composition are subject to some error) and
for experimental reasons (photometers may not view excitation by
electron streams in which α is everywhere constant, especially
if they are not pointed along a magnetic field line; and the 0.63 μm
line emission requires $\sim$1/2 min of near-constant energy
input to reach an equilibrium emission intensity). Nonetheless,
in large part because of its convenience, the spectroscopic-ratios
method has been widely applied for assessing altitude profiles
of auroral excitation. (BRIM's limb-radiance calculations are
based on it, for example.)

2.4.3. Dependence of F on α

In situ measurements of the free-electron density
and energetic-electron flux are inherently the most accurate
means of determining altitude profiles of energy deposition
rates. Unfortunately, too few such measurements have been made
with the aurora remaining stable in space and time during passage
of the rocket probe to systematize the relationship between
F and α. Particle energy spectrums measured from satellites
are another, less direct source of profile information. However
most of the energy distributions reported refer to individual
auroral events being analyzed in depth, and the results of a
major survey (Ref 29) are not presented in a form directly suitable

49

for conversion to sets of deposition profiles. Further, particle-flux data from sun-synchronous polar-orbiting satellites (such as DMSP) apply only to the limited range of local times during which they regularly pass over the auroral ovals.

Still another source is incoherent-backscatter radar data (Ref 30,31), which refer to narrow ranges of latitude/longitude across which the auroral oval cuts obliquely due to its eccentric rotation. These radar results are subject to some uncertainty from the conversion of the measured quantity, ionospheric electron densities, to rates of ionization by the incoming particles (the same can be said about in situ electron density measurements). Although we have identified no published long-period radar survey that focuses on the relationship between F and α (or for that matter on occurrence statistics of F), the input data for a comprehensive study are most probably on record.

An immediately-available data base on energy input profiles appropriate to systematizing auroral infrared backgrounds is the ~6000 spectroscopic ratios measured from a NASA subsonic jet aircraft in 1968-69 (Ref 32). Similar large sets of zenith-photometry data, as yet unanalyzed, are available from the 1967-1980 auroral-latitude flights of AFGL's NKC-135 research aircraft S/N 55-3120 (Ref 33) and 55-3131. (These latter measurements could be segmented by latitude, local time, magnetic-field disturbance, and even phase of the solar cycle -- and perhaps phase of substorms.) We note also that the imaging photometers on the recently-orbited Dynamics Explorer Satellite will provide further systematic information on occurrence and the F-α relationship when F $>\sim$ 1 kw/km^2 over $>\sim(50$ km$)^2$ areas, and that remote optical or ultraviolet sensing from satellites can provide real-time estimates of the auroral energy deposition profile for measurements systems applications, even in the daytime (as is discussed in Appendix III).

The NASA survey consists of approximately 200 hrs of measurements with 3° field photometers (giving a footprint of ~ 5 km on auroral emission), which were averaged over 2-min intervals (~25 km aircraft motion). Since the samplings were made over a period of months at a wide range of auroral latitudes and geomagnetic times (Ref 34) the data base is a more-or-less representative sum over geophysical conditions. (Geomagnetic time (Section 2.8.2) is reckoned from the azimuth angle between the sun and the meridian that passes through the geomagnetic poles and the latitude-longitude to which the time refers.) F and α were measured from the radiances in the 0.4278 μm N_2^+ First Negative band and the 0.6300 μm O line.

Figure 11a shows the polynomial best-fit between F and α (from Ref 32) with the approximate mean range of scatter in their cross plot (from our estimate). (The data set remains available for calculation of the correlation coefficient, which is not given in Ref 32.) The corresponding altitudes of maximum energy deposition (from Ref 35) are plotted in Figure 11b, which includes for later reference the [O]/[N_2] ratio from the Jacchia 1977 model atmosphere (Ref 36).

The considerable natural scatter indicated in the plot of F against α is also evident in auroral-particle spectrums measured by other than optical means (Ref's 23,28, and 37, for example). The spread in peak altitude of the profile (Fig 11b), on the other hand, becomes only ±6 km when F reaches 5000 watts/km^2 (5 kR 0.3914 μm radiation). This narrowing is due to the increasing effect of the exponential increase in atmospheric density near the end of the primary electrons' penetration ranges. Insensitivity to α of the relative profile at high α and F is also evident in Fig 10, which plots absolute rates of energy deposition per unit volume calculated for four α, F on the best-fit regression line in Fig 11a. Parameters of these profiles are given in Table 3.
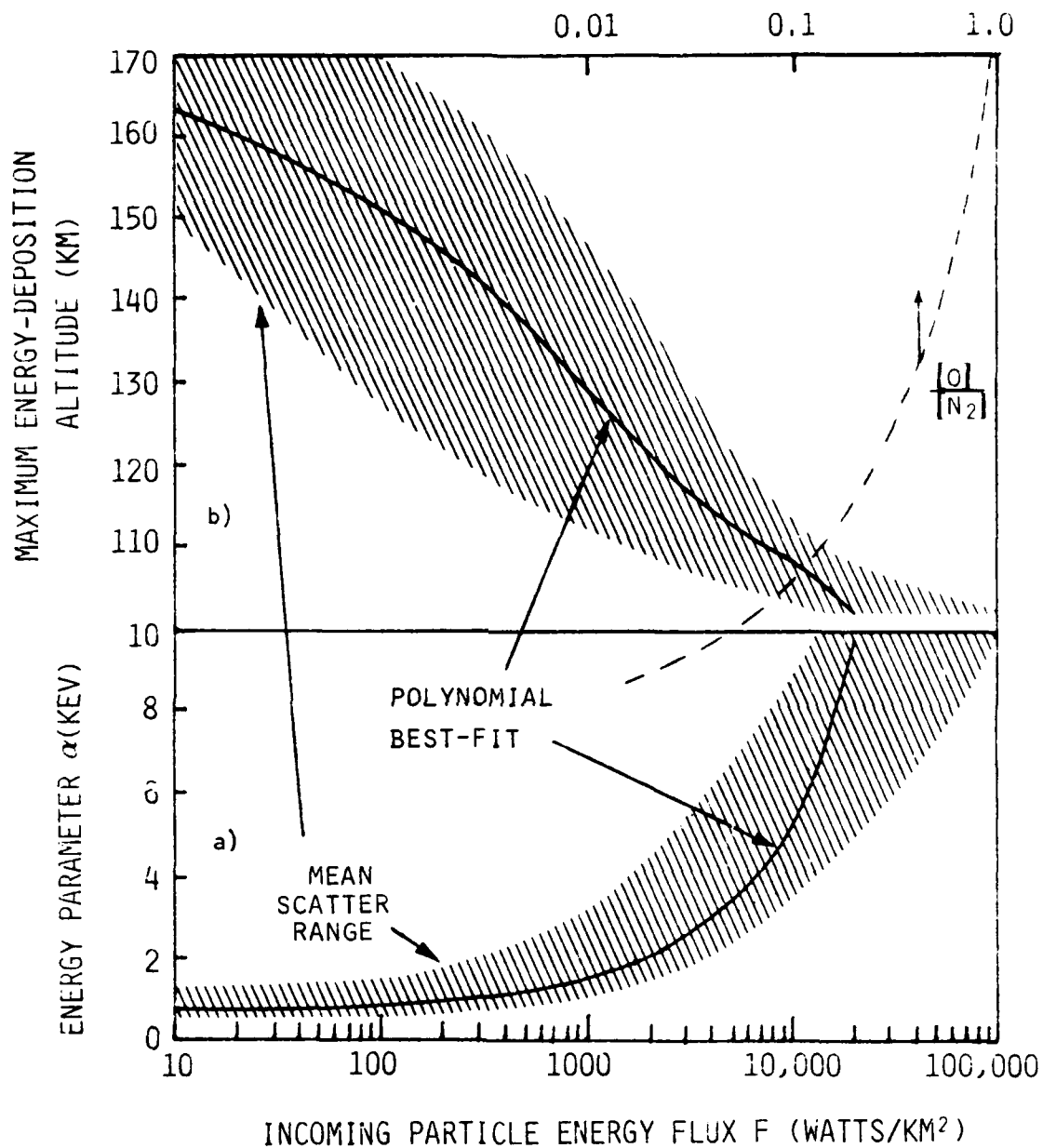
Figure 11. Correlation between Maxwellian energy parameter α
and total incoming-particle flux F as measured
from a survey aircraft by the spectroscopic-ratios
method (a), and resulting correlation between F
and altitude of maximum energy deposition (b).

Table 3. Deposition Altitude Profile Characteristics
(from Fig's 10 & 11)

eV	F, w/km^2	Peak deposition altitude, km	1/2-Peak altitudes, km	Maximum van Rhijn gain
	25,000	102	92-118	45
	4,000	115	105-135	41
	1,000	127	111-166	31
	150	145	120-193	27
	~10-50	170	130-228	23)

2.4.4. Minimum Energy Flux and Energy Parameter

From Fig's 10 and 11 and Table 3 we can assess
nimum auroral energy input rate F_{min} that results in output
rared background radiances greater than the 10 w/km^2-ster
old suggested in Section 1.2. The maximum efficiency with
incoming-particle energy is converted to radiation energy
of the infrared chemiluminescence-vibraluminescence bands
in Fig 2 is about 5%, as we shall show later; and the
m van Rhijn path-length factor in higher-altitude (lower
le-energy) aurora is about 25. Thus

$$10 \text{ w/km}^2 \text{ ster} = (25 \times 0.05 \ F_{min})/4\pi \text{ ster};$$

F_{min} ~100 w/km^2, α_{min} (from Fig 11a) ~ 0.85 keV.
s accompanied by ~1/10 kR of 0.3914µm zenith radiance,
must extend ~2000 km horizontally if the infrared limb
ice is to be as high as 10 w/km^2 ster. For emission
es into which the energy conversion efficiency is 1%, F_{min}
s 500 w/km^2 and α_{min} (again taken from the best-fit
it could of course be higher) about 0.95 keV.

These estimates of the minimum particle energy
rates that might result in degradation of measurements
is data depend only weakly on α, through the deposition
de profile. When α lies below the best fit to the
stical distribution the infrared noise tends to be lower,

53

as chemiluminescence efficiencies generally decrease with altitude and the radiating volumes are more "smeared" by transport of reactants. (The maximum van Rhijn factor also decreases with decreasing α.) This means that when α is small -- less than 1 keV -- even considerably larger input energy fluxes need not be considered in the model of auroral infrared backgrounds.

2.5. Auroral Emissions: Fluorescence

While the minimum input flux rate is a simple function of energy conversion yield and (secondarily) altitude profile (Section 2.4.4), the minimum scale of input irregularities is defined by delays in emission and the resulting transport of precursor species. That is to say, temporal and spatial frequency components of energy input whose effect on the infrared radiance distribution is strongly attenuated by the processes that result in radiation output need not have been initially specified. Hence we turn now to the second major issue in auroral sky backgrounds, how the emissions are excited in the atmosphere.

We consider first the less-complex, and less important, air fluorescence. The auroral particles directly and indirectly excite a number of electronic states of nitrogen molecules, which radiatively (and collisionally) cascade with infrared emission in several band systems. $2\text{-}1/2 - 7\mu m$ fluorescence from the less-abundant O_2 molecules and from O atoms is only of the order of the uncertainty in the spectral yields from N_2, and thus can be neglected. We note for reference that the fluorescence yield from auroral-altitude air in the $0.40 - 0.70\mu m$ visible-wavelength region (which may include some near-prompt chemiluminescence) is close to 2%.

Fluorescence directly reflects the inhomogeneities of initial energy deposition at all spatial and temporal scales, since it is virtually all emitted within <<1 sec of passage of

the auroral particles and transmitted by the overlying atmosphere
The low energy conversion yields, however, result in sky back-
grounds below threshold in all but the most intense aurora.
Synthetic spectra that include the 12 most prominent infrared
band systems of N_2 and N_2^+ have been compiled from detailed
surveys of laboratory excitation-deexcitation data and support-
ing theory, for input to atmospheric and auroral codes (Ref 38).
Figure 12 shows fluorescence efficiency per wavenumber interval
at two altitudes, calculated from this model (in Ref 39) with
the excitation probabilities in one very strong band system (the
$W^3\Delta_u \rightarrow B^3\pi_g$) increased by a factor 20 from its previously-
accepted value to conform to recent EXCEDE artificial auroral
measurements (Ref 6). In practice these W → B bands and those of
of First Positive ($B^3\pi_g \rightarrow A^3\Sigma_u^+$) sequences largely dominate
dominate the fluorescence spectrum of auroral-altitude air
between 2-1/2 and 7μm. (The steepsided broad peaks in Fig 12
are individual emission bands.) The temperatures in these spec-
trums are those of Ref 36's model atmosphere; the spectral distri-
bution of air fluorescence can be seen to have only a very weak
dependence on temperature at the ~5 cm^{-1} resolution.

The energy conversion efficiencies plotted in Fig 12
assume a 70% relative concentration of N_2 at both deposition
altitudes (79% of all particles are N_2 molecules at 90 km, and
60% at 150 km). This simplification introduces much less error
than the uncertainties in excitation cross-sections -- of the
W → B bands in particular -- and cascade branching ratios.
Collisional deactivation has little impact on fluorescence
yields above 120 km, and as the spectra show is only about a
factor-two effect at 92-1/2 km deposition altitude. Since only
a small fraction of auroral particle energy is deposited below
~100 km, little error is introduced into most zenith intensities
if the "unquenched" differential fluorescence efficiencies are
used at all altitudes; alternatively the geometric mean of the
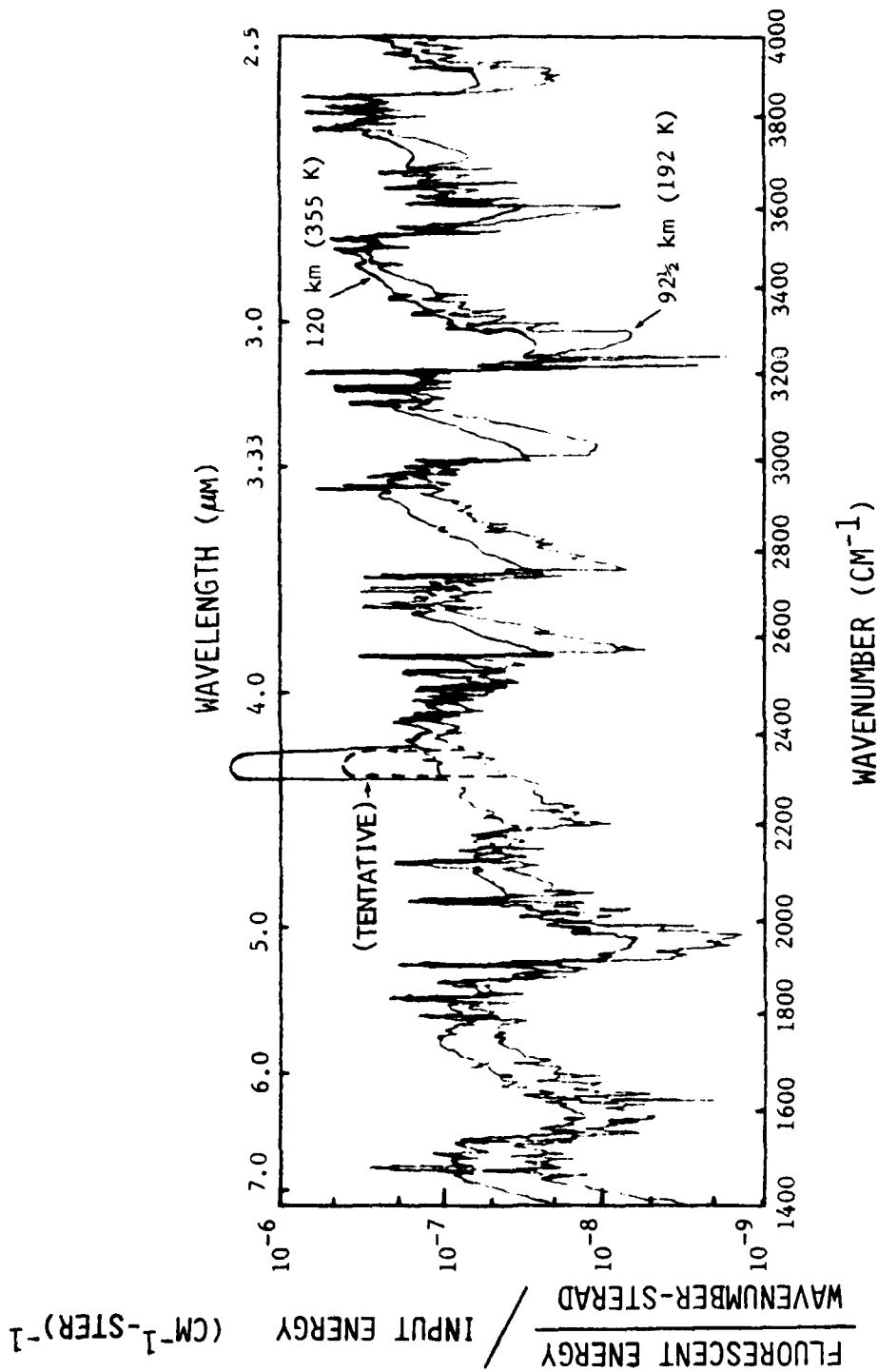
Figure 12. Fluorescence yields of air at 120 km and 92½ km energy deposition altitude. Units are energy output per wavenumber-sterad, per unit energy input. The feature at 4.3μm (shown without spectral detail) has not been fully verified (refer to Fig 18).

efficiencies could be applied. The energy conversion efficiencies given are probably upper limits over much of the spectral range, since the yields in the dominant W $\rightarrow$ B bands are incompletely verified.

The ordinate of Fig 12 is in units

$$\frac{\frac{\text{Fluorescent energy output}}{(\text{km}^2 \text{ column or km}^3 \text{ volume}) (\text{wavenumber-sterad})}}{\frac{\text{Particle energy input}}{(\text{km}^2 \text{ column or km}^3 \text{ volume})}} \ .$$

Sky-background radiance in spectral interval Δk wavenumbers is then F x (sight path factor) x $\int_{\Delta k}$(ordinate in Fig 12)dk. As an example, for the reasonably typical conditions of sight path multiplier = 10 and wavenumber interval 2600-2800 cm^{-1} (3.57-3.85μm filter width; the spiky feature in this interval is the (3,1) W$\rightarrow$B band) the fluorescent radiance reaches the nominal values of Section 1.2 when

$$\text{F x 10 x} \sim (1.5 \times 10^{-7} \text{x 100 cm}^{-1} + 3 \times 10^{-7} \text{x 10 cm}^{-1}) = 10 \text{ w/km}^2,$$
$$\text{F} \approx 55,000 \text{ w/km}^2 \text{ (55 kR 0.3914}\mu\text{m radiation)}.$$

This figure is indicative of the high input flux levels needed to produce significant infrared air fluorescence.

2.5.1. "Prompt" Emission near 4.3μm

A component of the signal measured by 4.3μm filter radiometers pointed toward optical aurora from sounding rockets appears to follow the energy input rates much more closely than the intense CO_2 vibraluminescence-transfer radiation discussed in Section 2.6.2 (Ref's 40,41,42). This "prompt" radiation has not been identified from its spectrum; prime candidates are NO$^+$ chemiluminescence and impact-excitation of CO_2. It is considered sufficiently well validated from the field measurements to be included in AFGL's BRIM model.

We have provisionally included this feature near 4.3μm in Fig 12, taking its energy efficiency from the

57

data interpretations in Ref's 42 and 18 (0.3% total yield at
>110 km, increasing deactivation at lower altitudes), and
its spectral width (but not structure) as that of the CO_2 ν_3
band at 200 K rotational temperature. Its spectral distribution
would be broadened if this radiation is due to NO^+ fundamental
bands; refer to Figure 18 and the discussion in Section 2.6.2.4.

2.6. Auroral Emissions: Chemiluminescence and Vibraluminescence

As is shown in Fig's 2 and 3, the principal auroral
infrared chemiluminescence is in vibrational bands of nitric
oxide at wavelengths above 2.7 and 5.3 μm and carbon dioxide
just below 4.3μm. The upper atmosphere is optically thin
to NO vibrational radiation, which is excited in reactions that
produce new NO molecules; in contrast the CO_2 radiation most
copiously produced by aurora, which is in part absorbed and re-
radiated by the atmosphere, is initially excited by transfer
of vibrational energy from N_2 to pre-existing CO_2 molecules.

The existing data do not rule out the possibility
that still further molecular species created or initially
present in the atmosphere are chemiluminescing. An upper
limit to the energy yield in any such emissions that are spec-
trally separated from the CO_2 and NO bands is ~10^{-4}, as is shown
by spectroradiometry of aurora and artificially-irradiated air
(in both the laboratory and upper atmosphere). With this low
conversion efficiency the maximum limb radiances of these
features would be near the 10 w/km^2-ster threshold in even the
most intense aurora. Furthermore any such chemiluminescence
would be overlaid by at least comparably intense N_2 fluor-
escence, which (as Fig 12 shows) sets a lower limit to the
energy conversion efficiency of about 10^{-4} per 100-wavenumber
interval -- fairly typical of the spectral width of molecular
bands -- over virtually the whole 2-1/2 - 7 μm infrared range.

On the other hand the uncertainty in the absolute yields and spectral distributions of the strong known atmospheric chemiluminescence bands allows for larger yields -- $\sim 10^{-3}$ -- in unidentified emissions that would be masked by these bands. Such radiations would 1) distort the emission spectrum in and within about 50 cm^{-1} ($\sim 1/10\mu m$) of the CO_2 and NO overtone bands (less in the NO fundamental, where higher resolution auroral spectra are available, as described in the next subsection); 2) superpose further temporal frequency components on the sky background noise measured by sensors operating at these wavelengths; and 3) through this change in time scales, alter the spatial distributions of infrared radiance. A detailed review of the minor species in air whose spectrums overlay 2.7, 4.3, and 5.3μm (in the context of irradiation of the atmosphere by nuclear particles, which produce more concentrated excitation than aurora and penetrate to lower altitudes) appears in Ref 43. Since no extraneous emissions other than (perhaps) the "prompt" 4.3μm component can be considered to be verified, we have not explicitly included radiation from these molecules in our model of auroral backgrounds near 2.7 and 5.3μm.

2.6.1. Nitric Oxide

The processes that lead to nitric oxide vibrational radiation in aurora are shown schematically in Figure 13 (adapted from Ref 41; NO aerochemistry has been most recently reviewed in Ref 44). The component responsible for infrared clutter is due to the fast reaction with ambient O_2 molecules of N atoms in the low-lying metastable ^2D state. The resulting vibrationally-excited NO molecules cascade to the ground state by radiating $\Delta v = 1$ or (fewer) $\Delta v = 2$ photons and collisions with O atoms or (with lower probability) O_2 mole-
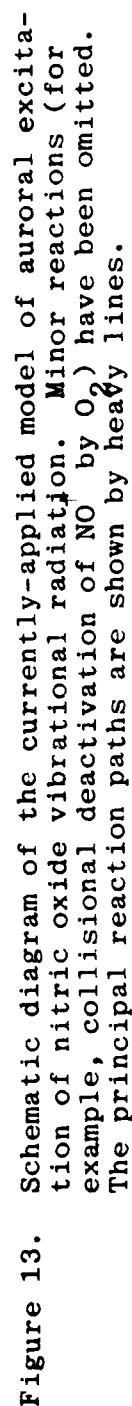
Figure 13. Schematic diagram of the currently-applied model of auroral excitation of nitric oxide vibrational radiation. Minor reactions (for example, collisional deactivation of NO by O_2) have been omitted. The principal reaction paths are shown by heavy lines.

cules. Since they react much more slowly with O_2, ground state N^4S atoms contribute a longer-lived ($\sim$1000 sec), less intense component that adds little to the background's structure.

The spectral distributions in the NO fundamental and overtone sequences, normalized to a particle energy input flux of 35,000 w/km^2 (remaining constant for $> \sim$10 sec), are shown in Figure 14. (The emission spectrums are higher-effective resolution versions of those in Fig 3.) These absolute chemiluminescence efficiencies can be directly compared to the relative N_2 fluorescence efficiencies in Fig 12 by dividing them by 3.5×10^4; the spectral yields from NO can be seen to be one to two orders of magnitude higher. They represent current best-estimates for steady-state auroral excitation, and are believed to be accurate to within $\pm$ a factor 2-1/2 for the fundamental and 1-1/2 for the overtone. Potential errors of this magnitude arise from uncertainties in absolute calibration of the rocket instruments (Ref's 45,46), in some of the rate coefficients for the processes indicated in Fig 13, and also in the altitude profile of atomic oxygen (Ref 44). These "equilibrium-excitation" spectrums were derived from the following experimental and theoretical results.

Yields in the fundamental sequence (Fig 14a) scale a 180 K rotational temperature laboratory spectrum unaffected by quenching (Ref 47) to the chemiluminous yield of 2.0% measured in the auroral limb with the HIRIS interferometric spectrometer (Ref 46). (The yield inferred from lower-resolution zenith spectroradiometry of aurora is 1.5% (Ref 45).) This spectral distribution is very closely fit by the atmospheric spectrum measured in EXCEDE (Ref 6). Unfortunately HIRIS's much higher-resolution spectrums cannot be used directly, as they have a substantial contribution of (1,0) band radiation from thermal excitation of NO. HIRIS and EXCEDE detect no other emission features spectrally overlapping the fundamental bands.
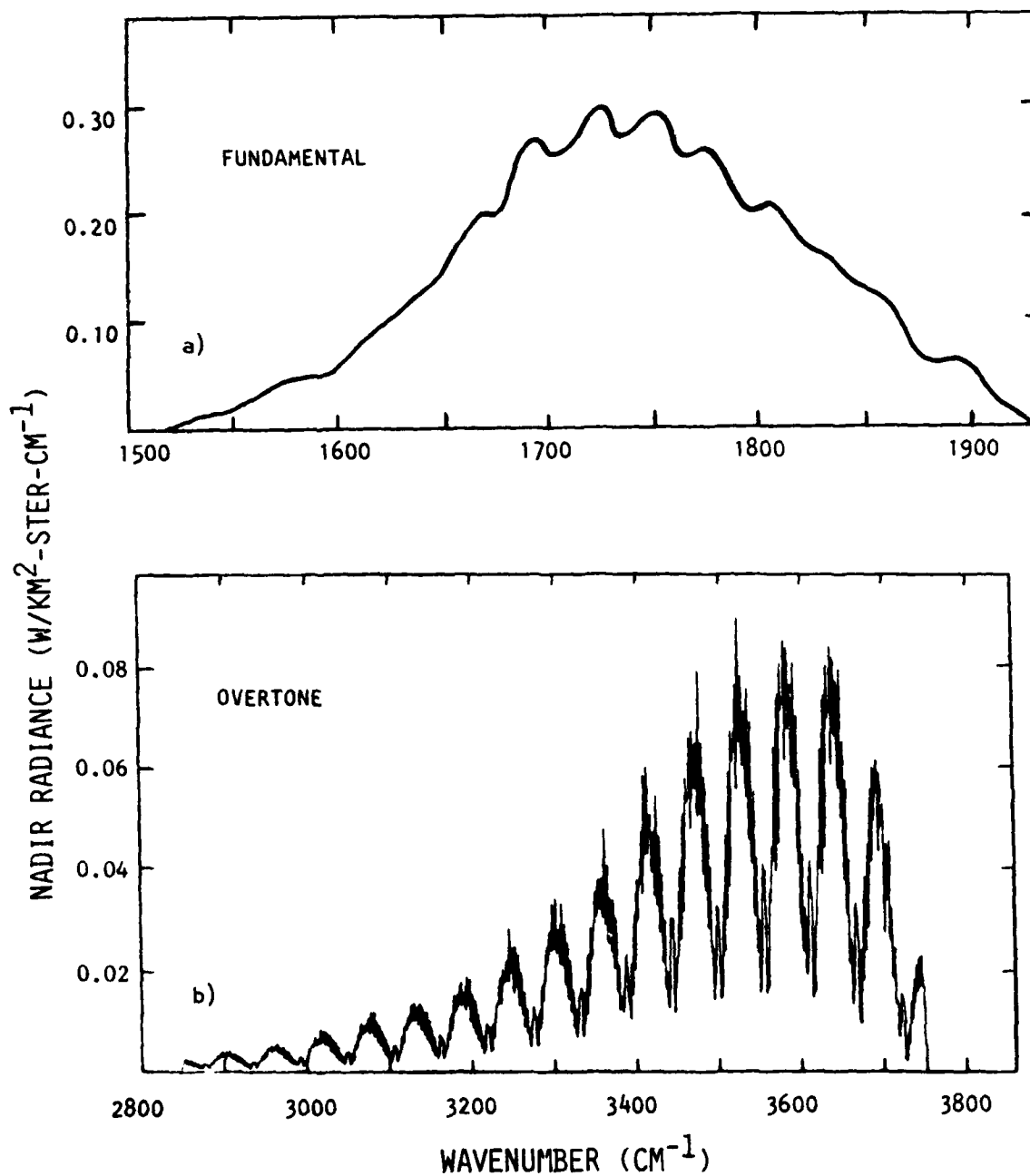
Figure 14. Spectral radiance distributions in the nitric oxide vibrational band sequences with input flux F = 35,000 w/km^2. For direct comparison with Fig 12, divide the ordinate scale by 3.5 x 10^4. Spectral resolution 11 cm^{-1} (fundamental) and 5 cm^{-1} (overtone).

62

The total energy conversion efficiency into the fundamental sequence is about half that predicted from model calculations, perhaps because of quenching or errors in calibration of the instruments. (These calculations input the initial vibrational-state population distribution of NO from the reaction of N^2D with O_2 measured in the laboratory (Ref 47), the calculated transition rates (Einstein coefficients) for the radiative cascade (Ref 48), and the expected number of N^2D precursor atoms produced along with each ionization.) 2% is the best-estimate sequence yield averaged over $\alpha \approx 3$ keV auroral energy deposition profiles.

Although individual NO overtone bands have not been spectrally resolved in the auroral atmosphere, the total yield in the sequence is somewhat better known. We adopt an energy efficiency of 0.7% again averaged over a deposition profile for $\alpha \approx 3$ keV. This figure is the mean of measurements on aurora with with side-viewing (Ref 49) and zenith-pointing (Ref 45) rocket radiometers and zenith-pointing aircraft radiometers (Ref 41); it is also supported by calculations using the above mentioned inputs. The spectral distribution in Fig 14b is calculated from a radiative cascade model by PhotoMetrics' AIRSPEC code (Ref 50). Quenching of N^2D by O atoms, which lowers the total yield at the higher deposition altitudes (Ref 44), is in effect averaged over altitude in Fig 14. Deactivation of $NO^\dagger$ by O, which may halve the volume emission rates near the ~100-km peak of the [O] profile (Ref's 43,44), would affect the relative spectral intensities.

2.6.1.1. Time Dependence

The finite time required for excitation of $NO^\dagger$ results in attenuation of the higher temporal and spatial frequency components of the auroral-sky radiance in these bands. Radiometer data from AFGL's aircraft (Ref 51) indicate that the

63

delay between input of particle energy and output of overtone
radiation, averaged over near-vertical measurement columns,
varies between ~5 sec and <1 sec. Calculations with the
ARCTIC aerochemistry code (Ref 52) show the zenith radiance
asymptotically approaching equilibrium after a step-function
turnon of the particle beam; the e-folding times are 1-1/2 sec
when $\alpha \approx 10$ keV (100 km mean energy deposition altitude)
and 7 sec for 2 keV (120 km), and when the 10 keV beam was
turned off the radiance decreased by a factor e in 1 sec.
BRIM assumes that the final reaction $N^2D + O_2 \to NO^\dagger + O$
is the rate-limiting step in chemiluminescence, that is, the
excitation process is essentially monomolecular; thus the
characteristic exponential time constant is ($[O_2]$ x the
reaction rate coefficient, 5.2×10^{-12} cm^3/sec)$^{-1}$. This
simplification results in substantially shorter grow-in and
decay times at low deposition altitudes than ARCTIC predicts --
1/10 sec at 100 km and 2-1/2 sec at 120 km --, as would be
expected from ignoring reaction paths in Fig 13 that do not
involve direct production of N^2D by electron impact. Clearly,
assuming that $N + O_2$ is the rate-limiting step gives a lower
limit to the time delay, especially at the lower altitudes
where it is not necessarily slower than N^2D's precursor
reactions.

Volume emission rates can be calcul-
ated by applying a procedure developed in Ref 41, which inte-
grates the energy input backward in time with altitude-dependent
exponential time constants (representing consumption of precursor
species produced at a rate proportional to the input rate).
(BRIM uses a closely similar method.) The procedure is valid
when the scale length of the energy deposition pattern is
larger than the physical transport length, so that there
is negligible net flow of reactants into the emitting volume

64

(as discussed in Section 2.6.1.3). The spectral intensity of
nitric oxide radiation at time T is then

(Yield from Figure 14/3.5 x 10^4) x

$(1/\tau)$ $\int^T_{-\infty}$ exp $[-(T - t)/\tau]$ $f(t)dt$ watts/km^3 ster cm^{-1}.
Here $f(t)$ is the rate of energy input at (earlier) time t into
the volume in watts/km^3, which like the characteristic time
τ depends on altitude. Typical values of f in aurora with
total input flux rate F are given in Fig 10. To determine
spectral radiances these volume emission rates are summed along
sensor sight paths. This approach could of course be straight-
forwardly modified to take into account the variation with
altitude of the equilibrium yields of NO-radiation, by placing
the yield underneath the integral sign.

The above equation assumes that the
time dependence of NO chemiluminescence can be characterized by
a single exponential time constant, applicable to both its grow-
in and decay, a simplification not completely consistent with
the aforementioned results of aerochemistry code calculations.
Pending further analysis of AFGL's aircraft radiometry data (now
in progress), which will provide further information about
this time dependence, we prescribe the following provisional
values for τ. In near-vertical sight paths, a lumped-parameter
figure can be adopted for auroral particle beams having energy
parameter α:

α	(F best-fit, from Fig 11)	τ
> 5 keV	> 10^4 w/km^2	1 sec
2 keV	2 x 10^3 w/km^2	5 sec
1 keV	3 x 10^2 w/km^2	50 sec .

For calculations of limb radiance:

Energy deposition altitude	τ
< 100 km	1 sec
110 km	2 sec
120 km	5 sec
135 km	20 sec
150 km	70 sec .

Clearly, the lower-frequency components in the temporal power spectrum of clutter background from $NO^\dagger$ are attenuated as the aurora's energy parameter decreases and deposition altitudes increase. For example, when $\alpha = 2$ keV the amplitude of oscillations in infrared output resulting from energy input pulsating with the "characteristic" auroral period of 10 sec noted in Section 2.2.4.2 is about an order of magnitude less than the input amplitude. Note also the substantial spread in time when $\alpha < 1$ keV (alluded to in Section 2.4.4), which is accompanied by a large spatial spread above the resulting ~140 km peak deposition altitude (Fig 16).

2.6.1.2. Space Dependence

Similarly, transport of the reactive precursor species during these radiation times smears out spatial structure in the NO vibrational-band radiances. Shear in the upper-atmospheric wind distorts the initial energy-input columns, and molecular and eddy diffusion spreads the source of emission vertically as well as horizontally. Although the quantitative effects of this atmospheric transport are specific to the geometry of the input distribution and sight path, and in the general auroral case are not separable from the effects of the temporal dependence of energy input, its overall impact on the radiance distributions can be estimated.

The magnitude and direction of the horizontal wind velocities at auroral latitudes is highly variable, as shown in Figure 15's examples of wind profiles (compiled from the survey in Ref 53 and data from AFGL's recent Auroral-E program, Ref 54). Wind shear turns out to be particularly high near the peaks of the particle energy-input profiles; note the common occurrence near 120 km of 100-200 m/sec differences over 10 km vertical distance. The about-average wind speed of 100 m/sec at 120 km would result in ~1/2 km (100 m/sec x 5-sec τ)

al offset cf the source of NO vibrational radiation from
itially vertical energy-deposition column. Wind vector
les at auroral altitudes and latitudes have been measured
otography of luminous chemical tracers released from
ts (as in Ref's 53 and 54) and recently by more-continuous
erent scatter and other (Ref 55) radar methods. While a
al correlation with magnetic activity is observed, and
rence and atmospheric-circulation models have been advanced
s 56,57), the wind field can be predicted only statistically.

Diffusion coefficients (Ref 58) and
cteristic diffusion lengths of nitrogen atoms at auroral
udes are as follows:

itude	Diffusion Coefficient D		$\sqrt{4D\tau}$
) km	10^2 m^2/sec	-- turbulent eddies	20 meters
) km	10^3 m^2/sec	-- molecular	100 meters
) km	3×10^3 m^2/sec-- molecular		1/4 km
) km	10^4 m^2/sec	-- molecular	1 km
) km	3×10^4 m^2/sec -- molecular		2-1/2 km.

is the rms horizontal transport distance from an initially-
w vertical segment in time τ. The total spread of N atoms
o diffusion would be 2x that shown in the right-hand
n, and diatomic atmospheric molecules (and also ions, such
)$^+$) would be spread $\sqrt{2} \times \sqrt{4D\tau}$. The smearing-out of
rsor concentrations due to diffusion changes very little
geophysical conditions, except at the bottom end of the
of auroral energy input altitudes where the variable tur-
ce dominates atmospheric mixing.

Better estimates of the spatial dis-
tions of infrared radiance that result from given time-
onary (steady-state) input distributions require detailed
sion-wind drift calculations. Further, when the input
is temporally varying -- specifically, if the scale time of
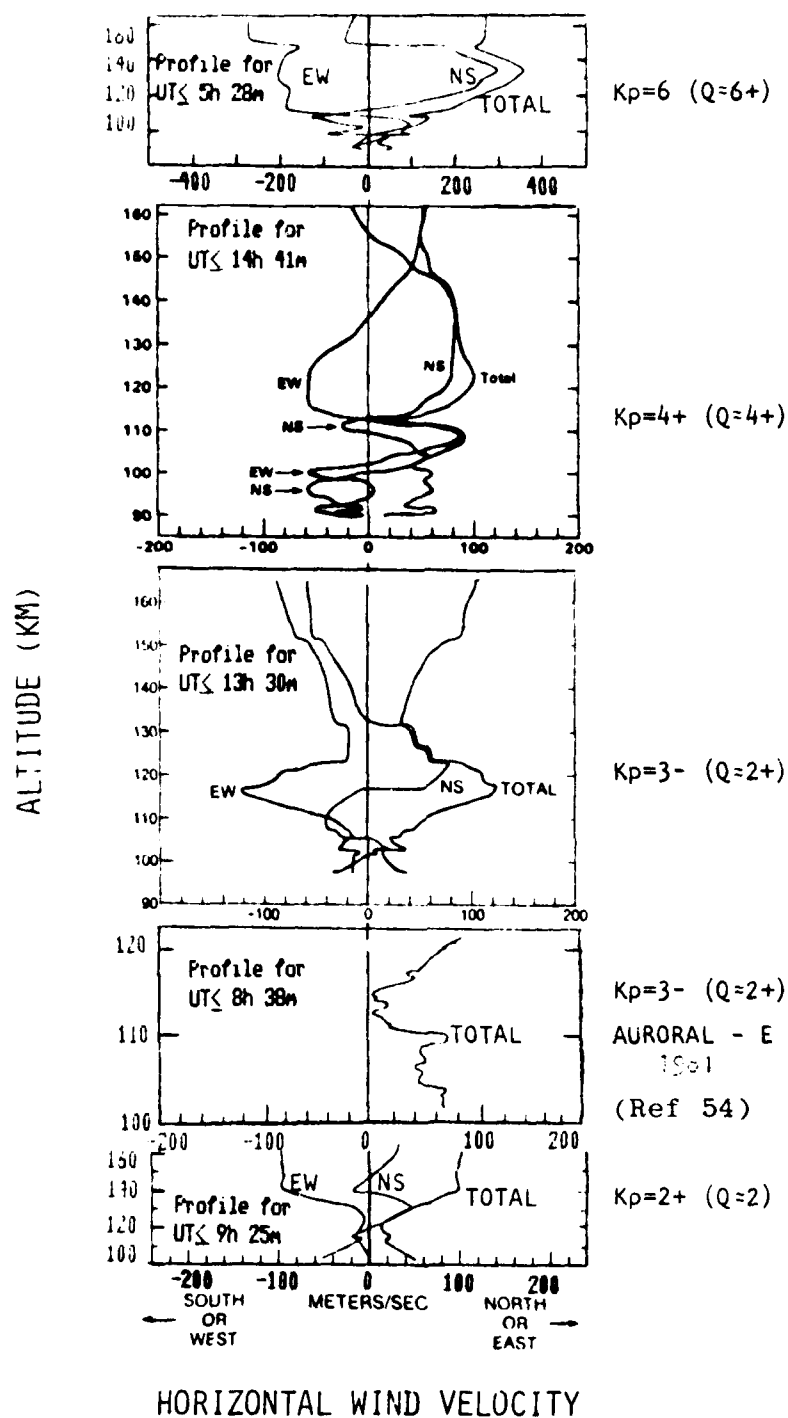
Figure 15. Typical wind velocity profiles and shear at auroral altitudes/latitude. (From Ref 53.)

68

energy deposition rate is less than τ -- solution of time-dependent transport equations is required. Note that the chemical reaction time and molecular diffusion coefficient both change in the same direction with altitude; and that diffusive transport depends only on $\sqrt{\tau}$ while the relative displacements by wind shear vary directly with τ and are thus relatively larger than diffusion at the lower auroral altitudes (although the spread is two-rather than three-dimensional).

As the energy deposition altitude decreases -- α and most-probable F increasing -- the infrared background clutter from NO more closely reflects the inhomogeneities present in the auroral particle beam. The above tabulations indicate the temporal and spatial structure of particle input that must be considered (or alternatively, neglected) in specifying an auroral model. They show that below approximately 125 km spatial smearing and distortion of the vibrational-radiation pattern is less than the usual measurements footprint, 1 km; on the other hand temporal components down to the nominal minimum sensor integration time of 1 sec are attenuated at all energy-deposition altitudes.

2.6.1.3. Spatial-Temporal Radiance Variations

The effects of aerochemical delays on infrared clutter are sufficiently important to merit re-emphasis, in particular as they impact CO_2 even more than NO background structure.

Pending availability of more accurate information, we prescribe calculating volume or column emission rates of NO^{+} radiation using a single time constant parameter τ, which is a function of altitude or α and independent of the absolute energy input rate. The average delay in infrared emission can be shown to be τ, and thus the average spatial offset of the radiation is at the position reached in τ .

69

Within their expected accuracy these τ's do not change with geophysical conditions. The single-pole linear integrating circuit will be recognized as an analog of this simplified aerochemistry model's exponentially-decreasing weighting of previous input:

```
                         R
particle     ———·  \ \——————————————○   volume or column
energy              τ(=RC)  ┬            emission rate of NO
input rate f(t)           ══ C          vibrational radiation.
or F(t)                    ┴
```
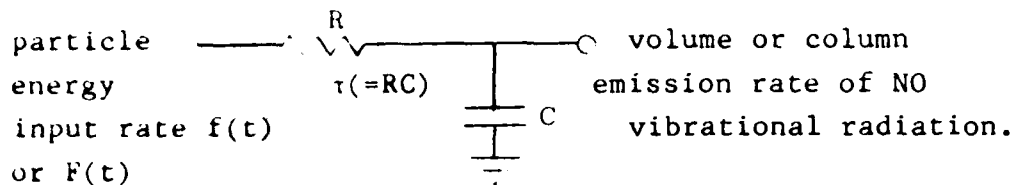
This calculation procedure is physically valid only when the spatial scale or correlation length of the energy input is large compared to species transport distances in characteristic chemiluminescence-output time τ; otherwise net inflow or outflow of reactants from the volumes in the sensor's field must be considered in predicting their infrared radiation rates. In those cases that the fractional change in energy input rate to a specified volume of air is $\ll 1$ over time τ and the scale length of this input exceeds the transport distance -- "equilibrium" auroral input in time and space --, Fig 14 directly gives the spectral yields from that volume. Aerochemical delay acting independently of mixing damps NO radiance variations with periods <1 sec at all auroral-excitation altitudes, and attenuates even 100 sec-period components of the infrared background at the higher tangent altitudes.

If the temporal PSD's (power at radian frequency ω) of the energy input F or f are known and mixing-transport can be neglected, the temporal PSD's of infrared output intensity can be determined by multiplying this distribution by the Fourier transform of the atmosphere's response to the input, $(1 + \omega^2 \tau^2)^{-1}$. Thus in this auroral case the statistics of temporal clutter in sky radiance can be straightforwardly

assessed. If the correlation length of energy input is so small that substantial physical transport between a typical sensor's instantaneous fields of view does take place within time τ, the temporal frequency distributions in these individual image elements (pixels) will be further affected. Calculation of the infrared radiance distribution in the general case -- auroral energy input rate varying in both space and time with scale less than τ -- requires solution of time-dependent transport equations with chemical depletion of species (for which a wind field model must be adopted).

Gradients in the spatial radiance distribution are reduced by the natural wind shear and (secondarily) diffusive transport of NO^+'s precursors during these chemical induction times, at scales indicated in the above tabulations and Figure 16. (While shear and turbulence may also enhance radiance structure in some view projections, the general tendency is toward smoothing.) Charged as well as neutral particles experience these offsets and spreading, since below ~140 km the collision frequency is sufficiently high to couple the wind drift and diffusion of the two types of species (that is, precursor ions such as NO^+ and N_2^+ are not confined by the geomagnetic field). Variations in the turbulent diffusion coefficient result in little error in the estimates of physical transport, because τ is small at the altitudes where natural turbulence occurs. In contrast to the spreading due to diffusion, the bulk distortions due to wind shear can be predicted only statistically (except, of course, when the actual shear profile has been measured). By analogy with the method mentioned above for calculating the power spectrum of temporal frequencies in the infrared background, the spectrum of spatial frequencies can be determined when the input spatial spectrum remains sensibly constant for time τ by constructing a spatial filtering function from model wind shear profiles (as in Fig 15) and the τ appropriate to each altitude.
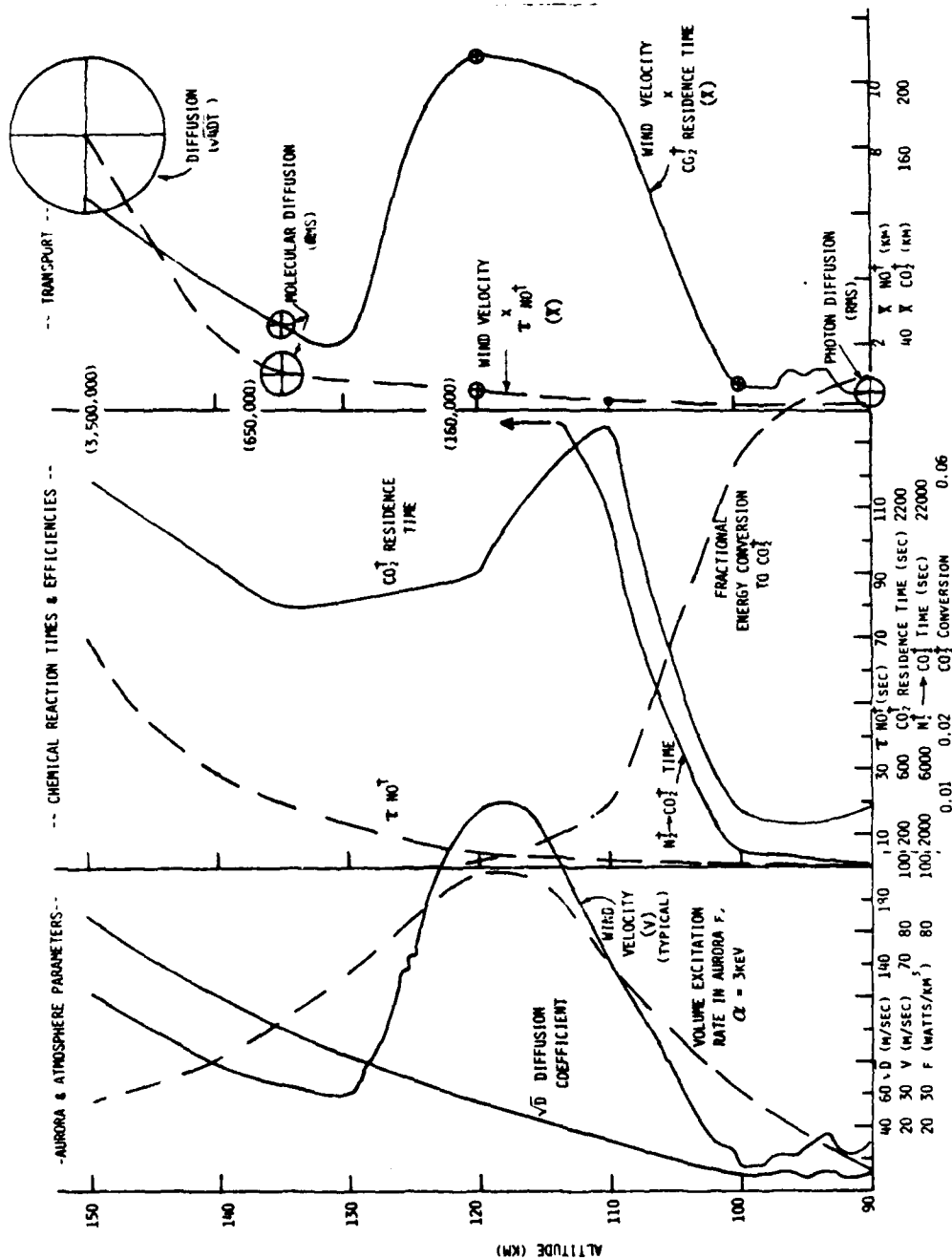
Figure 16. Altitude profiles of characteristic times for emission by NO^+ and CO_2 following auroral excitation (middle panel), and of transport of the precursor species (right panel). The model aurora and atmosphere parameters on which the calculations are based are given in the left panel.

72

2.6.1.4. Altitude Profiles

Figure 16 illustrates in a semiquantitative way the effects of aerochemical delays in emission on temporal and spatial radiance structure from $NO^\dagger$ and $CO_2^\dagger$ (to be discussed in Section 2.6.2). In the left panel are plotted altitude profiles of input parameters: $\sqrt{D}$, a model auroral-latitude (scalar) wind velocity, and the volume energy deposition rate f when $\alpha = 3$ keV (from Fig 10). (Note again the coincidence of high wind speed with high deposition.) τ and the analogous emission time of CO_2 vibraluminescence-transfer radiation, along with the initial efficiency of conversion of auroral particle energy to CO_2 vibrational energy, are plotted in the middle panel. The resulting altitude profiles of mean transport of the two infrared radiation sources are shown in the right-hand panel. Physically-reasonable values for the "transport length" that would be applied in the estimation of attenuation of spatial frequency components of scene radiance alluded to in the preceding paragraph, can be derived for desired view projections from these offsets. (For nadir sight paths, for example, weighting one-half the displacement over the actual particle energy deposition profile would provide a fair estimate.)

The increase with altitude of the spatial spread of chemiluminescent reactions works in the same direction as the decrease in photon yield per initial ionization (due to quenching of N^2D atoms by O, Ref 44), both reducing the power spectral density of sky radiance at the higher spatial and temporal frequencies. A closely similar effect is found for CO_2 4.3μm-band clutter (refer to Fig 16), O atoms again being the quenching agent. Since the atmosphere above auroral energy deposition altitudes is optically thin to NO vibrational radiation (even in very high zenith-angle sight paths), radiance distributions can be calculated by directly summing volume emission rate distributions. In contrast, absorption and re-

73

emission of CO_2 ν_3-band photons excited as a result of auroral particle impact must in general be considered in determining 4.3μm scene radiance (as is further discussed in Section 2.6.2).

2.6.1.5. Non-auroral NO Fundamental Band Emission

The vibrational-fundamental cascade spectrum in Fig 14a is always overlaid at its high-wavenumber (short-wavelength) end by thermal emission and earthshine scattering from the atmosphere's NO molecules in the (1,0) band (Ref's 44,45,46). A midlatitude limb spectrum of this component (at lower resolution, and on a logarithmic scale) appears in Fig 4; since [NO] is higher at high latitudes, presumably because of creation of NO molecules in aurora (Ref's 45,58), the thermal radiances would be expected to be higher viewing through the oval. Chemiluminescence in aurora can be looked at as producing "hot [vibrational] bands" of NO that extend the thermal background above 5.5μm (below 1820 cm^{-1}). It also increases the quiescent atmosphere's radiance within the (1,0) band's spectral range (to the extent discussed in Ref 46) and adds higher spatial and temporal frequency components to the infrared noise.

N atoms produced by solar photons also create $NO^{\dagger}$, by reacting with O_2 molecules at altitudes generally above the aurora. While this process results in much less (1,0) band radiation than thermal excitations, it is the principal source of NO overtone sequence radiation in the dayglow (as shown in in Appendix I, which also notes that the NO-fundamental "hot bands" are weak in the airglow).

2.6.2. Carbon Dioxide

Calculation of the background clutter from CO_2's (001-000) 4.3μm resonance transition (the ν_3 band) is further complicated by 1) two orders of magnitude longer mean interval

between initial energy deposition and infrared emission, 2) a strong dependence on altitude of the effective efficiency with which this energy results in vibrational excitation of CO_2 molecules, and 3) absorption and re-emission ot the radiation in the atmosphere. To determine surface radiances or even volume emission rates, coupled sets of equations that describe the time dependent radiation and excited-species transport must in general be solved; this is practical for only limited classes of auroral energy input geometries. Procedures for approximate solution of the photon diffusion equations (which do not consider the physical motion of the $N_2^\dagger$ precursor, which as we shall see has important effects on the radiance distributions) have been developed by AFGL (Ref's 60,61,62) and are summarized in the description of the BRIM method for calculating limb radiances in the 4.3μm band (Ref 18). As previously noted, the vibraluminescence of CO_2 that results from impact of energetic charged particles overlies emission excited lower in the atmosphere by thermal collisions, vibration transfer, and scattering of earthshine and sunlight (Ref 63); only the auroral component is explicitly discussed here.

Since the sky radiance distributions from transfer of vibrational quanta are broadly smeared in space and time, weak "prompt" 4.3μm excitation processes could dominate the background clutter at high frequencies. The important and still unresolved issue of other sources of radiation overlapping the CO_2 band mentioned in Section 2.5.1 is discussed in Section 2.6.2.3.

2.6.2.1. Excitation Transfer and Residence Times of Vibrational Energy

The collisional and radiative processes leading to 4.3μm vibraluminescence from CO_2 are shown in Figure 17; compare Fig 13 for the chemiluminescence of NO. We have attempted to make this review of these processes suffic-
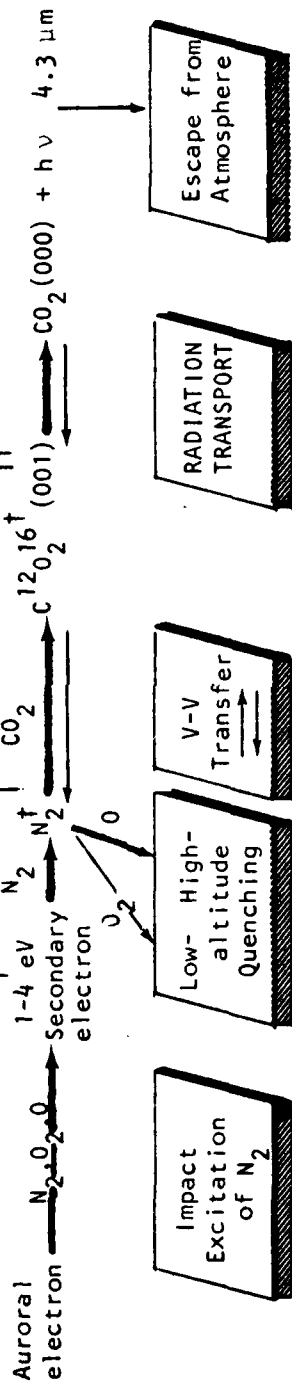
Figure 17. Schematic diagram of auroral excitation of CO_2 4.3μm vibra-luminescence and longer-wavelength radiations[2]. The principal reaction path is shown by heavy lines.

iently complete to illustrate and provide physical insight into the procedures for calculating the radiances from specified auroral energy input distributions, and to identify deficiencies in the information needed to provide useful scientific results. Actual application of these procedures requires substantial computational effort, and the original sources referenced should of course be consulted before such calculations are considered.

Table 4 lists characteristic times and probabilities of collisional energy transfer and direct photon escape at auroral altitudes. The entries were calculated using the temperature-dependent chemical reaction rate coefficients in Ref 64, O and N_2 concentrations from Ref 36's model atmosphere, and the geometric mean of the midlatitude CO_2 concentrations measured in daytime (Ref 65) and nighttime (Ref 66) rocket flights. The mass spectroscopically-measured CO_2 mixing ratio (listed in the second column) decreases by almost a factor 10 between 90 km and 150 km altitude; this profile, furthermore, would be expected to vary with latitude, as it depends on the mean solar elevation. Characteristic times for transfer of energy from $N_2{}^\dagger$ to CO_2 (in which the vibrational quantum is preserved; v-v in Fig 16) and O (in which it is converted to kinetic energy of translation), listed in the third and fourth columns, are of course inversely proportional to the actual concentrations of CO_2 molecules and O atoms at the latitude of the aurora.

The reactions are initiated by the excitation of N_2 molecules to vibrational states of their ground electronic state, principally by secondary electrons from impacts of the primary auroral electrons (thick line in Fig 17). About 8 vibrational quanta are believed to accompany each ionization of an atmospheric molecule or atom (somewhat fewer at the higher altitudes of energy deposition, where the relative concentration of N_2 decreases); this is an initial energy conversion efficiency of 7%, and is considered uncertain

Table 4. Characteristics of Transport of 4.3μm CO_2 Radiation*

Energy Deposition Altitude, km	$[CO_2]$, cm^{-3}**	Time $N_2^+ \rightarrow CO_2^+$, sec	Time $N_2^+ \rightarrow O$, sec	Fractional Initial $N_2^+ \rightarrow CO_2$	Photon escape probability***	Time $CO_2^+ \rightarrow N_2^+$, sec****	Time CO_2^+ quenched, sec	Time of N_2^+ residence, sec
90	2.0×10^{10}	55	6500	0.99	0.038(0.07)	0.021	11	370
100	1.9×10^{9}	625	3300	0.84	0.288(0.74)	0.13	64	370
110	6.5×10^{7}	21,800	3100	0.125	0.76 (0.95)	0.90	260	2710
120	1.2×10^{7}	1.6×10^{5}	1800	0.011	1	5	800	1780
135	3.8×10^{6}	6.5×10^{5}	1600	0.0025	1	30	1200	1600
150	8×10^{5}	3.5×10^{6}	2200	0.0006	1	90	1600	2200

*Physical transport of N_2^+ neglected.

**Geometric mean of midlatitude daytime and nighttime measurements, Ref's 65 and 66.

***In-band, directed into upper hemisphere (from Ref 61); estimated values using the CO_2 profile in Column 2 are in parentheses. Re-emission of initially downward-directed photons adds to the radiance.

****Radiative lifetime against emission of 4.3μm ($\nu_3 = 1$) photon = 0.00239 sec.

78

because it has not been directly measured. These $N_2^\dagger$ molecules transfer their energy in collisions with CO_2, which are near-resonant, or with O or O_2. Below about 80 km altitude the principal quenching species is O_2 (which in turn loses the vibrational energy in collisions with other molecules); as this reaction plays a very minor part in determining the 4.3 μm radiance of the auroral atmosphere it is among those in Fig 17 that have not been included in Table 4.

The fraction of vibrationally-excited N_2 molecules that excite CO_2, calculated from the rates of energy transfer in the third and fourth columns, is given in the fifth column. By 120 km altitude this fraction has decreased to 1%, so that the effective particle-energy conversion efficiency is only 0.07%; this shows that vibraluminescence of CO_2 is largely confined to the low-altitude end of auroral deposition profiles. The sixth column gives the probability that a ν_3-band photon initially directed into the upper hemisphere escapes the atmosphere without further absorption/emission (from Ref 61; our estimates using the CO_2 altitude profile in the second column, which is somewhat different from that in Ref 61, are in parentheses). Those photons initially directed toward the atmosphere's limb -- i.e., in the direction of equatorial-geosynchronous sensors -- have of course lower probability of directly escaping, and some of those directed downward are eventually out-scattered and so contribute to the sky brightness. As is indicated in Fig 17, some of the vibrational energy is radiated in "weak" infrared bands: ν_3 from molecules with isotopic composition other than $C^{12}O^{16}O^{16}$, which have longer mean free paths because the rotational lines do not line up with those of this most abundant isotope, and by branching into 9.6 and 10.4 μm and (in part through collisions) longer wavelengths.

The characteristic times for transfer of the vibrational quantum back to an N_2 molecule (seventh

column) or other collisional deactivation (eighth column) are long compared to the radiative lifetime of the CO_2 001 state, 0.00239 sec. Hence virtually all the $CO_2^\dagger$ molecules excited at auroral altitudes depopulate by radiating. (At lower altitudes, the vibrational quantum has a much higher probability of being transferred by collisions $CO_2^\dagger \rightarrow N_2^\dagger \rightarrow CO_2^\dagger \ldots$, or by 4.3$\mu$m-band radiation (or collision) $CO_2^\dagger \rightarrow CO_2^\dagger$.) The final entry in Table 4 gives the residence time of the quantum (Ref 60), which is in effect the e-folding time for escape of ν_3-band radiation from the atmosphere and so is analogous to the τ for exciting $NO^\dagger$ discussed in Section 2.6.1.

This residence time is the inverse of the sum of the rates of transfer of the quantum of energy from N_2 to

CO_2. increased for collisional transfers back to N_2 and corrected for probability of escape of the photon from the atmosphere, collisional quenching of $CO_2^\dagger$, and radiation in bands other than the 001-000

+ 0

+ O_2 (not important at auroral altitudes).

At energy deposition altitudes below 100 km this time is determined largely by the corrected $N_2^\dagger \rightarrow CO_2^\dagger$ transfer rate. The sharp falloff in $[CO_2]$ above this altitude (Table 4) then causes the residence time of the quantum to jump to near the time for its conversion to kinetic energy in collisions of $N_2^\dagger$ with O, ~2000 sec. As would be expected, this increase is accompanied by a rapid decrease in the probability of radiation from CO_2, and also by near-transparency of the overlying atmosphere to the ν_3-band photons (except in the longer limb paths). The "ledge" in effective energy conversion efficiency introduces spatial frequency components near 1/15 km^{-1} into the PSD's of vertical ν_3-band radiance (see Fig 16).

2.6.2.2. Impact on Background of the Conversion Efficiency and Residence Time

These residence times are of course ⎯gous to the times required for aerochemical reactions to ⎯te $NO^\dagger$, in that they quantify the duration of infrared ⎯ation output following particle energy input. Since they ⎯ two orders of magnitude longer, however, the $N_2^\dagger$ (and ⎯ precursor is moved two orders of magnitude farther ⎯pper-atmospheric winds and spread one order of magnitude ⎯ by turbulent and molecular diffusion. As the scale lengths ⎯uroral energy input are usually considerably less than this ⎯sport (typical values of which are shown in Fig 16), surface ⎯ance distributions can only rarely be calculated from a simple ⎯y-time formalism such as was prescribed for $NO^\dagger$, even from ⎯sition altitudes where the atmosphere is optically thin to ν_3 radiation. Wind shear can be expected to smear out ⎯ surface radiance spatially as much as the "random walk" of ⎯on diffusion at all auroral altitudes. (The rms horizontal ⎯ad from upward-directed 4.3 μm photons originating from a ⎯t source at 90 km is of the order of 10 km, and decreases ⎯ increasing altitude.) That is, atmosphere dynamics, which ⎯nly statistically predictable, has as much effect on the ⎯ground's spatial distribution as radiative transfer, which ⎯ least in principle) can be calculated from the absorption- ⎯ parameters and concentration profiles of the atmosphere's ⎯cules.

Since the probability that the vibra- ⎯al quantum will be quenched by O increases very rapidly ⎯e 100 km, the energy parameter of the auroral particle ⎯ plays a critical part in determining the CO_2 vibralum- ⎯scence intensities. Referring to the deposition profiles ⎯ig 10, we see that little auroral ν_3-band emission occurs ⎯ α is less than 3 keV. The radiances are obviously sensi-

tive to the $[CO_2]/[O]$ ratio, and indeed inaccuracy of these con-
centration profiles and in the transport calculations introduces
more uncertainty in the auroral brightnesses than the aforemen-
tioned uncertainty in the number of N_2 vibrational quanta initially
excited. (The lifetimes and yields in Table 4 were computed
for midlatitude CO_2 concentrations.)

As noted, quite detailed computations
that include the effects of physical and radiation transport are
required to predict CO_2 ν_3-band clutter statistics from even
the least spatially and temporally complex auroral energy input
distributions. At present there exists no "library" of results
of such calculations for naturally-occurring structured particle
fluxes in model atmospheric wind and turbulence fields.

2.6.2.3. Other 4.3μm Emission(s)

Despite the paucity of such calcula-
tions, it is obvious that this CO_2 vibraluminescence-transfer
radiation has negligible spectral power density at temporal
frequencies above $\sim 10^{-3}$/sec and horizontal spatial frequencies
above $\sim 2 \times 10^{-2}$/km (other than that due to horizontal structuring
of the ambient CO_2 and/or O concentrations, which is expected to
be small). Again only those inhomogeneities in the particle
energy input pattern having longer time and space scales need
be specified for calculations of the vibraluminescence background.

Such unstructured 4.3μm aurora
has been seen by AFGL's zenith-viewing spectroradiometers (as
reviewed in Ref 63). However, the diffuse enhancement seen by
spatially scanning (rotating side- and off-zenith-viewing) fixed-
band radiometers on two of their sounding rockets is overlaid
by a more localized component (Ref's 40,42,67). Additional
evidence for "near-prompt" 4.3μm-band emission is provided
by the EXCEDE spectrums, which show a factor three more radia-
tion than predicted from the times required for vibralum-

inescence transfer (Ref 68). This more closely correlated
emission, should it be verified by subsequent measurements,
would reflect the irregularities in energy input and so repre-
sent a potentially more important source of infrared noise.

Two excitation processes, electron
impact excited fluorescence of CO_2 and chemiluminescence of
NO^+ -- currently more favored --, have been invoked as the source
of this emission (refer to Table 5). $NO^{+\dagger}$ would be excited
in the exothermic reactions following initial ionization of air

$$N_2^+ + O \rightarrow NO^{+\dagger} + N \qquad \text{and}$$
$$N^+ + O_2 \rightarrow NO^{+\dagger} + O$$
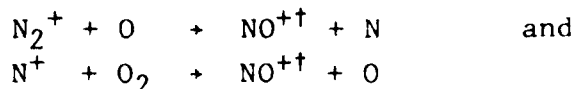
and, with less probability

$$N_2 + O^+ \rightarrow NO^{+\dagger} + N \qquad \text{and}$$
$$NO + O_2^+ \rightarrow NO^{+\dagger} + O_2.$$
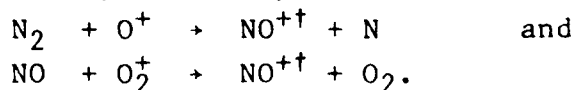
Characteristic times for completion of the first two atom-
interchange reactions are estimated in Table 5 from their rate
coefficients ($\sim 2 \times 10^{-10}$ cm^3/sec to all states of the
products) and the auroral atmosphere's concentration of O atoms
and O_2 molecules These time scales are considerably shorter
than those for NO chemiluminescence, as the rate coefficients
for the ion-neutral reactions are higher than that of neutral N
with O_2 (and no intermediate reactions are thought to be
involved). Only insignificant spatial and temporal smearing
of the radiance distributions would result from these short
delays. The measurements to date on artificial (Ref 68) and
natural (Ref's 42,67) aurora did not have sufficient resolu-
tion to quantify the temporal and spatial correlation between
energy input and "near-prompt" 4.3 μm radiation(s).

Similarly, existing data do not have
sufficient spectral resolution to identify the radiating species.
Figure 18 shows the calculated spectral intensities (at ~ 11 cm^{-1}
resolution) from each excitation process, normalized to the
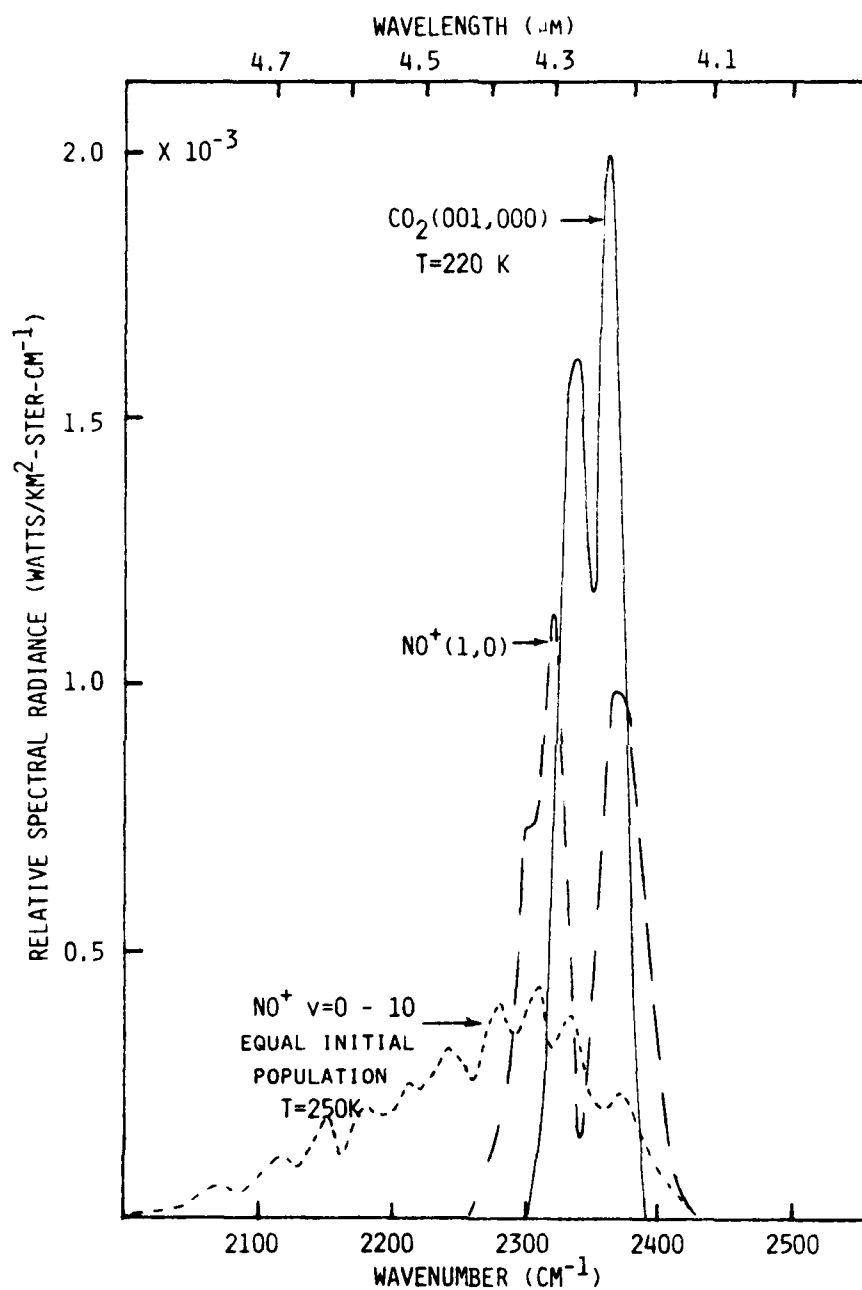
Figure 18. Relative radiance distributions in the CO_2 ν_3, NO^+ (1,0), and NO^+ fundamental bands, each normalized to a total output of 1 watt/4π sterad-km^2. Resolution is 11 cm^{-1}. Refer to the text for the estimated band efficiencies.

84

Table 5.   Expected Properties of Near-Prompt 4.3μm Radiation

	CO_2 fluorescence	NO^+ chemiluminescence
Emission Spectrum (see Figure 18)	Essentially same as CO_2 ν_3 from thermal excitation or vibraluminescence	Spread to higher and (especially if high vibrational states are populated) lower wavenumbers
Time Delay	2×10^{-3} sec (lifetime of 001 state)	~0.01 sec at 100 km, 0.1 sec at 120 km
Altitude Dependence of Yield	Increases downward because of increase in relative CO_2 concentration	Decreases downward below ~110 km due to quenching (Ref 67) by N_2 (Ref 69)

same total energy yield. If the NO^+ ions are all produced in
their first vibrationally-excited state the emission spectrum
is somewhat broader than CO_2 001-000 at 220K rotational temper-
ature, and as higher initial states are populated more less-
energetic photons are emitted. (Collisional quenching, which
becomes less probable as v increases (Ref 43) was not considered
in the cascade spectrum of NO^+ initially excited to v = 1-10.)
The wider spectral interval of this background has implications
in design of measurements sensors that operate in the short-
and long-wavelength wings of the ν_3 band. The spectral
distribution of emission from CO_2 in Fig 18 may also be used
in auroral vibraluminescence calculations.

BRIM adopts an energy yield of 0.3%
above 110 km altitude in this prompt 4.3μm-band radiation, on

the basis of radiometry data from 1978 auroral probe IC 807.15
(Ref 67); a figure of 0.2 - 0.5% was derived from the 1974 probe
A18.219-1 (Ref 42). As the time scale of the feature is expected
to be <1 sec (Table 5), we have included it in the plot of air
fluorescence (Fig 12), spread over ~70 cm^{-1} with spectral
detail omitted. The total band yield is estimated as 0.3% above
110 km, 0.1% at 100 km, and 0.04% at 92-1/2 km energy deposi-
tion altitude on the assumption that the radiation is due to $NO^{+\dagger}$
being quenched by N_2 molecules (Ref 69). The spectral yields in
Fig 18 have been normalized to a total output of $(1/4_\pi)$ watts/
steradian (from a column or volume), so that radiances or
volume emission rates can be calculated for specified energy-
deposition input rates and assumed radiation process. We note
that if the prompt 4.3_μm-band component is 001-000 emission
from CO_2 some of the photons will be absorbed in the atmosphere,
and therefore the radiative transfer methods alluded to in
Section 2.6.2.2 must be applied in calculating the sky radiance
distributions that would be measured from exoatmospheric altitudes.
Also, if it is from an NO^+ vibrational cascade originating
in part below 110 km, the high-wavenumber end of the spectral
distribution will be less intense than shown in Fig 18 because
of preferential quenching of the lower vibrational states.

With an energy conversion efficiency
of 0.3% above 110 km deposition altitude, a limb radiance of
10 w/km^2 ster in the optically thin emission band is reached
when the input flux rate is 1000 w/km^2 (best-fit α = 1.6 keV).
All spatial and temporal frequency components (above the mini-
mum scales in Table 1) in aurora with mean F >1000 w/km^2 would
be required to specify the sky background clutter in this
spectral feature.

2.7. Specification of Spatial and Temporal Input Structure

The review of infrared air fluorescence and chemilum-

inescence in Sections 2.5 and 2.6 indicates the input-structure
information needed for modeling occurrence of clutter back-
grounds. Insofar as the output (radiance) structure is speci-
fic to the input distribution, the upper limit of sky noise that
can be tolerated is not precisely defined (the 10 w/km^2-ster
minimum-mean is a "soft" boundary), and the radiance is sensi-
tive to intercept latitude or spherical angle λ (or λ') through
the van Rhijn factor, the minimum power spectral densities do not
lend themselves to a straightforward tabulation. A brief summary
of input requirements, which carries the assumption that inhomo-
geneities need be considered only when the mean auroral-sky radi-
ance is above the aforementioned threshold, is as follows.

Fluorescence of N$_2$ results in weak backgrounds extending
over the 2-1/2 - 7µm wavelength band (Fig 12). As the emis-
sion rate follows the energy input rate with negligible delay,
all the temporal and spatial frequency components must be speci-
fied when the input rate is above threshold. At a maximum van
Rhijn gain factor of 40, reached when θ is 8.81° - 8.84° and λ'
is near 77-1/4° (Fig 6), the radiance in a ~ 1/2µm spectrum
interval reaches 10 w/km^2 ster at input flux about 50 kw/km^2.
A further condition here (which of course also applies in com-
puting the maximum brightnesses of the other infrared features)
is that the flux remains at least this high over a ~ 1000 km
atmospheric path in the sensor field. For other intercepts on
the auroral-emission layer the minimum F at which frequency-con-
tent information is needed will of course be higher, indeed
considerably so at most latitudes/longitudes (as Fig 6 shows).

Nitric oxide chemiluminescence is principally at 5.3 -
6.2µm and 2.7 - 3.1 µm (1900 - 1600 and 3700 - 3300 cm^{-1};
details are in Fig 14), with a much higher energy conversion
efficiency. The threshold F is about 2/3 kw/km^2 (overtone) or
1/4 kw/km^2 (fundamental) when the sight path is at the maximum
van Rhijn factor of 30; these figures refer to a best-fit α near

87

1-1/3 keV. Again this condition can apply only over a narrow range of tangent intercepts, with higher thresholds over most of the auroral oval. At this worst case, temporal frequency components below $\sim$ 1/30 sec^{-1} and spatial frequency components below $\sim$ 1/3 km^{-1} need be specified for input rates greater than $\sim$ 1/2 kw/km^2; higher frequencies are severely attenuated by the chemical delay and accompanying species transport. Particle fluxes above 5 kw/km^2 (best-fit α = 3 KeV), which result in above-threshold radiances at angles $\lambda' > 69°$, would call for frequency components below 1/3 sec^{-1} and 3 km^{-1} (which would be reduced to 1 km^{-1}, as the minimum measurements sensor footprint is 1 km). Fig's 11, 10, 6, and 16 and the tabulations in Section 2.6.1 provide the data for further estimates of the maximum spatial and temporal frequencies at which power spectral densities of the energy input are needed to predict the occurrence of background clutter in the NO vibrational bands.

Carbon dioxide vibraluminescence at 4.22 - 4.30μm has little spectral power at frequencies above 10^{-3} sec^{-1} and 2 x 10^{-2} km^{-1} (horizontally) under any auroral input conditions. As was shown in the previous section, a model of the occurrence of sky background in the as-yet-unidentified (or validated) "prompt 4.3μm" emission would require specification of all frequency components when $F > 1$ kw/km^2 (again, only in the narrow range of o or λ'). If the radiation proves to be due to NO$^+$, the effect of the decrease in average energy-conversion efficiency as α increases (because of increased collisional quenching at lower energy-deposition altitudes) is to be considered in determining the minimum input flux rate at other intercepts.

The above figures are intended to establish semi-quantitative limits to the input structure detail needed for a model of infrared clutter. They underscore the ideas that the highest temporal and spatial frequency components needed vary inversely with the lowest characteristic emission time and that

88

the minimum particle flux that need be included (for a given
wavelength band) depends rather critically on the sensor
field's elevation angle θ or its intercept λ'. These limita-
tions on requirements serve to guide future measurements of
the occurrence and noise spectrums of auroral energy input.

2.8. An Occurrence Model

We proceed now to outline a first-generation model of
the distribution of infrared radiance and its structure in
measurements sensors' slant-path lines of sight. The sophis-
tication of the model is commensurate with the scope and quality
of the input data reviewed in Sections 2.2 (probabilities of
particle energy input) and 2.5 and 2.6 (aerochemistry and
atmospheric transport). It can of course be refined as better
input information becomes available from new measurements
and analysis of existing data bases.

We take the auroral oval (Section 2.2.1) to be the
locus of occurrence of all particle energy input fluxes that re-
sult in above-threshold sky background. The latitudinal extent
of this region can be determined from the measured magnitude of
the disturbance of the geomagnetic field, as described below.
Real-time as well as historical data on these field variations
are available. In addition, the probabilities of input flux
intensity are also taken as varying with the magnetic distur-
bance. That is to say, both the spatial location of occurrence
of aurora and the absolute probability distribution of auroral
particle input within this occurrence region are assumed to cor-
relate with the change in net magnetic field at the earth, and
to depend on no geophysical parameter other than local (mag-
netic) time.

Before proceeding, we point out that the "auroral oval"
concept is somewhat arbitrarily defined (refer to the discussion

89

in Ref 70) in terms of probability of appearance of diffuse particle fluxes generally well below those that excite above-threshold infrared noise, and that some energy input occurs outside its boundaries. Nonetheless, insofar as it contains the regions where discrete areas of high flux are most probable (Ref's 14,71) and the occurrence of these higher fluxes is roughly proportional to that of the weaker flux component (Ref 72) (with the proportion increasing toward the equatorward edge (Ref's 72, 73)), the oval seen in groundbased all-sky and meteorological satellite images represents the optimum geometry for a first-generation model of auroral infrared sky backgrounds.

2.8.1. Auroral Activity Index

The variations in the earth's field are routinely measured with magnetometers at stations worldwide and applied to form several numerical descriptors of the level of magnetic "activity" (Ref's 74, 75, 76), the best known of which is the global (subauroral-latitude) index Kp. The Auroral Activity Index (or Polar Range Index) Q has been found to provide a good statistical prediction of the extent of auroral particle input (Ref's 77, 78), as has the AE index (Ref 79). We choose to apply Q to characterize the oval because it is more commonly used.

Q is a quasi-logarithmic expression of the maximum deviation of one horizontal component of the earth's magnetic field at auroral latitudes (Ref 75). It is intended to measure currents in the ionosphere near the station, which have less effect on the vertical component of the field vector. As might be expected, Kp and a Q derived from a series of western-hemisphere stations are statistically correlated (Ref's 34, 80; they also have nearly equal numerical values), despite the fact that the two disturbance indexes refer to different latitudes

and possibly field directions. Numerical values of Q extend
from 0 ($<10^{-3}$ fractional change in the field) to 9 ($\sim 10^{-1}$)
and in very rare cases higher. The dimensions of the auroral
oval shown in Fig 9 refer to Q = 3, a nominal "average" magneto-
spheric-disturbance condition. As a typical time scale of
change in particle-input activity is of the order of 1/4 hr,
an ideal Q would be calculated from the excursions of the
magnetometer signals four times each hour.

Probabilities of occurrence of Q at a single
auroral-latitude station and the distribution of duration of
periods over which Q exceeds fixed values are shown in Figure 19
(from data in Ref 81). Just after solar minimum the Q-indexes
cluster around 2, while after solar maximum they become spread
to higher values. The systematics data in Ref 81 and the monthly
and yearly Q averages listed in Ref 82, along with data on
occurrence and persistence of Kp (in surveys such as Ref 83),
would be used to determine the statistics of oval size and flux
occurrence. "Instantaneous" oval locations can be found from
15-min Q indexes reported by civilian agencies.

2.8.2. Dimensions and Location of the Occurrence Region

The boundaries of the auroral oval, which our
model considers as hard-edged limits to the input-occurrence
region, are located in so-called corrected geomagnetic lati-
tude - magnetic local time coordinates (Ref's 78, 84, 85). The
average equatorward geomagnetic latitude ϕ_E^* is fit to a pre-
cision of about 1/2° by a simple analytical expression (Ref 78)
$$\phi_E^* = 72 - 0.9 \, Q - 5.1 \cos (H^* - 12),$$
where H* is magnetic time in degrees measured eastward from mag-
netic midnight (defined in Section 2.2.5; H* and its relationship
to geomagnetic longitude ψ^* are described further in 2.8.1.1)
and the other numerical quantities in the formula are in degrees.
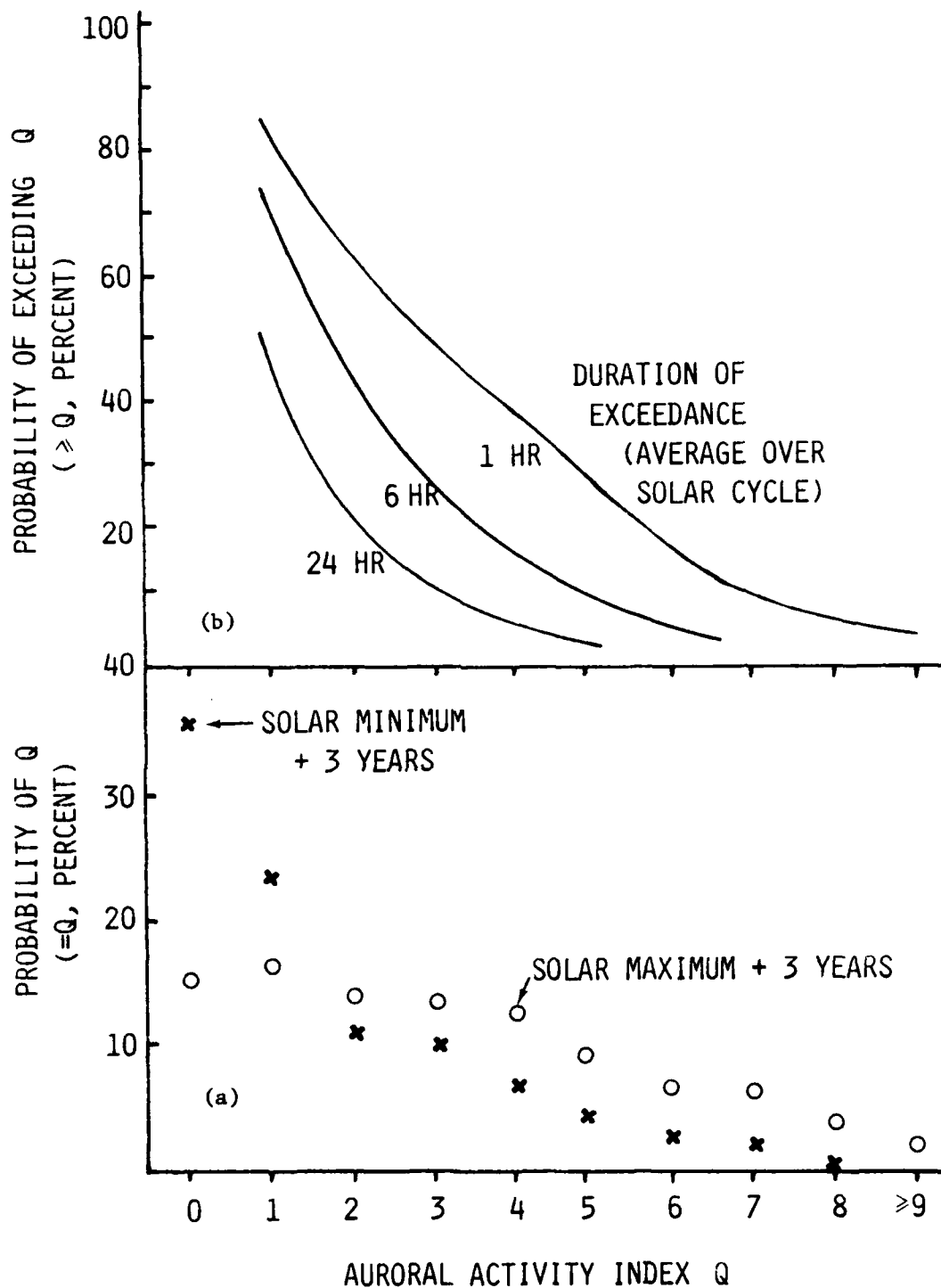
Figure 19. Probabilities of occurrence (a) and distribution of duration of exceedance (b) of auroral activity index Q.

Thus the outer boundary of occurrence is represented by a circle
around a rotating center offset 5.1° from the geomagnetic pole
(in the direction away from the sun), whose radius increases by
0.9° of latitude per unit Q.

The poleward boundary ϕ_P^* does not depend on
Q in such a simple way, and in addition its center is offset from
that of the equatorial boundary. The data from all sky camera
and meteorological satellite images can be fit (Ref 84) to <1° by

$$\phi_P^* = 90 - J_1 - J_2 \cos (H^* + J_3),$$

where the parameters $J(Q)$ are (again in units of degrees)

Q	J_1	J_2	J_3
0	15.2	2.4	12
1	15.9	2.7	11
2	16.1	2.5	7
3	16.2	1.9	0
4	16.3	1.4	-4
5	16.4	0.8	-9
6	16.7	0.4	-13
(7	16.8	0	-17)
(8	17.0	0	-21).

The figures in parentheses for Q = 7 and 8 are our extrapola-
tion of the results of Ref 84, which presents higher order
parameters for an improved fit to the data. To within the
expected accuracy of our model the extrapolation to higher Q
should be adequate and a closer fit is not justified.

In this regard, we point out that the mean
equatorward boundary of the "diffuse-appearing" aurora in
meteorological satellite images has a scatter of ±2° when
plotted against Kp or the magnetic-disturbance index AE (Ref
79). Hence a more conservative backgrounds model would increase
the area of occurrence by lowering the constant term in the
expression for ϕ_E^* by 2° (to 70°) and the J_1's in ϕ_P by 1°.

2.8.2.1. Conversion to Geographic Coordinates and Universal Time

Corrected geomagnetic latitude-longitude and local time (which is related to longitude) form a natural coordinate system for auroral occurrence. Measurements sensors, on the other hand, could also be expected to operate in geographic latitude-longitude and Universal Time. Hence a conversion between these two coordinate systems is needed to determine the range of ϕ', ψ' over which intercept paths through altitudes where infrared emission can take place pass within the region where energy input occurs.

In practice this coordinate transformation has been done principally by analog methods (such as in Ref 85), as the earth's magnetic field's large departure from a simple dipole at high latitudes requires tedious computations to achieve even $\pm 1/2°$ precision. Indeed, we have not identified in the literature a digital subroutine suitable for immediate adaptation into an occurrence model. A look-up table of sufficient accuracy can be compiled from the latitude-longitude plots in Figure 20 (taken from Ref 86) or the analog auroral-oval plotter in Ref 85. (Such a table is currently in use at Air Force Geophysics Laboratory (Ref 87).)

Geomagnetic local time H^*, the hour angle between the magnetic meridian ψ^* and the anti-subsolar (or midnight = noon + 12 hrs) magnetic meridian ψ_0^*, requires similarly tedious (albeit conceptually simple) computations. Since the position of the sun moves relative to the pole at a fixed local solar time H, H* depends on day of the year, and hence on the solar declination, which is tabulated in ephemerises such as Ref 88 (and also Ref 133). H* can be calculated using the look-up table, as described below, or found by the analog method of Ref 85. Alternatively, after ψ^* of the desired intercept point has been looked up, it can be determined from the equation (adapted from Ref 89)

94
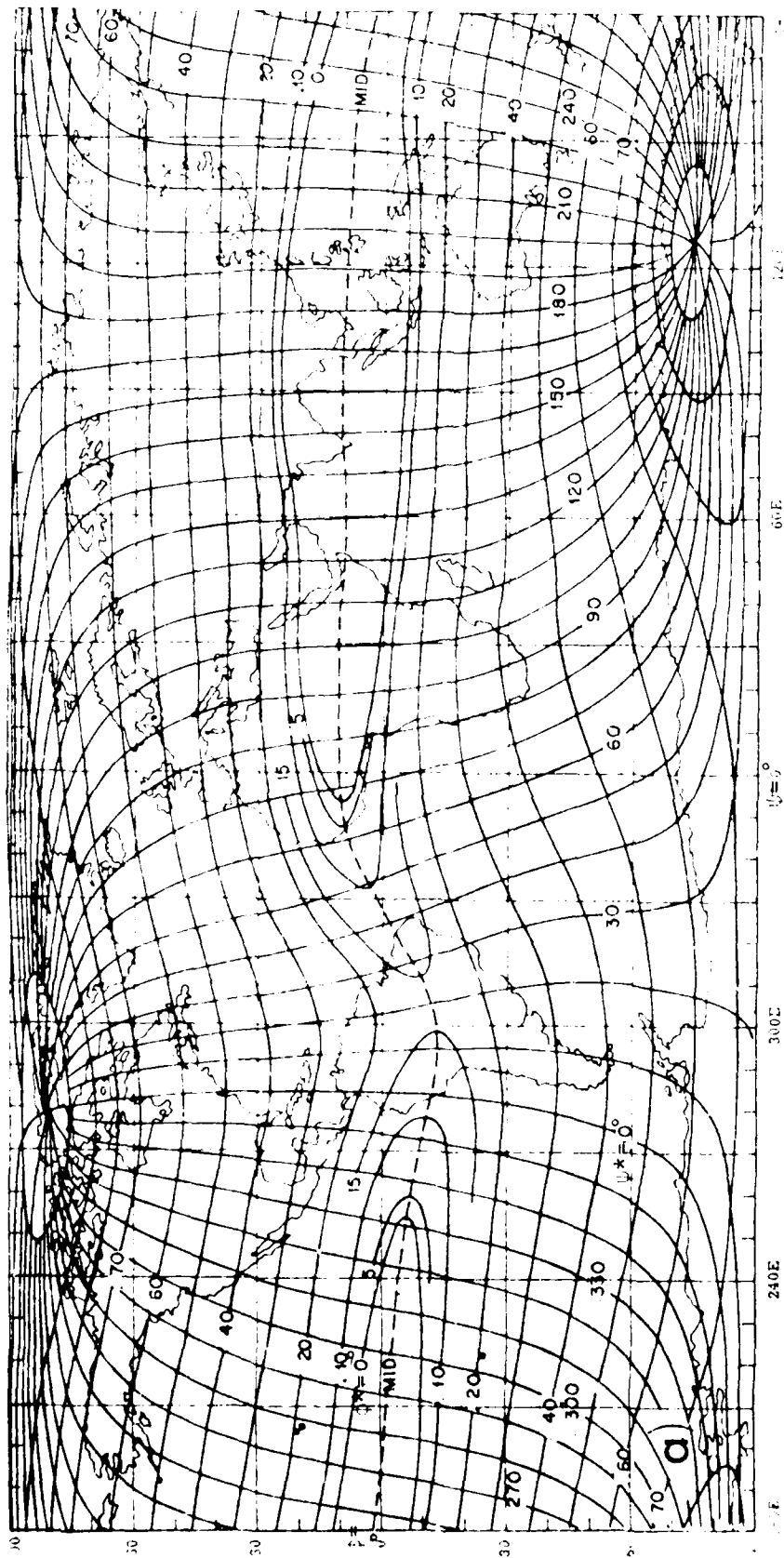
Figure 20.   Geomagnetic coordinates (ϕ^*, ψ^*, thick lines and lettering) plotted with geographic coordinates (ϕ, ψ, thin lines). (a) Global, cylindrical equidistant projection, for calculating H^*; (b) north polar, azimuthal equidistant projection; (c) south polar. (From Ref 86.)

95

MICROCOPY RESOLUTION TEST CHART

NATIONAL BUREAU OF STANDARDS 1963 A

b)

c)

97
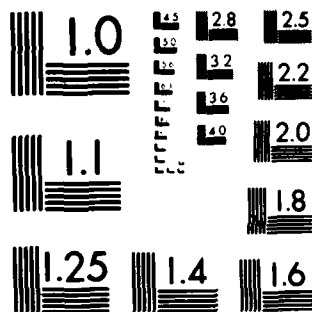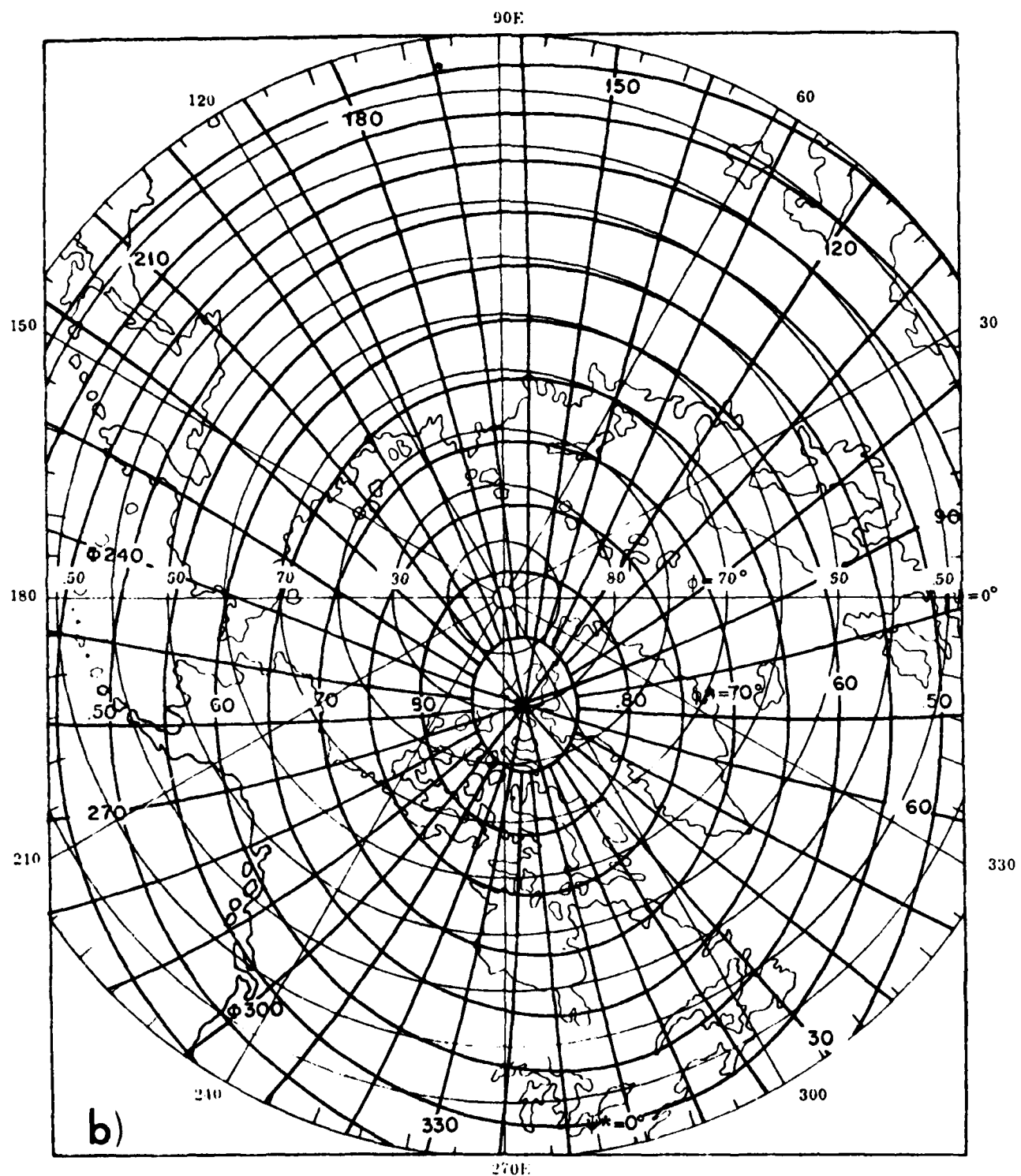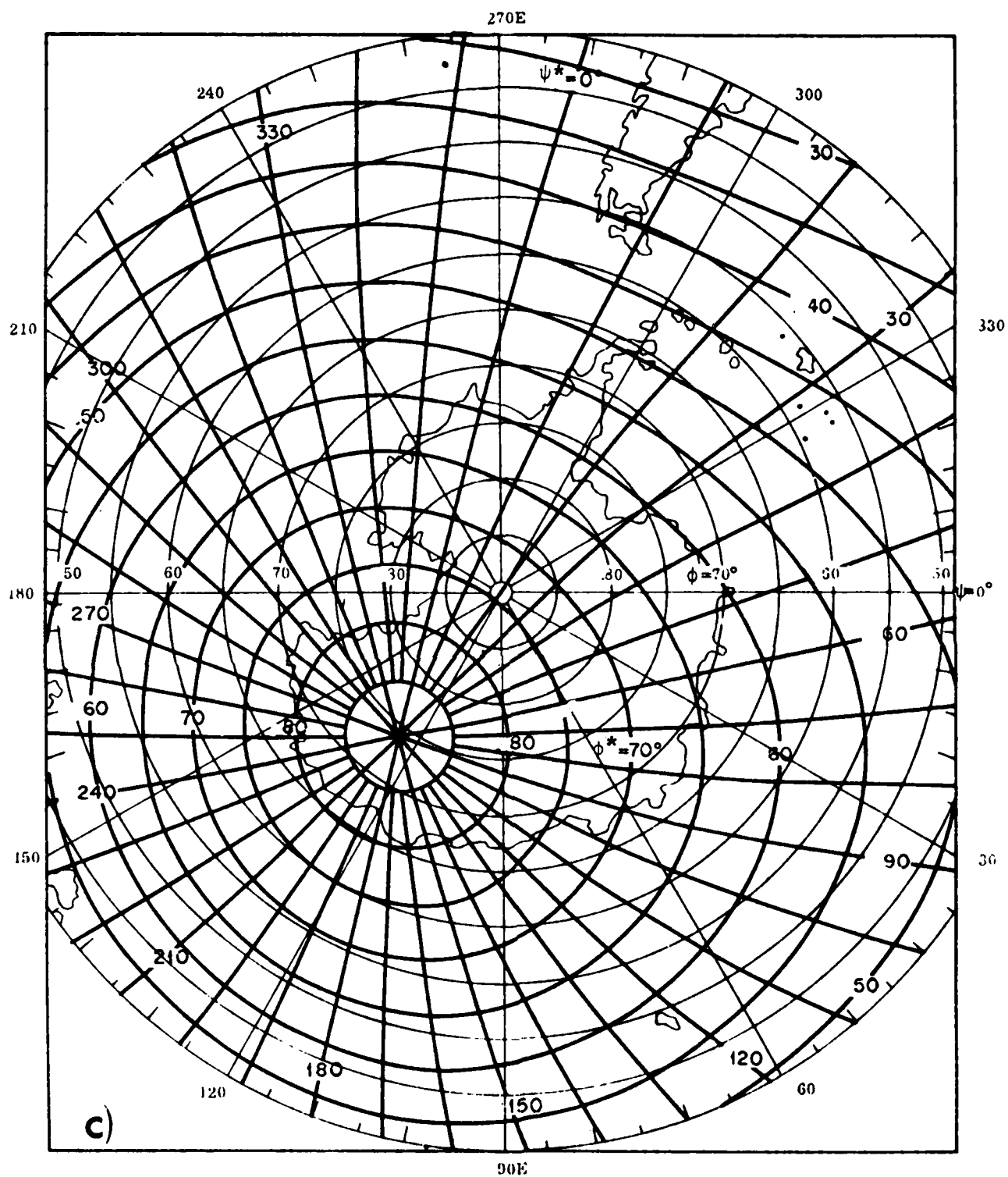
$$H^* = \psi^* - \psi_0^* = \psi^* -$$

$$\sin^{-1}\left[\cos(\text{Dec})\sin U/\{1 - (a_1\sin(\text{Dec}) - a_2\cos(\text{Dec})\cos U)^2\}^{1/2}\right].$$

Here (Dec) is the solar declination angle and $U = \psi - H + a_3$;
H and ψ are positive eastward, in degrees ($H(\psi)$ is found from
UT as described in Section 3.2.7). The constants, which are
derived from the latitude and longitude of the geomagnetic
axis poles, are

	Northern hemisphere	Southern hemisphere
a_1	0.984	0.961
a_2	0.174	0.276
a_3	81°	234°.

H^* at a given UT and ψ^* (from the
look-up table) can also be determined by locating the geographic
coordinates of the overhead sun (from an ephemeris) and finding
$\psi_0^* + 12$ hrs through the look-up table. First the subsolar
point's longitude (local noon, $= 15°(\text{UT} - 12)$) and latitude (from
the ephemeris; absolute value always $< 22\text{-}1/2°$) are found,
and then the geomagnetic coordinates of this subsolar point are
looked up (in a compilation from Figure 20a). Then

$H^* = \psi^* - \psi_0^* = \psi^* -$ (geomagnetic longitude of noon) + 12.
These H^*'s, or alternatively the ψ^*'s(H^*, UT), serve to locate
the poleward and equatorward latitude boundaries of the auroral-
input region.

The procedures described here lend them-
selves to digital implementation. Although they may not repre-
sent the optimum strategy for a clutter model, their develop-
ment illustrates the mechanical problems and serves as an intro-
duction to the literature on conversion between geomagnetic
(auroral-occurrence) and geographic (measurements-systems)
coordinates.

2.8.3. Occurrence Within the Oval

As was pointed out in Section 2.2, probabilities

of line-of-sight occurrence in near-limb paths at all directions
relative to the local geomagnetic latitude lines (or oval
boundaries) are needed. We look once again at the existing
data to determine how closely this input requirement can be met.

2.8.3.1. DMSP Images

The most useful reduced data on fre-
quency of occurrence of column energy input come from the Defense
Meteorological Satellite Program (Ref's 15, 17). These polar-
orbiting, sun-synchronous satellites build up images of the
visible and near-infrared air fluorescence from a raster scan
traverse to their ~800-km orbital path with a nominal resolu-
tion of ~2 km at the nadir and ±56° (~2500 km across)
angular field.

About 750 DMSP images containing both
oval boundaries were analyzed for auroral "activity" as a func-
tion of Kp (Ref 90). In most of these data H* = 0-2 hrs at
the spacecraft's nadir, and all are from winter months (when
scattered sunlight does not obscure the fluorescence). A quali-
tative activity-classification scheme was applied, which with
the help of the DMSP calibration in Ref 91 can be made semi-
quantitative. The results, which apply to the oval as a whole
rather than individual vertical columns, are summarized in Fig-
ure 21. The classification Quiet means that the input fluxes
are well below nominal threshold. Moderate means presence
of some discrete auroral structure with column intensities up
to a few times the mean shown. The Active category includes
scenes with high brightness over most of the longitudinal seg-
ment of oval within the radiometer's field of view, some of
them overexposed in the the photographic reproduction of the
sky brightness distribution. (Some of the DMSP image data are
also available in digital form.)
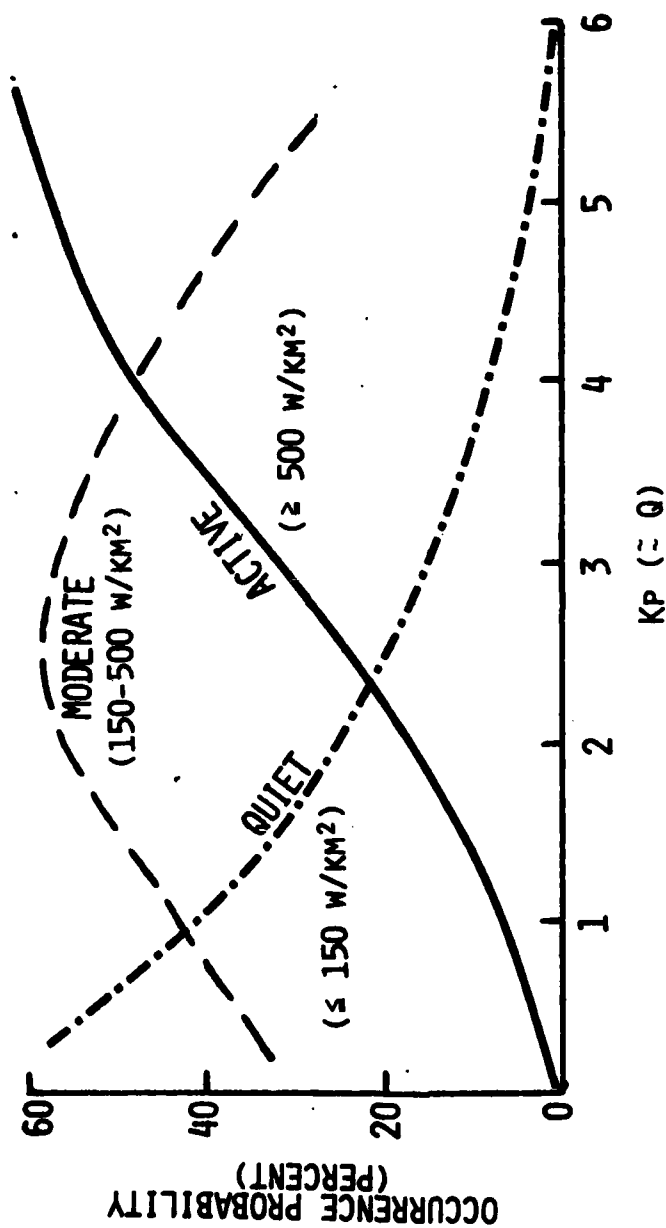
Figure 21. Frequency of auroral activity as a function of Kp determined from DMSP images (from Ref 90), with estimates of occurrence of zenith flux.

It is clear that this analysis gives only very low resolution information about large-area, much less localized, occurrence of energy input. The intensity resolution within the Active category can be improved by applying the results of a study with a groundbased high-sensitivity video camera of discrete bright forms (narrow arcs) when Q was between ~3 and 6 (Ref 92). About an order of magnitude more 10^4 - 10^5 w/km^2 events were observed in the magnetic zenith than 10^5 - 10^6 w/km^2 events. (The fact that fewer 10^3 - 10^4 w/km^2 events were reported is most probably an artifact of the sensitivity of the camera and the definition of a discrete auroral feature.)

2.8.3.2. Other Data

None of the other surveys of auroral particle fluxes, air fluorescence distributions, or ionospheric electron densities have been analyzed to produce directly-applicable data on probabilities of energy input.

The following data bases contain input-occurrence information, of varying degrees of spatial and intensity resolution. (The references are intended to identify the data sets, and discuss other results from the experiments.)

- --DMSP particle spectrometry (Ref 24)
- --OGO-4 particle spectrometry (Ref 73)
- --ISIS particle spectrometry (Ref 93)
- --Injun-5 particle spectrometry (Ref 29)

- --DMSP images (Ref's 17, 79, 84, 90)
- --ISIS images (Ref 71)
- --Dynamics Explorer images (Appendix III)
- --All-sky camera images (Ref 84; also Ref 13)

- --S3-4 Satellite UV photometry (Appendix III)
- -- Aircraft photometry (Ref's 32 and 33).

101
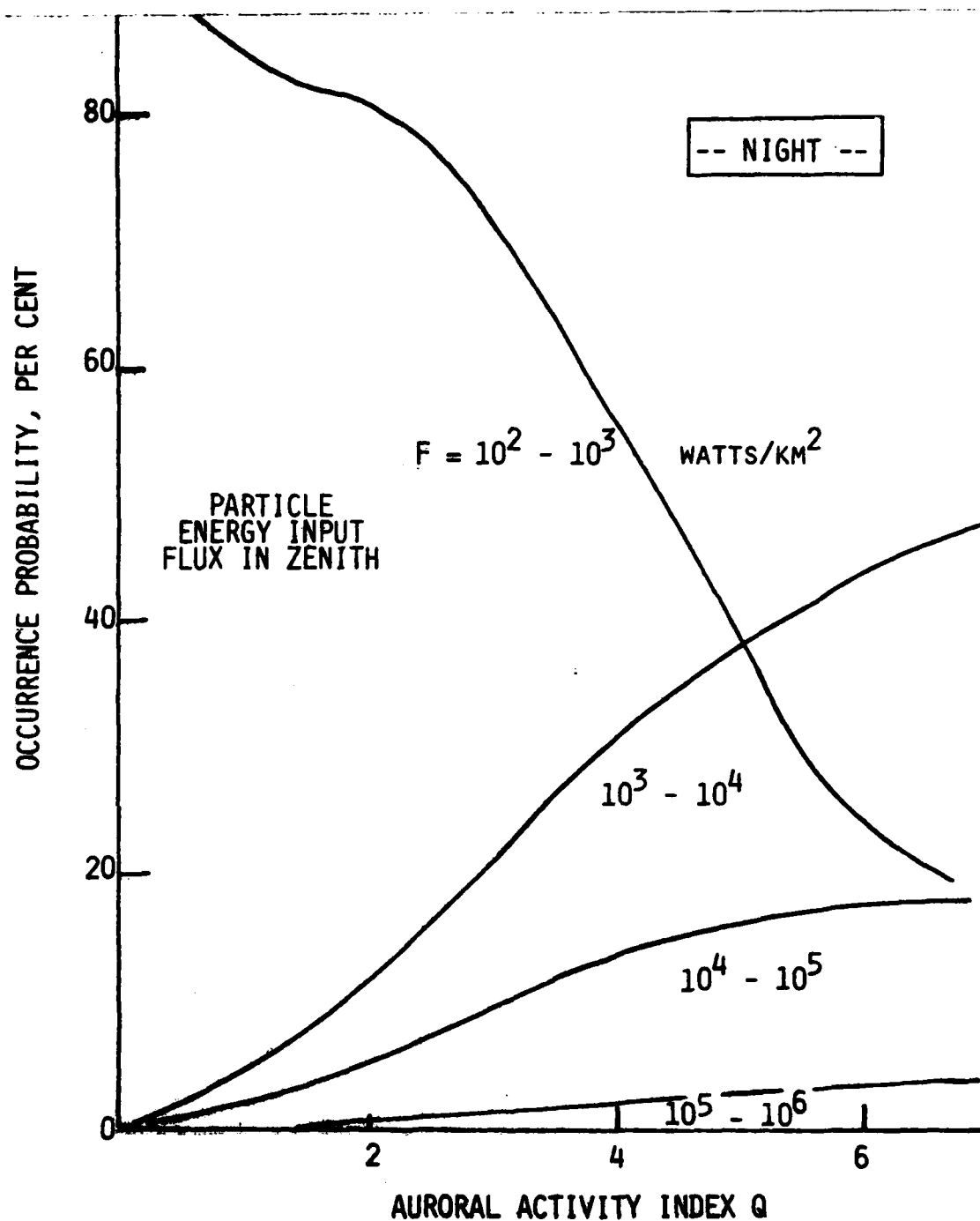
Figure 22. Estimated probabilities of occurrence of zenith energy input rate within the nighttime auroral oval.

Image data are particularly effective, as they allow correlation lengths to be determined for calculating column inputs in slant paths. Systematic survey data not explicitly referenced in the literature would also be expected to be on record (as mentioned in Section 2.4.3). These would include meridian photometer scans and all-sky images from auroral observatories, and electron density profiles measured with ionosondes and the higher lateral spatial resolution incoherent-backscatter radars (in particular, the unit until recently at Poker Flat Research Range (Chatanika), Alaska).

2.8.3.3. Zenith Occurrence

It is clear that the data now available permit only a rough estimate of the occurrence probabilities of zenith column input rates $F(Q, H^*)$. Such an estimate, derived principally from Ref's 90 and 92 and a qualitative review of the particle spectrometry and aircraft photometry data is in Figure 22. The large uncertainty even at this one-decade intensity resolution gives impetus to further auroral surveys and to analysis of the above-mentioned existing data bases. To use Fig 22's estimates in an occurrence model, the probabilities would be re-plotted against F at fixed Q's and the resulting curves smoothed.

To within their expected accuracy these occurrence probabilities apply at all latitudes and geomagnetic times within the nighttime oval (notwithstanding the increased probability of high F and α toward its equatorward edge and near midnight (Ref 73)). During the daytime the average particle flux in discrete aurora is an order of magnitude less than at night (Ref's 70, 94) and the characteristic energies are also substantially lower within what has been defined as the oval (Ref 70). Hence we prescribe reducing Fig 22's probabilities of input fluxes $>10^3$ w/km^2 by a factor 10 when H^* is between 0600 and 1800 hrs. (That is, for purposes of the model the auroral oval is divided into two input-occurrence zones.)

2.8.3.4. Slant-Path Input

Energy input into the oblique sight paths from measurements sensors depends on the scale or correlation length of the zenith-column inputs. As was pointed out in Section 2.2.3, this scale length tends to be long in the direction(s) parallel to the oval's boundary, so that high input rates would be more probable at some intermediate-longitude intercepts. Near the measurements nadir the correlation lengths in the direction of the instrument field tend to be smaller, and therefore the total column input rates may be better approximated by the sum of independently-selected volume energy inputs. The path-lengths within the oval -- truncated van Rhijn factors -- depend on its width and location (that is, on Q and UT) as well as on $\phi^\prime$, $\psi^\prime$ and the measurement sensor's longitude; refer to Fig's 9 and 6.

Pending availability of information on these position- and orientation-dependent scale lengths and in view of the large uncertainty in the estimates of occurrence of vertically-directed particle flux, we prescribe calculating slant-path inputs with the assumption that F remains constant within each oblique field. This approximation overestimates the number of very high and very low input rate occurrences (Section 2.2.3), and thus the model (conservatively) overstates the exceedance probabilities at high sky backgrounds.

2.8.3.5. Temporal and Spatial Structure

The accuracy of the computed column input rates is much too low to derive useful structure information from differences between neighboring fields or times. We specify that instead PSD's of the form discussed in Section 2.2.4.2 be used to characterize the temporal variability. As these spectrums were derived from near-zenith auroral radiances, we are making the further assumption that they apply also in near-limb

fields of view. The power spectral densities at outer scale
and in the secondary peak are to be taken as proportional to
the calculated mean energy input rate.

A very preliminary estimate (Ref 95) of
the spatial PSD can by made from analysis in progress of DMSP
image data (Ref 17). The spatial spectrums in these near-nadir
projections appear similar to the temporal spectrums (without
the secondary peak), with the power per unit frequency decreas-
ing as $(frequency)^{-(2 \text{ or } 3)}$. We assume that this behavior holds
also in all other (including near-limb) projections, as well as
in all directions relative to the oval's boundaries; and that
the absolute spectral densities are again proportional to the
mean input flux rates. (Note that we have also taken the noise
in the airglow to be proportional to mean column intensity
(Section 3.5).)

2.8.4. A First-Generation Auroral Clutter Model

Figure 23 is the flow chart for a model of
occurrence of mean intensity and spatial-temporal structure
of the infrared sky backgrounds excited in aurora. Following
the approach stated in the introduction to Section 2, the ener-
gy input into individual elements of the sensor's field is first
computed and then the aerochemistry is applied to calculate radi-
ances in emission features or spectrum intervals. The framework
does not attempt to consider explicitly attenuation of higher
frequencies in the chemiluminescent output for specific complex
input patterns (Sections 2.6.1.3-4), but rather applies the prin-
ciples developed for less general cases. In addition it omits or
simplifies some of the technical issues that we have raised, to-
ward making the model's detail commensurate with the standard of
information available about probability and scale lengths of par-
ticle input (Section 2.8.3) and chemistry and transport of pre-
cursors of infrared radiation output (Section 2.6).
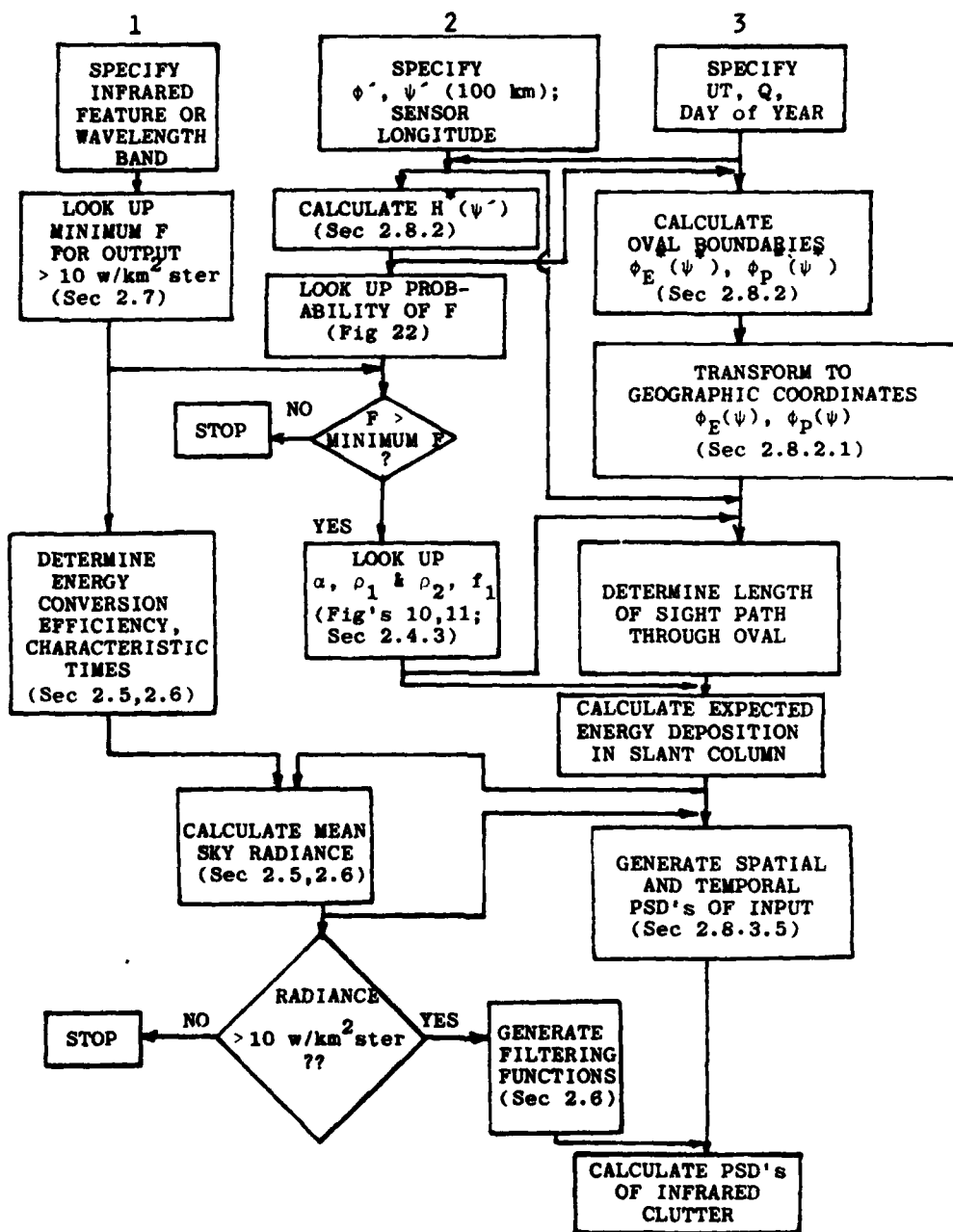
Figure 23. Flow diagram for a first generation model of occurrence of auroral infrared background clutter.

The model calls for selection of an emission feature or wavelength/wavenumber interval (column 1 in Fig 23); position of the field intercept ϕ', ψ', which is taken at 100 km altitude to accomodate sight paths that pass above the solid earth (column 2; the sensor's nadir is again taken as the reference longitude, except for calculating magnetic time); and auroral activity index and Universal Time of the measurement observation, with day of year (needed to determine H*; column 3). Following first down column 3, the boundaries of the auroral oval -- the sole region where energy input occurs -- are calculated in corrected geomagnetic coordinates using a procedure such as prescribed in Section 2.8.2 and then transformed to geographic coordinates (Section 2.8.2.1). All remaining calculations are made in this exoatmospheric sensor-oriented coordinate system.

The boundaries of this occurrence region are taken as extensions of the lines from the earth's center through the oval's boundaries at zero altitude $\phi_E(\psi)$, $\phi_p(\psi)$, that is, as vertical "walls". (The small inclination angle of the particle-guiding magnetic field lines is neglected.) Next the day-or-night condition is determined from H*$(\phi',\psi',$ UT$)$ and a zenith energy flux F_1 is input to the calculation. Probability of occurrence of flux is taken from the refinement of Fig 22 suggested in Section 2.8.3.3. (If the sight path extends through both the day and night ovals separate calculations are F_1 made for the F assigned to each sector.) The best-fit α for (from Fig 11) defines the FWHM altitudes $\rho_1 - R$ and $\rho_2 - R$ of the volume energy deposition rate f_1. Energy input is then either approximated as extending in altitude between ρ_2 and ρ_1 with a constant volume deposition rate, or fit by an altitude profile of f_1 from Fig 10 (which involves somewhat greater, but not burdensome, computational complexity).

107

If F_1 is below the minimum that results in threshold radiance in the selected infrared feature when the van Rhijn factor has its maximum allowed value (as determined from Section 2.7), the calculation is terminated. In this regard, the location of the oval's boundaries, and thus Q and H*, impose constraints on the maximum possible sight path length which further reduce the limiting F. Flags applying this idea could be incorporated into the logic to reduce the time needed to compute distributions of background occurrence probabilities and exceedances for sets of values of the input conditions F, ϕ', ψ', Q, UT, and infrared feature or spectrum interval. (Another flag is shown later in Fig 23.)

The deposition profile and auroral oval boundaries determine the length through the occurrence region of the sight path that intercepts the point ϕ', ψ' at 100 km altitude. Summing f_1 along this path gives the total particle-energy deposition within the instrument field. The relative altitude profile of the total energy input into oblique fields is to a satisfactory approximation the same as would be derived from the best-fit α. This procedure applies the above-stated simplification that the zenith flux F_1 and volume deposition rates f_1, once chosen as part of the input conditions, remain constant in the (potentially-long) slant path. It also sets to zero the energy input in those segments of the sensor's spatial scan that do not cut through the three-dimensional occurrence region.

The model then brings in the energy conversion process to determine the radiance and modification of the input irregularity structure. Absence of time delay and a narrowly-varying altitude profile of yields simplifies considerably the calculation of fluorescence intensities (Section 2.5, and also 2.6.2.3 -- "prompt" 4.3 μm emission). A geometric mean of the energy conversion efficiencies at altitudes ρ_2 - R and ρ_1 - R is a more than satisfactory approximation to the average efficiency

over the deposition profile. When the mean sky radiance exceeds Table 1's threshold -- rare for fluorescence of N_2 --, its spatial and temporal power spectrums are calculated as described in Section 2.8.3.5. (Further zenith-input spectra are in Ref 96.) These spectral densities will be directly proportional to those of the energy input.

For NO chemiluminescence, the occurrence model assumes that the correlation length of energy input perpendicular to the slant-path column is large compared to the mean lateral transport distance during one or two characteristic reaction times. (BRIM (Ref 18), which considers input distributions having variable F along the oblique path, makes the same assumption.) Thus "cross-talk" between adjacent sensor fields due to mixing or shear is neglected. τ is then determined from α and the mean radiance is calculated from the F's extending backward for time $1-2\tau$, following Section 2.6.1.1. Power at temporal frequencies ω in the input power spectrum is multiplied by $(1 + \omega^2\tau^2)^{-1}$ (to an adequate approximation the spectrum could be simply truncated at $1/\tau$), and a spatial frequency filter is created and applied as suggested in Section 2.6.1.4.

2.9. Discussion

In view of the large number of variables on which the background radiances depend, a substantial volume of calculations is needed to generate probability distributions of auroral infrared noise. Hence further flagging algorithms, including rapid termination for sight paths that miss the oval (or if F_1 or the energy conversion efficiency into the feature is low, have short paths through it), and perhaps even further simplifications of the inputs model, are highly desirable.

As noted, the occurrence model is designed to be consistent with the quality of its input information. Hence it does not treat some of the issues raised in Section 2.2, such as the

anisotropy and "periodicity" (or persistence) of auroral flux
patterns. The major data shortcomings are in the probability
of particle energy deposition -- particularly, into the near-limb
sight paths through auroral latitudes/altitudes from geosynchron-
ous sensors --, the irregularity structure of this input power,
and the statistics of lateral transport of precursors of NO chem-
iluminescent and CO_2 vibraluminescent emissions. These geophysics
factors appear to overweigh the uncertainties of the aerochemistry.

Several other aspects of the model's development merit
mention. None of the many surveys of aurora has explicitly
addressed the question of occurrence probability of vertically-
directed particle flux at specified latitudes-longitudes-times;
same information about this issue can be extracted from existing
data bases. Since the infrared column output is in general speci-
fic to its three-dimensional energy input pattern, calculations
of radiance distributions can be expected to be time-consuming
(except, of course, for fluorescence). Qualitatively speaking,
the most intense sky backgrounds would be expected at those inter-
cepts where the sensor's field has long pathlengths through the
oval at altitudes ~90-130 km that roughly parallel the lines
of geomagnetic latitude. The incoming particles' energy distri-
bution also plays an important part in determining the background
intensity and its spatial-temporal variability. Thus informa-
tion about spatial scale lengths and energy parameters of the
zenith auroral flux is as important as the vertical-flux occur-
rences themselves.

3. Airglow Infrared Background

The fundamental vibration-rotation bands of the hydroxyl radical's ground electronic state (Ref 97) are by far the principal 2-1/2 - 7µm airglow feature. Sky backgrounds due to chemiluminescence of other minor species -- NO, NO_2, and O_3, estimated in Appendixes I and II -- would be at most comparable to the 10 w/km^2-ster minimum even in limb projections, and as noted have so far not been detected in the upper atmosphere.

An "airglow" component of the CO_2 ν_3-band vibraluminescence is also present (as briefly noted in Section 1.2). It results from collisional vibration transfer $OH^\dagger \rightarrow N_2^\dagger \rightarrow CO_2^\dagger$ (Ref 63, 98) and thus reduces the hydroxyl emission intensity. This excitation of CO_2 (001) proceeds at rates comparable to absorption of earthshine plus thermal collisions in the ~80 - 87 km layer where $OH^\dagger$ is produced. The overlying atmosphere is optically thick to the rotational lines of the $C^{12} O_2^{16}$ ν_3 band from these altitudes (see Table 4), particularly so in the limb, making the residence time of a vibrational quantum ~400 sec (Ref 62). Hence exoatmospheric sensors do not directly "see" inhomogeneities in the luminescence-transfer component, but may detect the glow as a broadly smeared -- in space and time -- enhancement of the thermal radiance in the ν_3 band. (At night this radiance totals about 4 w/km^2 ster at 80 km tangent intercept (Fig 4)). The energy transfer process contributes little to the much higher daytime limb intensity, which is due to fluorescent scattering of sunlight, or to the similarly higher nadir intensity (Fig 3), which results from temperature (doppler) broadening of the rotational lines. The hydroxyl emission-rate variations reviewed here would of course apply directly in detailed calculations of the atmosphere's 4.3µm radiance. In view of this low intensity and absence of structure, however, we have not expressly considered the airglow component of CO_2 ν_3 background.

The so-called Meinel bands of OH include $\Delta v = 9$ to $\Delta v = 1$ transitions that extend from $0.38 \mu m$ (P branch of 9,0) to almost $5 \mu m$ (R branch of 9,8) (Ref 99). About 1/4 of the power ($\sim 1/3$ of the photons) is emitted in the $\Delta v = 1$ sequence at wavelengths above $2-1/2 \mu m$. The spectrum of these fundamental bands has not been directly measured in the atmosphere; only some uncertain balloon data on its short wavelength end exist. In Section 3.3 we derive the expected absolute spectral distribution in the zenith, which is shown in Figure 24. This "best-estimate" mean spectrum is prescribed for all geophysical conditions and view projections; that is, for purposes of the background-occurrence model it is applicable to all emission altitudes, temperatures, and quenching-species concentrations. Table 6 lists the best-estimate mean zenith radiances in individual bands of the sequence. Note the pronounced minimum between the (9,8) and (4,3) and the concentration of the hydroxyl emission between 2800 and 3500 cm^{-1}. The mean total fundamental-bands radiance is 13 w/km^2 ster in the zenith, and the limb maximum (as shown in Section 1.4.2.1) would be close to 1×10^3 w/km^2 ster.

While a substantial literature exists on the hydroxyl airglow, it is nonetheless inadequate for producing a high-accuracy model of the natural infrared clutter. We will review pertinent elements of this data base to provide a perspective on the input information needed to upgrade the occurrence model developed. A brief overview of the major features of the airglow appears in Table 2.

3.1. Excitation

The reaction widely considered to be responsible for most or all of the chemiluminescence (Ref's 100,101) is

$$O_3 + H \rightarrow OH^\dagger \ (v \leqslant 9) + O_2 + 3.34 \text{ eV.}$$
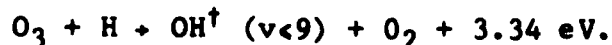
OH Meinel bands are emitted in the radiational (-collisional)

112

Table 6. Mean Zenith Radiance of Hydroxyl Fundamental Bands

Band	Origin,* μm	Radiance Ref 99, kR	Radiance from Data Base kR	w/km^2 ster
9,8	4.470	11.2	32.2 ± 13.2	1.14
8,7	4.141	5.4	7.5 ± 4.7	0.28
7,6	3.867	0.63	0.66 ± 0.32	0.027
6,5	3.633	0.57	0.46 ± 0.08	0.020
5,4	3.429	6.2	6.9 ± 1.5	0.32
4,3	3.248	20.8	42.3 ± 5.8	2.05
3,2	3.085	45.3	27.2 ± 1.8	1.42
2,1	3.937	86.9	60.0 ± 8.3	3.23
1,0	2.801	148	79.8	4.49

* Q branch. R branch is toward shorter wavelengths,
  P toward longer.

cascade of the OH† radicals to their ground state. The fact
that the highest vibrational level energetically accessible
is the highest upper state observed in spectrums of the night-
glow supports this mechanism. Some further support is provided
by the calculated concentration profile of H atoms (which
result from photodissociation of water vapor) and the measured
profile of ozone molecules (from recombination of O with O_2).
The H + O_3 reaction rate coefficient has been recently found to
vary as exp(-480/T) down to at least 196 K (Ref 102), which is
typical of the mesosphere; this temperature dependence varies
the reaction rates and layer radiance much more than the $\sqrt{T}$-
dependence (derived assuming zero activation energy, Ref 103)
that has been used in earlier models of hydroxyl emission.

A second reaction, yielding a different initial vibra-
tional population distribution has been proposed (Ref 104):

Figure 24.

Mean nadir (or zenith) spectral radiance distribution of the hydroxyl-fundamental airglow, averaged over 10 cm⁻¹ intervals.

115

$$HO_2 + O \rightarrow OH^\dagger \ (v< 6) + O_2 + 2.4 \pm 0.1 \ eV.$$
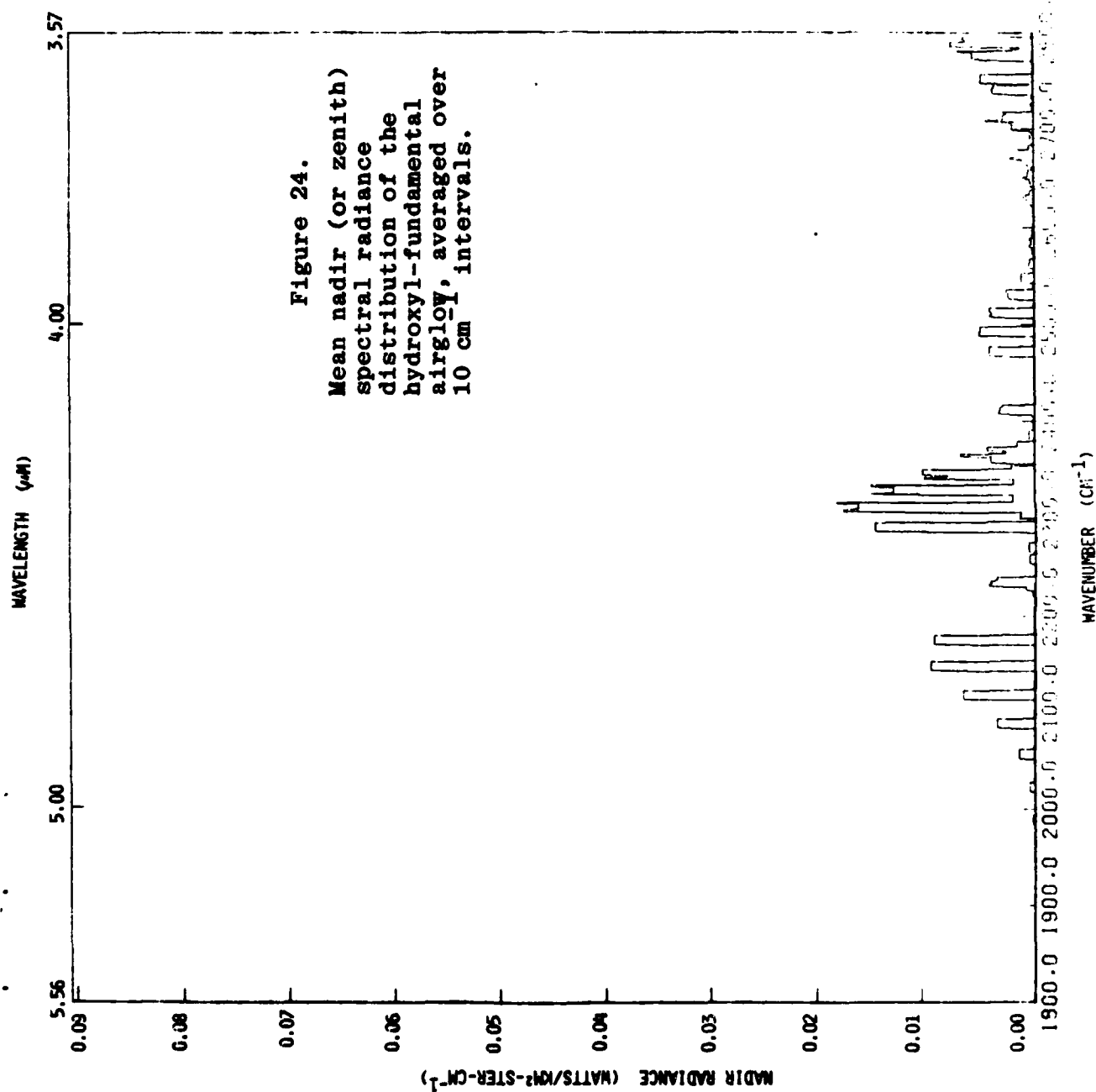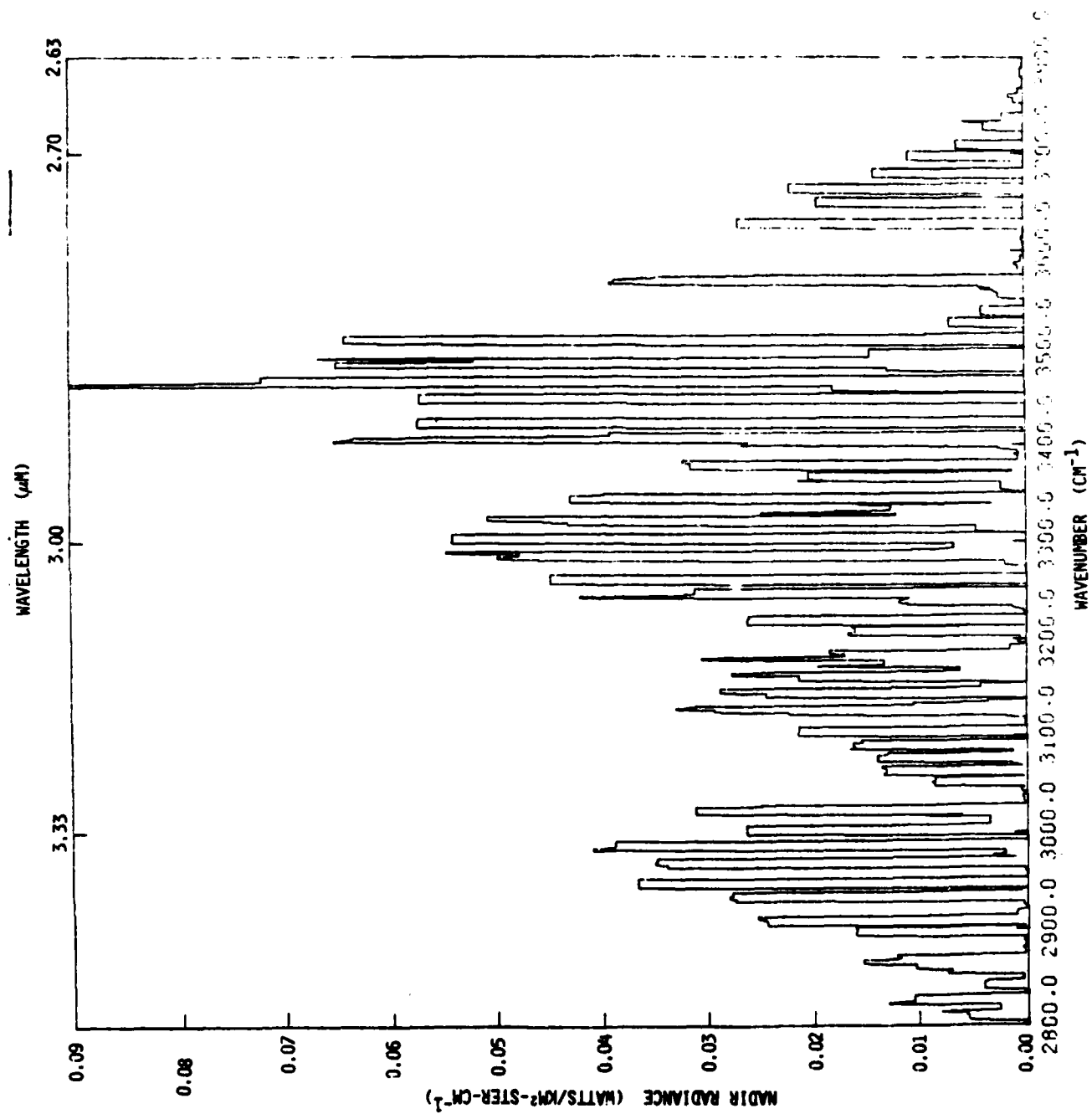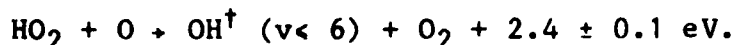
It is thought to contribute principally to the dayglow (Ref 105) at altitudes extending below those where most of the nightglow has been found (by rocket radiometry). The two reactions would in general result in different temporal-spatial variations of column emission, and also in a difference between the altitude profiles of hydroxyl emission originating from higher ($v = 7,8,9$) and lower ($v <6$) vibrational states. Both types of effect could of course also be caused by v-dependent collisional quenching. Some such differences have been reported (Ref's 106, 107, 108), while other measurements have not detected these effects (Ref's 109, 110, for example). Thus the contribution of the HO_2 + O reaction can not be considered substantiated, and furthermore its principal impact would be in the daytime when thermal emissions from the limb at OH $\Delta v = 1$ wavelengths are an order of magnitude higher than at night (refer to Fig 4). In any case, the zenith-intensity occurrence model and spectral distribution we have derived from the data are independent of the specific hydroxyl production mechanism.

Several attempts have been made to construct models of the photochemistry and vertical species transport that fit measured hydroxyl radiance variations (for example Ref's 109, 111,112, and 113). As uncertainties still exist in the radiational transition probabilities, quenching rate coefficients, and number densities of participating species (and even temperature dependence of the H + O_3 reaction rate), the results of such efforts are by and large inconclusive. Deactivation of $OH^\dagger$ by molecular nitrogen (cross-sections for which were most recently reported in Ref 114) is evidenced by the above-mentioned observations of energy transfer to CO_2.

van Rhijn sight-path factors for $\rho_2 = 87 + R$ km, $\rho_1 = 80 + R$ km are shown in Fig 6. The mean volume emission rate per unit spectral interval or in each band would be 1/7 the

116

average zenith radiance from Fig 24 or Table 6. A nominally
more accurate limb radiance profile could be derived from
Gaussian or parabolic volume emission rate profiles (Profile
A of Ref 10 makes about the best fit to the existing set of
rocket measurements). In view of the inherent uncertainty of
the spectrum and the variability and perhaps "waviness" of the
actual profile (Section 3.5), however, the rectangular shape
is adequate for predicting the atmospheric background.

3.2. Radiance Variability

Total column emission rates in near-infrared Δv = 3,
4, and 5 OH bands can be readily measured at night from ground
stations, and thus many long-period surveys of the airglow have
been made. In contrast, the altitude profile has been measured
from less than a dozen rocket probes, which have not served to
determine its systematics.

Consumption of O_3 (H atoms are recycled) would pre-
dict a continuous decline in hydroxyl radiance through the
night, which is observed at low latitudes (Ref 115,116) but
much less frequently elsewhere. Models incorporating one-
dimensional transport, which advect reactants with a variable
eddy diffusion coefficient (Ref 117), have reproduced some of
the measured diurnal variations, such as the often-seen rise
in intensity after midnight at midlatitudes. Other temporal
and spatial irregularities found in the airglow -- patchiness
(Ref 118), traveling waves (Ref's 119,120), and meridional
gradients (Ref 125), for example -- may call for three- (or
perhaps two-) dimensional dynamical modeling.

Variations in the hydroxyl intensity have been found
to correlate with the occurrence of sporadic as well as re-
curring events, such as stratospheric warmings (Ref 112) and
severe magnetic storms (Ref 122). The latter (and in all
probability the former) also produce changes in the bands'

117

rotational temperature, which is in effect the kinetic temperature. These episodic, propagating disturbances overlie the more or less regular variations with mean solar ultraviolet irradiance (which determines the altitude profiles of H and O_3) and the more localized atmospheric wave-induced and mesosphere-temperature effects.

The vast majority of existing data refer to the nightglow. Some measurements have been made at twilight, but virtually none at solar elevations above $-5°$ because of the overlay of Rayleigh-scattering of sunlight by the atmosphere at the shorter hydroxyl wavelengths (which can be inexpensively measured with uncooled spectroradiometers and are detectable through/against the lower atmosphere, unlike the $\Delta v = 1$ sequence). We have used the fact that the rates of emission from the same upper state to two different lower states are proportional to the Einstein coefficients for the two transitions to assess the mean intensities of the fundamental bands from the measurements of intensities in these higher overtone sequences (Section 3.3).

In the following subsections we discuss the airglow's variation with time of day, season of year, phase of solar cycle, magnetic disturbance index, and stratospheric warmings. Irregularities at a shorter spatial-temporal scale caused by atmospheric wave phenomena are discussed separately in Section 3.5. (While all but one of these column intensity variations depend on latitude the latitude dependence of the background noise spectrums is not known.) We then develop a model of the variation of the atmosphere's projected radiant intensity as a function of these recurring and episodic geophysical parameters, which assumes that their effects act independently (and linearly). This occurrence model assigns multipliers to the mean radiance with standard deviations that estimate the uncertainty due to the non-deterministic nature of the variability and the limi-

tations of existing input data. The estimated amplitudes of infrared clutter are taken as proportional to the radiance within the selected spectral band at the projection of the sensor's field of view (Section 3.5).

The body of column-intensity data from ground stations allows the large-scale (~degrees of latitude) hydroxyl surface radiances to be derived. As virtually no systematic data exist on the smaller-scale spatial and temporal inhomogeneities, however, the clutter model is much less reliable than the average-intensity model. In what follows negative fractional uncertainties (-u), which can be comparable to 1 and thus would otherwise result in too-low (or even negative) radiance limits, should be applied as $(1 + u)^{-1}$; for example a calculated total uncertainty ±70% means that the 1σ range (due to unsystematic natural behavior and/or inadequate input information) would be between 1.7 and 0.59 times the quoted best-estimate spectral radiance.

3.2.1. Diurnal Variations

Many groups (Ref's 115,122,123,124,125,126, among others) have searched for systematically recurring patterns in the hydroxyl nightglow, underlying (and perhaps connected with) the fluctuations due to atmosphere dynamics. Detailed analyses (Ref's 115,124) show that the occurrence frequency of types of time-dependence depends on latitude and give an indication that the distribution of these patterns changes with season. At low latitudes a steady decrease through the night is most commonly observed, in general agreement with staticphotochemistry calculations. The most common diurnal variation at midlatitude (where the most measurements have been made) is a decrease after evening twilight to a minimum near midnight, followed by an increase. Recurrence of nightglow patterns gradually becomes undetectable at higher latitudes

(>~55°). This overall change with latitude in the diurnal
variation shows the increasing importance of species transport
at higher latitudes. We found the average ratio of highest
to lowest intensity over the course of a night to be 1.64
± 0.27, with no latitude dependence apparent within the
noise of the data set.

The most striking feature of the hydroxyl glow
near twilight is a narrow factor-about-two minimum at 4-6° solar
depression angle (Ref's 126,127,128,129). This behavior occurs
about 3/4 of the evenings (Ref 126), and also ~1/4 of the
morning twilights. A measurement of the column intensity during
the day found the mean to be about the same as nightglow (Ref
129); on the other hand some calculations (Ref's 109,111)
suggest a daytime decrease by a factor as much as three.

We postpone specifying a diurnal variation model
until we have discussed the other solar zenith angle-related
changes; refer to Section 3.2.7.

3.2.2. Seasonal Variations

The distribution of time-dependence patterns
(Ref's 115,124) and the time of the nightly minimum (Ref 127)
have been reported to vary repeatably with season in the
northern hemisphere. From this variation data we have derived
a best-estimate seasonal multiplier and uncertainty:

$m_S = 1 + 0.26 \sin [(\pi/3)(M - 5/2 + 2\phi/45)] \sin \pi(\phi/90 - 5/18)$,

$u_S = \pm 23\%$.

Here M is the month of the year (M = 1 refers to January) and
ϕ is the latitude in degrees (positive in both hemispheres);
the argument of each sine function is in radians. Note that the
intensity modulation is not in phase with the mean solar eleva-
tion, but may be controlled by the mesospheric temperature (which
is a maximum in winter).

120

The average over a night of the spectral radiance at month M and latitude ϕ is found by multiplying the mean radiance in Fig 24 or Table 6 by this factor. At $\phi = 25°$ the amplitude of the seasonal modulation goes to zero, and at 70° it is a maximum of 0.26. In our model this variation is symmetric about the equator with a six-month phase difference between hemispheres. The 1σ uncertainty u_S (= 23%), which is in part due to the seasonal change in occurrence of diurnal patterns, is an average of the uncertainties in the data sets (references above).

Stratospheric warmings, an episodic winter-seasonal phenomenon, are discussed separately in Section 3.2.5.

3.2.3. Solar Cycle Variation

A change in the annual-mean hydroxyl radiance (corrected for the seasonal and diurnal variations, and again with dynamics-induced fluctuations smoothed out) has been found to be correlated with phase of the solar cycle at latitudes 44°N (Ref 115) and 58°N and 42°N (Ref 122). Its amplitude averages 17%, and noise in the data set introduces an uncertainty $u_C = 23\%$. The radiance multipler for the eleven-year solar cycle is thus

$$m_C = 1 + 0.17 \cos \left[(2\pi/11) (Y - 1958) \right] \pm 23\%,$$

where Y is the year and the argument of the cosine is as usual in radians.

This smooth variation in phase with the solar cycle is most probably due to the increase/decrease in average hardultraviolet energy emitted by the sun. (Solar flux variations at shorter time scales would also be expected to induce fluctuations in the OH radiance, averaged over many days; we have identified no direct evidence of such effects.) The above dependence is derived from a geographically very limited

121

range of observations; nonetheless as the maximum hydroxyl
emission coincides with the maximum solar flare activity,
whose effect is felt worldwide, the dependence in first approx-
imation should be applicable to all latitudes. The uncertainty
quoted is again an unweighted average of the uncertainties in
the individual nightglow surveys.

3.2.4. Magnetic Storm-Induced Variations

Geomagnetic storms with global magnetic index Kp
greater than about 4 have been found to produce wavelike changes
in the hydroxyl intensity (Ref 122). (The rotational tempera-
tures are also affected.) The delay of the initial enhancement
increases with decreasing latitude, while the amplitude of the
disturbance decreases. This first pulse is followed by oscill-
ations with smaller amplitudes, which extend below as well as
above the mean. Both the enhancement and its period increase
with Kp. This behavior suggests that the onset of a major
magnetic disturbance excites a wave in the mesosphere that
spreads from high latitudes (at an observed speed of 5 - 10
m/s along the meridian), decaying in amplitude. The failure
of some other surveys to detect this correlation (Ref's 124,
129) may be due to weakness of the disturbances during their
measurements, or perhaps lack of samplings when the waves
is peaking.

The maximum increase in zenith intensity resulting
from major magnetic storms is 14% per unit Kp above 4, and the
decay rate is 20% per day. An analysis of the network data in
Ref 122 indicates that the radiance multiplier at time t_K in
days from the beginning of the disturbance can be expressed as

$$m_K = 1 + G(t_K, \phi, Kp - 4) \pm u_K,$$

where the change due to the event is

122

$$G = g \cos \beta \exp(-0.2t_K),$$
$$g = 0.14 \ (Kp - 4) \ (a\phi^2 + b\phi + c), \quad \text{and}$$
$$\beta = 5 \ (t_K - 0.26 \ \Delta\phi)/(Kp + 21).$$

The empirical constants are

$$a = 8.6 \times 10^{-4}, \ - \ b = 4.0 \times 10^{-2}, \quad \text{and} \ c = 4 \times 10^{-1};$$
$$u_K = \pm \ 1.5G/m_K \times 100\%.$$

This prescription holds when $4 < Kp < 9$, $\phi < 65°$. For
$\phi > 65°$ only an additional estimated uncertainty

$$u_K(\phi > 65°) = \pm 1.5 \ [0.14 \ (Kp - 4)] \ \exp -(0.2t_K) \times 100\%$$

can be applied to the radiance, as no useful data are available
on the effect of geomagnetic storms on airglow within the auroral
oval and polar cap. $\Delta\phi$ in the cyclic term is the difference
in latitude from the point of observation to the "origin" of
the disturbance, which we estimate to be at 65°.

Because this origin cannot be unambiguously
determined and as no systematic data on the effect exist other
than from this one survey (Ref 122), substantial error may
result from application of the above formulas. For example,
an error in phase of the wave could even reverse the sign of
the change in hydroxyl intensity. Hence we have assigned a
large uncertainty to the enhancements excited by geomagnetic
storms.

3.2.5. Stratospheric Warming-Induced Enhancement

Similarly, the long-term effects of stratospheric
warmings (Ref 130) on the high latitude hydroxyl emission are
not well characterized. Major warmings, of scale sufficient
to cause measurable changes in the intensity (and temperature),
are thought to occur an average of once every two winters (Ref
131). They represent a meteorological effect on the mesosphere,
in contrast to geomagnetic storms, in which energy from the
thermosphere is coupled downward to the altitudes where hydroxyl
is excited.

An extensive survey of OH radiance during an identified stratospheric warming was made from the OGO-4 satellite in 1967-68 (Ref 112). Emission in the (9,3) band near 0.6225 μm was found to vary with longitude (it increased markedly above 60°N from 70°E to 70°W, for example). Increases of up to a factor four in the nadir column intensity were reported, with a factor two typical for about a month during the late stages of the warming when the temperature wave reaches the mesosphere. (Recall that the $H + O_3$ reaction rate increases with temperature.) These sole satellite data are supported by one set of ground measurements from a station at 58° latitude (Ref 132), from which a southward-propagating enhancement wave with velocity 1-2 m/sec was inferred.

This thin data base does not allow prediction of the changes in local hydroxyl radiances. The most that can now be done is assignment of an additional uncertainty u_W. We estimate u_W to be ± 50% at latitudes above 55° and ± 30% between 45° and 55° during major winter stratospheric warmings.

3.2.6. Latitude Effects

As we have seen, latitude comes into play in each of these OH variations except solar-cycle. The changes of intensity with latitude that would be due to the change in solar ultraviolet fluence are contained in the diurnal variation to be described below; no others can be resolved from the data set. Latitude, then, appears as a dependent variable in the other intensity modulations rather than as a fully independent variable.

3.2.7. Diurnal Model

We fit the survey data on diurnal variation of the nightglow with equations that describe a linear decrease after evening twilight at equatorial latitudes giving way to a

124

midnight minimum at midlatitudes, which becomes shallower toward higher latitudes and eventually disappears into the noise. These are the most probable patterns in each latitude region; the less-frequent occurrence of other types of diurnal variation is accounted for in the calculated uncertainties. The time of day H is in hours local solar time, or Universal Time H +/- 1 hr per 15° E/W longitude (for example at 1030 U.T. the local solar time at 35° E is 12.83). t_e and t_m are the local solar times of evening and morning "hydroxyl twilight", that is, when the local solar depression is 5° (where the minimums in the airglow are observed). The diurnal variation multipliers for the night-glow and their uncertainties u_D are

$$0° < \phi < 26° \quad m_D = 1 - 0.04(24-H) \pm 33\%, \quad 24 > H > t_e;$$
$$m_D = 1 - 0.04H \quad \pm 29\%, \quad t_m > H > 0.$$
$$26° < \phi < 40° \quad m_D = 0.88 + 0.0061(H-24)^2 \pm 10\%, \quad 24 > H > t_e;$$
$$m_D = 0.88 + 0.0061 H^2 \pm 10\%, \quad t_m > H > 0.$$
$$40° < \phi < 56° \quad m_D = 0.94 + 0.0033(H-24)^2 \pm 25\%, \quad 24 > H > t_e;$$
$$m_D = 0.94 + 0.0033 H^2 \pm 25\%, \quad t_m > H > 0;$$
$$56° < \phi < 90° \quad m_D = 1 \pm 63\% \quad \text{Between OH twilights.}$$

For the twilight and dayglow, a best-estimate applicable to all latitudes is

$$m_D = 0.44 + 0.56 \cos[(\pi/12)(H-12)] \pm 100\%, \quad t_e > H > t_m.$$

Attention is directed to the large uncertainty assigned. This fitting function indicates a season-dependent minimum intensity at each twilight transition, since the times at which hydroxyl-twilight occurs vary with month of the year, and an increase toward noon up to the mean nighttime radiance.

The local times of these twilight transitions are determined as follows. First, the local hour angle of the sun H_s is found from the equation

$$\cos H_s = \sin(Dep)[\cos\phi \cos(Dec)]^{-1} - \tan\phi \tan(Dec),$$

where (Dec) and (Dep) are the solar declination and depression angles. At hydroxyl twilight $\sin(Dep) = \sin 5° = 0.087$. (Dec)

at zonal meridians is tabulated against date in Ref 133, as is
the time of solar meridian passage t_s. The local mean times
of the two twilights are:

$$t_m = t_s - H_s, \quad t_e = t_s + H_s,$$

where H_s (like H) is expressed in hours. This procedure for
finding the local times of hydroxyl twilight, which are needed
to decide whether to apply the nightglow or twilight-dayglow
formula, will be illustrated by a worked example in Section
3.4.1.

3.3. Emission Spectrum

Spectral intensities of the hydroxyl airglow measured
in $\Delta v > 1$ bands -- that is, at visible and near-infrared wave-
lengths -- permit the essentially-unmeasured spectrum of the
$\Delta v = 1$ sequence to be derived from ratios of intensity in
progressions (bands originating from the same upper state).
The volume rate of radiation I_{ij} from state i to state j
is $A_{ij} n_i$, where A_{ij} is the Einstein coefficient for the
transition (the inverse lifetime) and n_i is the number density of
molecules in state i. Thus the rate to lower state k is simply

$$I_{ik} = I_{ij} \times A_{ik}/A_{ij}.$$

As we noted at the start of Section 3, our occurrence model
assumes that the relative spectral distribution of OH radiation
remains constant over space and time. Consequently only the
mean radiances in single transitions originating from the
second to the ninth upper states and ratios of Einstein coef-
ficients need be known to determine the mean airglow intensity
in each fundamental vibrational band (except the (1,0), which
is determined from the population model in Ref 109).

Unfortunately, no fully coherent and reliable set of
these intensities exists. Hence we have derived a least-error
set by fitting the existing nightglow spectrum data with
measured and theoretically-derived Einstein coefficients. It
was found that the laboratory A_{ij}'s (Ref 134) resulted in

maximimum self-consistency of individual progression intensities
in the radiometry data base (Ref's 106,108,109,110,115,116,
117,120,125,132,135-138).

To compare the measurements from different instru-
ments and geophysical conditions, we first corrected them to
the zenith. No attempt was made to compensate for variable
attenuation by the lower atmosphere, as this effect introduces
only a small error at the long wavelengths of most of the
measurements (out-scattering is in any case largely compensated
by in-scattering from the wide-angle airglow source). We then
factored out the seasonal and solar cycle variations using the
procedure described in Sections 3.2.2 and 3.2.3. These correc-
tions reduced the average uncertainty in the combined data to
28% from its initial 70%. (The latter figure is substantially
larger than the claimed uncertainty of individual measurements.)
We interpret this factor- 2-1/2 reduction in the spread of ab-
solute intensities of the OH Meinel bands as evidence of the
validity of our method for removing the recurring variations
and of the accuracy of the set of Einstein coefficients adopted.

The resulting zenith intensities in the fundamental
sequence, along with the 1σ uncertainty in reproducibility
of the data and the intensities calculated in Ref 99's review
of near-infrared airglow, are listed in Table 6. This distri-
bution represents a mean over the solar cycle, season, and time
of night. Fig 24's spectrum was generated with the AIRSPEC
code (Ref 50) using the Einstein coefficients in Ref 139 and
standard rotational line intensity functions (Ref 140) at a
rotational temperature of 213K, which is typical of the winter
mesosphere (Ref 141). The total spectral width of each vibra-
tional band changes by only a small amount over the range of
temperatures encountered in the mesosphere; therefore, con-
sidering also the overlap of adjoining bands and the errors
in band intensities, we have judged a single spectrum to be

127
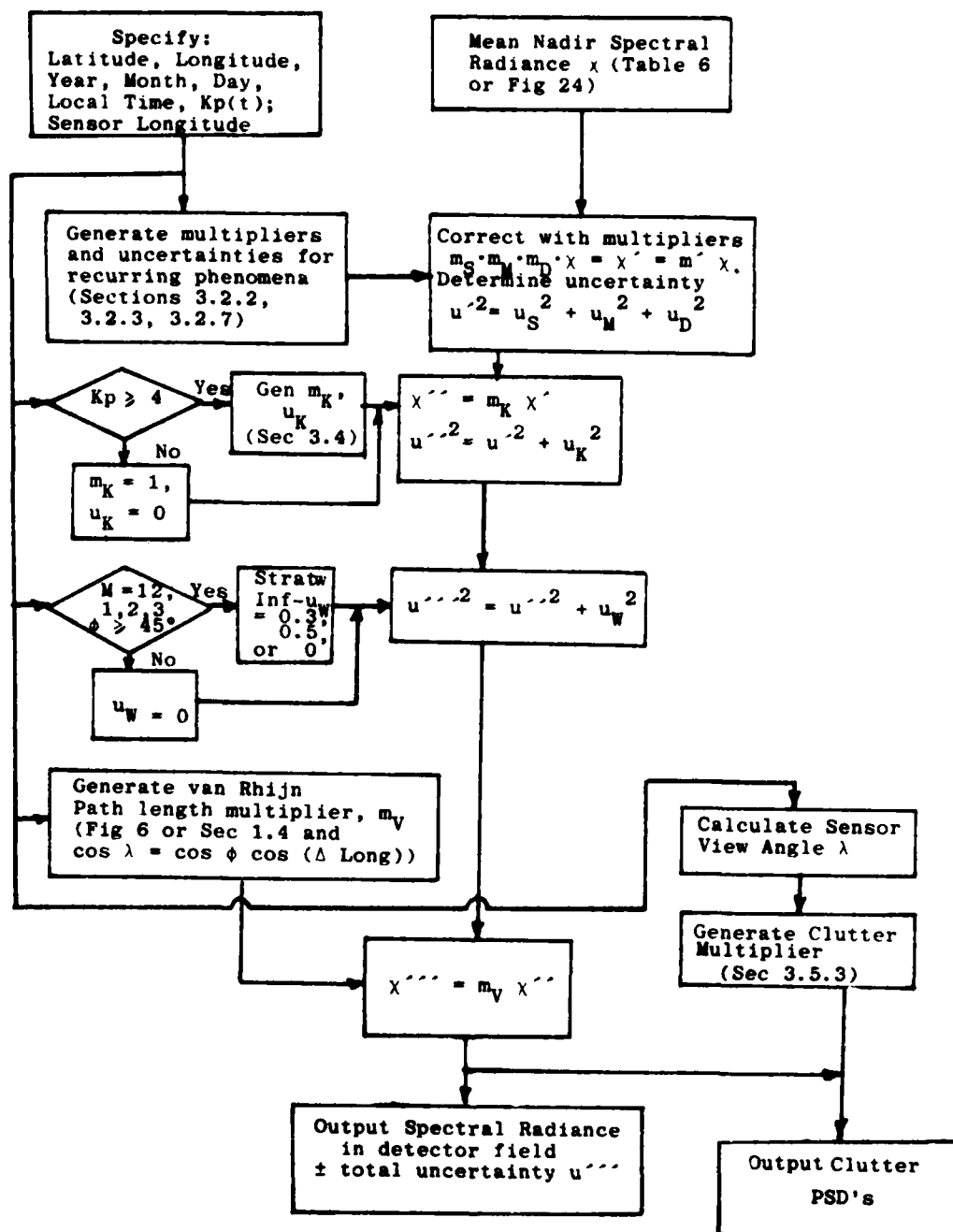
Figure 25. Flow diagram for a first-generation model of hydroxyl airglow background clutter.

adequate for the occurrence model. (Spectrums for other
temperatures can of course be readily calculated from Table 6.)
Line intensities in Fig 24 are averaged over a 10 cm^{-1} rectan-
gular spectrum interval.

3.4. Calculations of Column Intensity

The long-period (hours to solar cycle) temporal and
global distributions of radiance in individual bands or spectrum
intervals are calculated from the means in Table 6 or Fig 24
using the procedures described in Section 3.2. The analytic
functions that model the variations are piece-wise continuous
with latitude; discontinuities where the functions change
should be recognized as due to this quantization noise rather
than taken as a real geophysical effect, and the values faired
into one another. Similarly, the changes in intensity with year
and season, for which integer values of Y and M were derived from
the data base for input to the formulas, should be taken as
continuous.

Since the geophysical processes underlying the column
intensity changes are considered as independent of one another,
the m's can be multiplied together in any order and the total
fractional uncertainty is the square root of the sum of the
squares of the individual u's. Information on whether a major
stratospheric warming or magnetic storm is in progress, which
is available from USAF Air Weather Center as well as non-DoD
sources, is input to assess the episodic effects. Little
further error is introduced into the occurrence pattern if the
change in zenith radiance over oblique sight paths through the
emitting layer is neglected; we prescribe using the radiance
at the mid-point of the cut. Similarly, as the difference
between latitude ϕ at the ground intercept and ϕ' at the
emitting layer (shown in Fig 6) is substantial only above ~55°
where the uncertainty in the airglow intensities is already
large, it can also be neglected.

129

Figure 25 is a flow chart of the procedure for calculating expectation hydroxyl background intensities and their uncertainties. χ is the mean radiance of the airglow within the selected wavenumber (or wavelength) interval, and the other symbols not defined in the text are self-explanatory. As shown, the multipliers for the recurring-geophysical variations and their uncertainties are generated to derive a provisional $\chi' \pm u'$, and then the magnetic storm and stratospheric warming factors (when applicable) give the zenith radiance $\chi'' \pm u'''$. The van Rhijn path length factor is determined from the latitude and longitude of the specified sensor intercept using Fig 6 or the equations in Section 1.4.2.1. The estimated upper and lower limits are the expectation radiance multiplied and divided by $(1 + u''')$.

The expected amplitude and frequency range of clutter noise superposed on this calculated average local radiance is then derived from the simple model in Section 3.5.

3.4.1. Example Calculation

To illustrate this procedure, we work an example for near-twilight, magnetically-disturbed conditions:

Latitude ϕ = 55°N

Longitude   = 70°W, sensor at 20° W.

Day/month M/year Y = 01/09/1984

Time UT   = 2300 U.T.

Kp   = 7 storm onset 2.0 days earlier.

Seasonal:
(Sec 3.2.2)

$$m_S = 1 + 0.26 \sin \pi/3 \ (9.0 - 5/2 + 110/45) \ \times \ \sin \pi \ (55/90 - 5/18)$$
$$= 1.013 \pm 23\%.$$

Solar cycle:
(Sec 3.2.3)

$$m_C = 1 + 0.17 \cos (2\pi/11) \ (1984 - 1958)$$
$$= 0.89 \pm 23\% \ .$$

<u>Diurnal:</u> (Sec 3.2.7)	Local solar time H is universal time UT corrected for the longitude difference $-70°/(15°/hr) = -4.67$ hr, or $23.00 - 4.67 = 18.33$. We next calculate time of hydroxyl evening twilight to determine whether to apply the nightglow or dayglow variation formula. Referring to Table 1 of Ref 133, we find that at 70°W on 01 Sep local solar time of solar meridian passage t_s is 11.67 hours and solar declination is 8.4°. The hour angle of the sun is then determined from

$$\cos H_s = 0.087 \, (\cos 55° \cos 8.4°)^{-1}$$
$$-\tan 55° \tan 8.4° = -0.0563,$$
$$H_s = 93.7° \times 1 \text{ hr}/15° = 6.21 \text{ hr}.$$

Then $t_e = t_s + H_s = 11.67 + 6.21 = 17.88$. As $H > t_e$, we apply the nighttime dependence for 55° latitude:

$$m_D = 0.94 + 0.0033 \, (18.33 - 24)^2 \pm 25\%$$
$$= 1.05 \pm 25\%$$

<u>Recurring:</u>

$$m' = m_S \cdot m_C \cdot m_D = 0.95$$
$$u' = (0.23^2 + 0.23^2 + 0.25^2)^{1/2} = \pm 41\%.$$

<u>Magnetic Storm:</u>
(Sec 3.2.4)

$$m_K = 1 + 0.14 \, (7 - 4) \, [8.6 \times 10^{-4} \, (55)^2$$
$$- 0.040 \, (55) + 0.4] \times$$
$$\cos 5[(2 - 0.26(65 - 55))/28] \exp(-0.4)$$
$$= 1.11$$
$$u_K = (1.5) \, (0.11)/1.11 = \pm 13\%.$$

<u>Stratwarm:</u>
(Sec 3.2.5)

$M \neq 12, 1, 2,$ or 3; therefore no change.

<u>Total</u>
<u>Zenith:</u>

$$m'' = m' \cdot m_K = 1.05$$
$$u'' = (0.41^2 + 0.13^2 + 0^2)^{1/2} = \pm 43\%$$

131

Pathlength: Referring to Section 1.4.2.1, the angle λ
                between the exoatmospheric measurement platform
                nadir and the point of observation is found
                from

$$\cos \lambda = \cos \phi \cos (\Delta \text{ longitude})$$
$$= \cos 55° \cos (70°-20°) = 0.3687,$$
$$\lambda = 68.37°.$$

The elevation angle of the sight path is found from

$$\sin \theta = \sin \lambda/(P/R - \cos \lambda)$$
$$= 0.9300/(6.6321 - 0.3687) = 0.1485,$$
$$\theta = 8.54°.$$

As this angle intercepts the earth's surface
(see Fig 6), the path length for $\rho_2 = 87$ km $+$ R,
$\rho_1 = 80$ km $+$ R is given by the first of the
formulas in Sec 1.4.2.1. Substituting ρ_2,
ρ_1, P $= 6.6321$ R, R $= 6370$ km, and $\sin^2\theta$,
we find the pathlength is 30 km.
Therefore $m_V = 30/7 = 4.3$.

Radiance $m''' = m'' \cdot m_V = (1.05)(4.3) = 4.52 \pm 43\%.$
Multiplier:

Thus the projected sky radiance in, for example, the total
(13 w/km^2 ster) hydroxyl band system would be $\chi''' =$
59 + 25, − 18 w/km^2 ster.

3.5. Clutter Statistics

Irregular, non-systematic variations also appear in
the hydroxyl nightlow. These have at least two loosely-defined
spatial-temporal scales, ~5 min-25 km horizontally and ~3 hr-
thousands km. The latter modulations, whose occurrence statis-
tics is poorly understood (largely because their scale is close

have amplitudes of about 10% and are considered to be associated with traveling ionosphere disturbances (Ref 142). The shorter-wavelength irregularities are thought to be due to internal gravity waves (Ref 143,144) that have their origin in disturbances of either the troposphere (principally) or thermosphere. As their scale is much closer to that of the footprints and signal integration times of typical measurements sensors, they would be the major source of clutter from hydroxyl.

3.5.1. Zenith Data

No quantitative data exist on the frequency spectrum of this background in near-limb projections. The measurements from below the layer have focused principally on temporal variations, with some preliminary spatial cross-correlations determined using a multiple-field $\Delta v = 4$-bands photometer (Ref 145). Spatial scans of $\Delta v = 1$ and 2 emission made with AFGL's optical aircraft flying at 220 m/sec (Ref 31) and with a radiometer whose field of view was rotated in a vertical plane at 2° elevation/sec (Ref 146) (a horizontal sweep speed of 3 km/sec at the zenith) do not differ qualitatively from the many temporal scans made with fixed-pointing instruments. (These hydroxyl data bases are available for quantifying the short-period spatial variations.)

Narrow-field groundbased instruments -- with footprint <5 km on the hydroxyl layer -- show the variation to have amplitude 2-3% in a band of frequencies near $1/5$ min^{-1} (Ref's 142, 143, 145, for example). No power spectral densities have been reported in the journal literature, presumably because this fluctuation signal is so weak. Reports of large episodic changes -- "spikes" or "ledges" of scale less than a few min and amplitude greater than a few percent, not due to cloud or instrument effects -- are conspicuously missing from the literature.
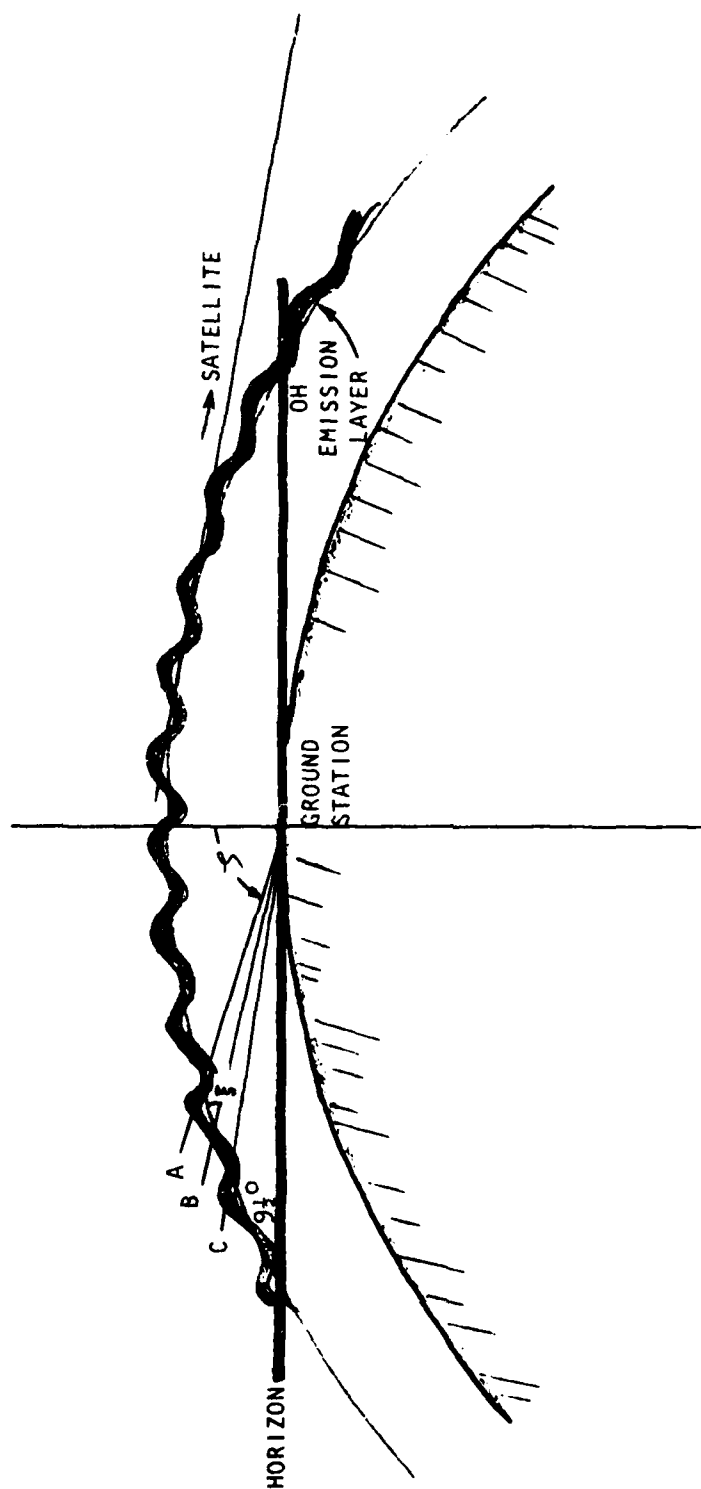
Figure 26. Model of the geometry of the hydroxyl radiance variations (adapted from Ref 150). The wave heights are exaggerated to illustrate the effect of changing sight path at low ξ.

134

How the rms amplitude or the frequency range of this irregularity depends on average airglow radiance, latitude, or other geophysical parameters, is not known. One model (Ref 149) suggests that at least one type of short-period irregularity is excited when longer-period atmospheric waves reach a threshold amplitude. While the disturbances might be expected to be more intense and frequent at high latitudes (Ref's 3,148), especially in the winter mesosphere (Ref 142), the direct evidence is not useful for modeling such behavior. We have not attempted to extract this information from the nightglow data base, as instrument noise and data smoothing (seldom specified) would most probably mask any systematic changes.

3.5.2. Low Elevation-Angle Data

Spatial distributions of OH radiance near the horizon can be measured by conventional photography from mountain or aircraft altitudes (Ref 107). The van Rhijn gain raises the irradiance in the image plane over the effective-exposure threshold of near infrared-sensitive emulsions (Ref 142), and simultaneously an enhancement of the projected irregularity results in readily-detectable contrast on the negative (rather than a smooth and thus virtually uninterpretable density distribution). At zenith angles greater than about 70° -- an angle ξ of 22° between line of sight and hydroxyl layer -- the amplitude of the spatial variations in the $\Delta v = 4$ and 5 bands within the camera's spectral range increases to about 15% in many of the photographs (Ref 150). The low-to-the-horizon nightglow shows as a series of more or less regularly rippled clouds separated by a few 10's of km and traveling perpendicular to their length in a horizontal plane, and sometimes as patches whose spatial frequency spectrum would be isotropic. No favored direction of the

waves has been identified. Occurrence of this structure is reported by one group to be correlated with lunar high tide (Ref 148), which they interpret as due to excitation of secondary shorter waves in the mesosphere by a harmonic of the lunar atmospheric tidal wave. The literature does not provide quantitative information on the probabilities of occurrence of amplitude of this radiance modulation.

Other investigators (Ref 150, 151) explain the measured sky brightness distributions by invoking a "corrugated" emitting layer whose vertical amplitude/horizontal wavelength ratio is ~1/20, such as is shown in Figure 26. Near the zenith, the line of sight intercepts the layer once; variations in radiance are due to the small changes in pathlength as its angle to the layer changes. Near the horizon (sight paths A,B,C), the modulation of the pathlength gain factor would increase rapidly, with multiple intercepts on the waves at low incidence angles. (Near-horizon views also enhance the relative sight path through the bottom edge of the emitting volume, where most of the irregularity is expected (Ref 148)). This height variation implies that the maximum van Rhijn factor for hydroxyl (in Section 1.4) is somewhat overestimated.

This airglow geometry indicates that the peaks should appear closer together as ξ decreases. That this foreshortening toward smaller spatial-scale irregularities has not been reported for ξ between 22° and 9-1/2° (0° elevation, about the limit of view on the photographic images) is most probably due to the nonuniformity of the wavelength. From the near-zenith temporal (and spatial) variations and gravity wave theory, it may be concluded that a broad band of spatial frequencies is present in the emitting layer, which would have the effect of attenuating higher-frequency structure at low incidence angles (such as those of limb views from rockets or satellites).

3.5.3. Clutter Amplitude and Frequency

This incidence angle ξ is the key variable in modeling the short-period, short-wavelength hydroxyl radiance variation seen from space. From geosynchronous orbit ξ reaches 22° at an elevation angle θ of 8.14° (refer to Fig 6); therefore the ground-intercept latitude in the nadir meridian (or the spherical angle λ from the earth's center) is 59.8°. The groundbased hydroxyl-radiometry data indicate that when $\theta < 8.14°$, where the points on the earth's surface are at $\lambda < 59.8°$ and the van Rhijn gain is thus $< 2\text{-}1/2$, the rms amplitude of this clutter is

0.02 x average radiance $\chi^{\prime\prime\prime}$, with 70% probability

0.03 x average radiance,   with 30% probability.

For the range $22° > \xi > 9.3°$,

which corresponds to $8.14° < \theta < 8.68°$ and

$59.8° < \lambda < 81.32°$,

we take the fluctuation amplitude to be larger and again proportional to the average radiance. We deduce from the available data that weak disturbances resulting from the layer having the shape indicated in Fig 26 are always present, and are overlaid roughly half the time by a strong disturbance (perhaps resulting from the nonlinear lunar-tide process described in Ref 148) with the microdensitometrically-measured amplitude reported in Ref 150. Some probability of even larger excursions is included to err on the side of conservatism. The estimated fluctuation amplitudes are then

0.07 x average radiance, with 50% probability

0.15 x average radiance, with 40% probability

0.20 x average radiance, with 10% probability.

These occurrence probabilities are to be taken as independent of the direction in the horizontal plane in which the measurements sensor is pointing, latitude, mean radiance, and solar time. (A variation with time of lunar transit would be included

137

when the data of Ref 148 are refined.) Note that when λ = 81.32° the sensor's sight path is tangent to the earth's surface, which is the effective limit of the photographic measurements of hydroxyl emission structure.

For the range of θ over which the geo-synchronous sensor's field of view intercepts the hydroxyl layer but not the earth, which is

$$8.68° < \theta < 8.82° ,$$

which corresponds to $\quad 9.3° > \xi > 0° ,$

no structure data from the bottomside are available. Ref 150's geometric model does not show 9.3° to have any special property, and the presence of a distribution spectrum of wavelengths indicates no change in the spectrum of radiance variations at these low incidence angles. Hence we prescribe continuing the probability distribution of clutter amplitudes for ξ = 22° to 9.3° down to ξ = 0°.

These background radiance variations extend over spatial frequencies $1/50$ km^{-1} to $1/10$ km^{-1} in the photographic data. The qualitative similarity between temporal and spatial scans of the radiation, supported by the theory of these fluctuations (Ref's 143, 152), suggests that the same frequencies are present when ξ >22°. The best-estimate of the spatial power spectral density of hydroxyl noise seen by a geo-synchronous experiment sensor is thus

$(0.03$ or 0.02 radiance$)^2$

    per cycle/km, $\qquad\qquad\qquad \theta < 8.14°, \lambda < 59.8°$

$(0.20, 0.15$ or 0.07 radiance$)^2$

    per cycle/km, $\qquad\qquad\qquad \theta > 8.14°, \lambda > 59.8°.$

The same prescription applies to the temporal PSD's in the frequency band between $1/600$ and $1/100$ Hertz. No reliable estimate can be made of probabilities of exceedance of spectral

power beyond those derivable from the estimated occurrence probabilities.

At the current state of knowledge, these estimates of the clutter background can be taken as applicable to all projected hydroxyl radiances under all geophysical conditions.

3.6. Hydroxyl Data Base

It is clear that the existing information on hydroxyl-emission irregularities, in particular those in limb views of the layer, is sufficient to construct only a rudimentary model of the infrared clutter background. The spatial and temporal noise spectrums at incidence angles ξ as low as $6.77°(0 = 8.73°)$ could be determined by measurements from balloon altitudes. The short-wavelength irregularities' frequency spectrum, with its occurrence statistics and dependence on geophysical para-meters, could be derived from ground and aircraft measurements; indeed, some unanalyzed existing data contain this type of information. Surveys of the airglow's radiance structure from satellite and even sounding rockets would of course provide the most directly-applicable inputs to design of future measurements experiments, as is the case for the auroral infrared backgrounds.

This review has also shown broad gaps in the data on other important aspects of the hydroxyl vibrational-bands back-ground. Information is lacking on, for example, the basic radiative and collisional deactivation parameters of $OH^\dagger$; the systematics of airglow intensity averaged over ~1 hr through the day; and in the spectral distribution in the fundamental sequence, particularly in above-the-limb projections.

REFERENCES

1. T.C. Degges and H.J.P. Smith, A High Altitude Infrared Radiance Model, AFGL-TR-77-0271 (30 Nov 77).

2. F.Y. Kneizys, E.P. Shettle, W.O. Gallery, J.H. Chetwynd, Jr., L.W. Abreu, J.E.A. Selby, R.W. Fenn, and R.A. McClatchey, Atmospheric Transmittance/Radiance: Computer Code LOWTRAN 5, AFGL-TR-80-0067 (21 Feb 80).

3. J.E.A. Selby, F.X. Kneizys, J.H. Chetwynd, Jr., and R.A. McClatchey, Atmospheric Transmittance/Radiance: Computer Code LOWTRAN 4, AFGL-TR-78-0253 (1978).

4. C.H. Humphrey, R.M. Nadile, C.R. Philbrick, and D.R. Smith, Atmospheric Infrared Radiance Variability, AFGL-TR-81-0207 (27 May 81).

5. I.L. Kofsky and J.W. Schroeder, Visible and Infrared Radiations from the atmosphere Accompanying PCA Events, AFCRL-TR-74-0476 (30 Sept 74).

6. R.R. O'Neil, A.T. Stair, Jr., E.T.P. Lee, D. Burt, and G. Frodsham, Excede Spectral: An Artificial Auroral Experiment, Paper 81-0422, AIAA 19th Aerospace Sciences Meeting, St. Louis, 1981.

7. K.D. Baker, D.J. Baker, J.C. Ulwick, and A.T. Stair, Jr., Rocketborne Measurement of an Infrared Enhancement Associated with a Bright Auroral Breakup, AFGL-TR-77-0157 (05 Jul 77).

8. S.-I. Akasofu, Polar and Magnetospheric Substorms, Springer, New York, 1968.

9. C.M. Langley and W.G.M. Blaettner, E-O Sensor Signal Recognition: Computer Code SPOT I, Radiation Research Associates (Ft. Worth, TX) Report T7809 (01 Oct 78).

10. W.F. Grieder and L.A. Whalen, Geometric Aspects of Rocket Photometry, AFGL-TR-76-0046 (Feb 76).

11. J.W. Chamberlain, Physics of the Aurora and Airglow, Academic Press, New York, 1961.

12. D.W. Swift, Rev's Geophys. Space Phys. $\underline{17}$, 681 (1979).

13. Y.I. Feldstein and G.V. Starkov, Planet. Space Sci. $\underline{15}$, 209 (1967).

REFERENCES (continued)

14. J.A. Whalen, General Characteristics of the Auroral
     Ionosphere, in Physics of Space Plasmas (ed's T. Chang,
     B. Coppi, and J. Jasperse), SPI Conference and Reprint
     Series 4, Scientific Publications, Cambridge, MA (1981).

15. C.P. Pike and J.A. Whalen, J. Geophys. Res. 79, 985 (1975).

16. A.T.Y. Lui and C.D. Anger, Planet. Space Sci. 21, 799 (1973).

17. G. Davidson, The Use of Digital DMSP Data for Auroral
     Measurements, AFGL-TR-81-0105 (15 Feb 81).

18. J.B. Kumer, R.D. Sears, J.E. Evans, S.E. Harris, and R.M.
     Nadile, Application of Visible Monochromatic Auroral
     Imaging Data for Modeling Infrared Earth-Limb Morphology,
     AFGL-TR-81-0025 (26 Mar 81).

19. A. Omholt, The Optical Aurora, Springer, New York, 1971,
     Chapter 7.

20. G.G. Shepherd and E.V. Pemberton, Radio Sci. 3, 650 (1968).

21. A.P. Krukonis and J.A. Whalen, J. Geophys. Res. 85, 119
     (1980).

22. R.E. Sheehan, R.L. Carovillano, and M.S. Gussenhoven,
     J. Geophys. Res. 87, 3581 (1982).

23. R.A. Hoffman and J.L. Burch, J. Geophys. Res. 78, 2867
     (1973).

24. P.J. Tanskanen, D.A. Hardy, and W.J. Burke, J. Geophys.
     Res. 86, 1379 (1981).

25. D.J. Strickland, Electron Transport, Chemistry, and
     Optical Emissions in the Auroral E-Layer, AFGL-TR-81-0042
     (Jan 81).

26. M.H. Rees and D. Luckey, J. Geophys. Res. 79, 5181 (1974).

27. I.L. Kofsky, Ultraviolet-Optical Remote Sensing of the
     Ionosphere, AFGL-TR-77-0142 (30 Jun 77).

28. R.L. Arnoldy and P.B. Lewis, Jr., J. Geophys. Res. 82,
     5563 (1977).

29. L.A. Frank and K.L. Ackerson, J. Geophys. Res. 76, 3612
     (1971).

REFERENCES (continued)

30. R.K. White, Incoherent Scatter Radar Measurements in the Upper Atmosphere, DNA 3082T (Nov 77).

31. I.L. Kofsky, D.P. Villanucci, and R.B. Sluder, Evaluation of Infrared Simulation Data, DNA 5521F (26 Nov 80).

32. S.B. Mende and R.H. Eather, J. Geophys. Res. 80, 3211 (1975).

33. I.L. Kofsky, J.D. Geller, and C.A. Trowbridge, Sky Background Measurement Program, AFCRL-70-0032 (30 Nov 69).

34. R.H. Eather and S.B. Mende, J. Geophys. Res. 76, 1976 (1971).

35. A. Belon, G. Romick, and M.H. Rees, Planet. Space Sci. 14, 597 (1966).

36. L.G. Jacchia, Smithsonian Astrophysical Report 375, Cambridge, MA (1977).

37. C.S. Deehr, J.D. Winningham, F. Yasuhara, and S.-I. Akasofu, J. Geophys. Res. 81, 5327 (1976).

38. T.L. Stephens (Kaman TEMPO), Private communication (1982).

39. D.H. Archer, Infrared Program Support, Final Report on DNA-001-81-0011, DNA-0000 (30 Nov 81).

40. D.J. Baker, G.D. Frodsham, J. Kumer, A.T. Stair, Jr., and J.C. Ulwick, Trans. Am. Geophys. Un. 60, 328 (1979).

41. I.L. Kofsky, D.P. Villanucci, and W.S. Andrus, Assessment of Rocketborne and Airborne Infrared Data, DNA 4731F (30 Nov 78).

42. I.L. Kofsky, D.P. Villanucci, and G. Davidson, Assessment and Evaluation of Simulation Data, DNA 4303F (15 Nov 77).

43. D.H. Archer, Requirements for Improved Infrared Prediction Capability, DNA 4585F (30 Apr 78).

44. G.E. Caledonia and J.P. Kennealy, NO Infrared Radiation in the Upper Atmosphere, submitted to Planetary and Space Science (1982).

45. W.P. Reidy, T.C. Degges, A.G. Hurd, A.T. Stair, Jr., and J.C. Ulwick, J. Geophys. Res. 87, 3591 (1982).

46. W.T. Rawlins, G.E. Caledonia, J.J. Gibson, and A.T. Stair, Jr., J. Geophys. Res. 86, 1313 (1981).

REFERENCES (continued)

47. J.P. Kennealy, F.P. Del Greco, G.E. Caledonia, and B.D. Green, J. Chem. Phys. 69, 1574 (1978).

48. F.P. Billingsley II, J. Molec. Spectrosc. 61, 53 (1976).

49. I.L. Kofsky, D.P. Villanucci, and R.B. Sluder, Data Reduction and Auroral Characterizations for ICECAP III, DNA 4220F (31 Jan 77).

50. I.L. Kofsky, C.A. Trowbridge, and R.B. Sluder, Data Reduction and Auroral Characterizations for ICECAP II, DNA 3789F (25 Oct 75).

51. I.L. Kofsky, D.P. Villanucci, M.T. Chamberlain, and C.A. Trowbridge, Further Evaluations of Infrared Simulation Data, DNA-TR-81-41 (30 Nov 81).

52. D.H. Archer (Mission Research Corp.), Private communication (Mar 82).

53. J.P. Heppner and M.L. Miller, J. Geophys. Res. 87, 1633 (1982).

54. R.E. Good and C.A. Trowbridge (AFGL), Private communication (1982).

55. G.D. Nastrom, B.B. Balsley, and D.A. Carter, Geophys. Res. Lett. 9, 139 (1982).

56. R.G. Roble, R.E. Dickinson, and E.C. Ridley, J. Geophys. Res. 87, 1599 (1982),

57. G.V. Groves, J. Brit. Interplan. Soc. 22, 285 (1969).

58. U.S. Standard Atmosphere, NOAA-S/T 76-1562 (1976).

59. J.-C. Gerard and C.A. Barth, J. Geophys. Res. 82, 1674 (1977).

60. J.B. Kumer, Analysis of 4.3μm ICECAP Data, AFCRL-TR-74-0334 (Jul 74).

61. J.B. Kumer and T.C. James, J. Geophys. Res. 79, 638 (1974).

62. J.B. Kumer, J. Geophys. Res. 82, 2203 (1977).

63. J.B. Kumer, Multidimensional Time Dependent Structure and Mechanisms for Non-LTE CO_2 Infrared Emissions and 4.3μm Aurora, AFGL-TR-79-0224 (31 Aug 79).

64. D. Garvin and R.F. Hampson, Chemical Kinetics Data Survey Vol 7, National Bureau of Standards TR1974-30 (1974).

65. H. Trinks and K.H. Fricke, J. Geophys. Res. 83, 3883 (1978).

66. D. Offermann and K.U. Grossmann, J. Geophys. Res. 78, 8296 (1973).

67. D.J. Baker, G.D. Frodsham, J. Kumer, A.T. Stair, Jr., and J.C. Ulwick, in Proceedings of the Second DNA Infrared Data Review Meeting (ed's A.T. Stair, Jr., and J.A. Mayo), AFGL-TM-18 (1979).

68. E.T.P. Lee, R.R. O'Neil, and A.T. Stair Jr., in EXCEDE Spectral Preliminary Results (ed. R.O.'Neil), AFGL-TM-41 (1980).

69. F. Bien, Measurements of Nitric Oxide Vibrational Absorption Coefficient and Vibrational Transfer to N_2, AFGL-TR-77-0181 (Sep 77).

70. R.H. Eather, Rev's Geophys. Space Phys. 11, 155 (1973).

71. A.T.Y. Lui, C.D. Anger, D. Venketesan, W. Sawchuk, and S.-I. Akasofu, J. Geophys. Res. 80, 1795(1975).

72. R.E. Sheehan, M.S. Gussenhoven, and R.L. Carovillano, Activity Rating Scheme and Latitudinal Extent of DMSP Auroras, Boston College Report BC-76 801 (1976).

73. G. Gustafsson, Latitude and Local Time Dependence of Precipitated Low Energy Electrons at High Latitudes, NASA X-645-72-293 (Aug 72).

74. G. Rostoker, Rev's Geophys. Space Phys. 10, 935 (1972).

75. S.L. Valley (ed.), Handbook of Geophysics and Space Environments, McGraw-Hill, New York, 1965, Section 11.

76. A.V. Jones, Aurora, Reidel, Dordrecht, 1974.

77. B.S. Dandekar, Study of Equatorward Edge of the Auroral Oval from Satellite Observations, AFGL-TR-79-0010 (09 Jan 79).

78. G.V. Starkov, Geomag. i Aeron. 9, 614 (1969).

79. R.E. Sheehan and R.L. Carovillano, J. Geophys. Res. 83, 4749 (1978).

REFERENCES (continued)

80.   B.S. Dandekar, AFGL Report TM-86, in preparation (1982).

81.   B.S. Dandekar, Magnetic Disturbance Statistics from a
      Single Station Q Index Applied to an Actual OTH-B Radar
      Station, AFGL-TR-79-0296 (18 Dec 79).

82.   A.E. Reilly, The Geomagnetic Index Q -- Its Persistence,
      Predictability, and Other Pertinent Properties,
      AFGL-TR-78-0223 (18 Sep 78).

83.   A.L. Cage and E. Gawalick, A Discussion of Geomagnetic
      Indices Kp and Ap, 1932-1971, AFCRL-72-0693 (Nov 72).

84.   R.H. Holzworth and C.-I. Meng, Geophys. Res. Lett. $\underline{2}$,
      377 (1975).

85.   J.A. Whalen, Auroral Oval Plotter and Nomograph for
      Determining Corrected and Geomagnetic Local Time,
      Latitude, and Longitudes for High Latitudes in the
      Northern Hemisphere, AFCRL-70-0422 (27 Jul 70).

86.   J.E. Evans, L.L. Newkirk, and B.M. McCormac, North
      Polar, South Polar, World Maps and Tables of Invariant
      Magnetic Coordinates for Six Altitudes, DASA 2347 (Oct 69).

87.   J.A. Whalen (AFGL), Private communication (1982).

88.   U.S. Naval Observatory Air Almanac, Washington, 1982.

89.   B. Hultqvist and G. Gustafsson, J. Atm. Terr. Phys.
      $\underline{19}$, 246 (1960).

90.   R.L. Carovillano, G.L. Siscoe, R.E. Sheehan, R.H. Eather,
      M.S. Gussenhoven, and N.U. Crooker, Unified Model of
      Auroral Substorm Development, AFCRL-TR-75-0558 (31 Aug 75).

91.   R.H.Eather, J. Geophys. Res. $\underline{84}$, 4134 (1979).

92.   J.E. Maggs and T.N. Davis, Planet. Space Sci. $\underline{16}$,
      205 (1968).

93.   Y. Kamide and J.D. Winningham, J. Geophys. Res. $\underline{82}$,
      5573 (1977).

94.   T.R. Hartz, Particle Precipitation Patterns, in The
      Radiating Atmosphere (ed. B. McCormac), Reidel,
      Dordrecht, 1971.

95.   G. Davidson and C.A. Trowbridge (PhotoMetrics, Inc.),
      Private communication (1982).

REFERENCES (continued)

96. R. Sears, Experimental Visible Spatial Structure, in
     Proceedings of the Second DNA Infrared Data Review Meeting
     (ed's A. T. Stair, Jr. and J. A. Mayo), AFGL-TM-18(1979).

97. A.B. Meinel, Astrophys. J. 111, 555 (1950).

98. J.B. Kumer, A.T. Stair, Jr., N. Wheeler, K.D. Baker and
     D.J. Baker, J. Geophys. Res. 83, 4743 (1978).

99. A. Vallance Jones, Space Sci. Rev's 15, 355 (1973).

100. D.R. Bates and M. Nicolet, J. Geophys. Res. 55, 301 (1950).

101. G. Herzberg, J. Roy. Astron. Soc. Can. 45, 100 (1951).

102. D.L. Baulch, R.A. Cox, R.F. Hampson, Jr., J.A. Kerr,
     J. Troe, and R.T. Watson, J. Phys. Chem. Ref. Data 9,
     295 (1980).

103. M. Nicolet, Planet. Space Sci. 20, 1671 (1972).

104. M. Nicolet, Ann. Geophys. 26, 531 (1970).

105. E.L. Breig, Planet. Space Sci. 18, 1271 (1970).

106. H. Takahashi and P.P. Batista, J. Geophys. Res. 86, 5632
     (1981).

107. V.I. Krassovsky and M.V. Shagaev, Planet. Space Sci. 25,
     509 (1977).

108. J.W. Rogers, R.E. Murphy, A.T. Stair, Jr., and J.C. Ulwick,
     J. Geophys. Res. 78, 7023 (1973).

109. E.J. Llewellyn, B.H. Long, and B.H. Solheim, Planet. Space
     Sci. 27, 1421 (1979).

110. L.M. Kieffaber and A.W. Peterson, J. Atmos. Terr. Phys.
     40, 1339 (1978).

111. E. Battener and J.J. Lopez-Moreno, Planet. Space Sci. 27,
     1421 (1979).

112. J.D. Walker and E.I. Reed, Behavior of the Sodium and Hy-
     droxyl Nighttime Emissions During a Stratospheric Warming,
     NASA/Goddard Space Flight Center Report X-621-76-6 (1975).

113. G. Moreels, G. Megie, A. Vallance Jones, and R.L. Gattinger,
     J. Atmos. Terr. Phys. 39, 551 (1977).

114. G.E. Streit and H.S. Johnston, J. Chem. Phys. 64, 95 (1976).

146

REFERENCES (continued)

115. R.H. Wiens and G. Weill, Planet. Space Sci. 21, 1011 (1973).

116. G. Fiocco and G. Visconti, J. Atmos. Terr. Phys. 36, 583 (1974).

117. G. Moreels, D. Chahrokhi and J.E. Blamont, J. Geophys. Res. 81, 5467 (1976).

118. A.W. Peterson and L.M. Kieffaber, Nature 242, 321 (1973).

119. J.F. Noxon, Geophys. Res. Lett. 5, 25 (1978).

120. B.R. Clemesha, V.W.J.H. Kirchoff, D.M. Simonich, H. Takahashi, and P.P. Batista, J. Geophys. Res. 84, 6477 (1979).

121. F.A Herrero and J.W. Meriwether, Jr., J. Geophys. Res. 85, 4191 (1980).

122. N.N. Shefov, Planet. Space Sci. 17, 797 (1969).

123. P. Berthier, Ann. Geophys. 12, 113 (1956).

124. M. Nakamura, Symposium on the Ionospheric Regions: Proc. Inst. Space Aero. Sci., University of Tokyo, 153 (1974).

125. F.E. Bunn and H.P. Gush, Can. J. Phys. 50, 213 (1972).

126. R.J. Huppi and D.J. Baker, Intensity Variations of Atmospheric Hydroxyl Emissions, AFGL-TR-76-0032 (1976).

127. K.A. Dick, Ann. Geophys. 28, 149 (1972).

128. D.R. Pick, E.J. Llewellyn, and A. Vallance Jones, Can. J. Phys. 49, 897 (1971).

129. G. Moreels, W.F.J. Evans, J.E. Blamont, and A. Vallance Jones, Planet. Space Sci. 18, 637 (1970).

130. K. Labitzke, J. Atmos. Sci. 29, 1395 (1972).

131. M.R. Schoeberl, Rev's Geophys. Space Phys. 16, 521 (1978).

132. N.N. Shefov, Ann. Geophys. 28, 137 (1972).

133. B.P. Sandford and L.R. Doan, Graphs of the Solar Depression Angle from 0° to 90°, AFCRL-69-0543 (1969).

134. R.E. Murphy, J. Chem. Phys. 54, 4852 (1971).

REFERENCES (concluded)

135.   R.E. Goody, Planet. Space Sci. 24, 389 (1976).

136.   T. Watanabe, M. Nakamura, and T. Ogawa, J. Geophys. Res. 86, 5768 (1981).

137.   V.I. Krassovsky, Ann. Geophys. 28, 739 (1972).

138.   R.G. MacDonald, H.L. Buijs, and H.P. Gush, Can. J. Phys. 46, 2575 (1968).

139.   F.H. Mies, J. Molec. Spectrosc. 53, 150 (1971).

140.   G. Herzberg, Spectra of Diatomic Molecules, Van Nostrand Reinhold, New York, 1950.

141.   Cospar International Reference Atmosphere, Akademie-Verlag, Berlin, 1972.

142.   I.L. Kofsky, J.W. Meriwether, Jr., J.W. Schroeder, and R.B. Sluder, Data Reduction and Auroral Characterizations for ICECAP, DNA 3511F (10 Apr 75).

143.   R. Hatfield, T.F. Tuan and S.M. Silverman, J. Geophys. Res. 86, 2429 (1981).

144.   T.F. Tuan, Research in Gravity Waves and Airglow Phenomena, AFGL-TR-76-0296 (1976).

145.   R.D. Sears, Ground-Based Photometric Measurements, DNA 4975 (31 Jan 79).

146.   Ground Support Data Report in Support of Black Brant 18.219-1 Flight, Utah State University (02 Sept 74).

147.   T. Sugiyama, Ionosphere Symposium of the University of Tokyo (Oct 75).

148.   A.W. Peterson, L. Kieffaber, T.F. Tuan, D. Papadopoulos, and R.M. Nadile, submitted to J. Geophys. Res. (1982).

149.   M. Davis and A.V. DaRosa, J. Geophys. Res. 74, 5721 (1969).

150.   M. Herse, G. Moreels, and J. Clairemidi, Appl. Opt. 19, 355 (1980).

151.   G. Moreels and M. Herse, Planet. Space Sci. 25, 265 (1977).

152.   T.F. Tuan, Theoretical Investigation of the Effects of Atmospheric Gravity Waves on the Hydroxyl Emissions of the Atmosphere, AFGL-TR-80-0007 (1979).

153.   L. H. Keiffaber and A. W. Peterson, J. Atm. Terr. Phys. 40, 1339 (1978).

APPENDIX I

NITRIC OXIDE VIBRATIONAL-OVERTONE AIRGLOW

BACKGROUND

The major source of excitation of NO ($v > 2$) in the mid-latitude (non-auroral) daytime upper atmosphere is the reactions of ambient O_2 with N atoms that result from dissociation of N_2 molecules by solar photons and their secondary electrons. At night [N] decreases by about two orders of magnitude in the altitude range where these reactions produce significant dayglow (aeronomy model results, Ref I-1), reducing $+d[NO^\dagger]/dt$ by the same factor.

Other processes that could excite NO ($v > 2$) in the thermosphere occur either less frequently or are unverified. The quenching reaction $N_2(A) + O$, even if it always produces $NO^\dagger$ (which has not been observed experimentally), would result in a lower volume excitation rate at most altitudes. (The concentration of $N_2(A)$ in the atmosphere above $\sim$ 120 km can be estimated from the intensity of dayglow in the Vegard-Kaplan (A-X) bands.) $N(^4S) + O_2(^1\Delta)$ is similarly both infrequent and with uncertain yield of $NO^\dagger$. The column emission rates of solar-pumped electronic bands of NO (β, γ, δ) are so low that the ensuing vibrational cascade is only of the order of 10^{-2} as intense as chemiluminescence. Thermal population of NO to the $\Delta v = 2$ state is also small compared to daytime $N + O_2$, as current atmospheric limb emission models show (Ref I-2); however, when [N] decreases at night it is about the same order of magnitude. Scattering of solar photons from NO, H_2O, and CO_2 molecules also produces less volume emission in the 2.7 μm region above $\sim$110 km altitude, according to limb models (Ref I-2).

This chemiluminous dayglow was in fact considered in the initial treatments of upper-atmospheric $NO^\dagger$-production processes,

Ref's I-3 and I-4. At the time no measurements were available
of [N] or of yields of NO[†] from the reaction of ground-state
and excited N atoms with O_2 (since measured by AFGL). (Ref I-3
presents calculated fractional rates of vibrational excitation
of ambient NO molecules, rather than sky background radiances
in the overtone band.)

INTENSITY CALCULATIONS

We have calculated the zenith and limb brightnesses in the NO
overtone sequence using the midwinter 1400 LT profiles of $[N^4S]$
and $[N^2D + {}^2P]$ from Ref I-5, and the $[O_2]$ and temperature profiles
from the Jacchia 1977 Atmosphere (Ref I-6; about exosphere tempera-
ture about 1020 K). The yield of overtone photons was taken as
1/3 in each reaction of the metastable N atoms with O_2 (calcu-
lated from 0.7% auroral chemiluminous efficiency for NO overtone
radiation, with 1-1/2 $N^2D + N^2P$ atoms produced per ion
pair) and 1/4 in the reactions of ground-state N (which are less
exothermic and thus result in less vibrational excitation).

The zenith radiance in the nitric oxide overtone is then
the sum over altitude
$[O_2](1/4[N^4S]\ 3 \times 10^{-12}\exp(-3150/T) + 1/3[N^2D + {}^2P]\ 5.2 \times 10^{-12})$,
where the numerical figures just after the atomic nitrogen
concentrations are the rate coefficients for reaction of each
species with O_2 to produce NO, and T is the ambient kinetic
temperature at the altitude considered.

The results are as follows. Little radiation is emitted
below 100 km because the natural N-atom concentrations are decreas-
ing rapidly near that altitude. The volume emission rate profile
then shows an increase to a flat maximum (near 2000 photons/cm^3sec
over ~ 40 km) near 160 km. 2/3 of the emission is due to the
$N^2D + O_2$ reaction. (Using a rate coefficient of only 2.7×10^{-12}
cm^3/sec for the $N^2D + O_2$ reaction and earlier altitude
profiles of [N], another group (Ref I-7) has calculated that 1/5
of the NO production, and thus ~1/4 of the overtone emission,

is due to the metastable-state reaction.) The total daytime vertical-column radiance is 1 watt/km^2 ster. Maximum brightness in the limb for the broad layer is then about 30 w/km^2-ster, which is near the 10 w/km^2-ster minimum stated in Section 1.2. (All figures are accurate to only a factor ~2 because of uncertainties in the input concentration profiles.)

By night the predicted precipitous drop in [N] (Ref I-1) reduces the calculated radiances in the NO overtone by about two orders of magnitude below these daytime figures. Some recent rocket profiles at 31°N latitude (Ref I-8) indicate significantly higher nighttime vertical column intensities near 2.6 µm; however, as these radiometer data would result in factor-100 higher nightglow radiances in the N^2D-^4S airglow doublet at 0.5200 µm than are observed, and in addition fail to show the accepted hydroxyl-fundamental profile, they are subject to question. (None of AFGL's rocket probe data apply unambiguously to measuring the NO overtone nightglow intensity above ~ 110 km altitude.)

DISCUSSION

It is instructive to compare these figures to other radiant intensities in the 2-1/2 - 3-1/3 µm wavelength (3000 - 4000 cm^{-1}) band. The mean nighttime hydroxyl fundamental is 13 w/km^2 ster in the zenith and a maximum of 1000 w/km^2 ster in limb projections (Section 3). If these intensities a factor 2 or 3 lower by day, the zenith radiance of OH would be only about a factor 5 higher than the NO overtone. Note that the altitude of the OH[†] layer is some 80 km below the peak of NO Δv >2 airglow.

The "thermal" (atom-interchange) radiance of the NO (2,0) band is no more than 1/2 w/km^2 ster by day and 1/20 w/km^2 ster by night at tangent altitudes between 60 and 200 km (using data in Ref I-2). Thus the interchange process produces much less overtone radiation than chemiluminescence in the daytime, but is comparable in the nighttime atmosphere, Referring to Fig 5, we see that the

daytime limb radiances of all the CO_2 and H_2O bands near 2.7 μm fall below 30 w/km^2 ster at about 120 km tangent altitude. Thus the backgrounds from these other features are lower than NO $\Delta v = 2$ at intercept altitudes above about 120 km.

The $N + O_2$ reactions of course also produce fundamental-band sequence photons, which make a small contribution to the daytime radiance at wavelengths above 5.3 μm. The thermal background in the (1,0) band at 150 km tangent altitude is broadened to a spectral width of about 300 cm^{-1} by the atmosphere's high temperature (Ref II-2), and so extends well into the lower-wavenumber region of the chemiluminescence cascade spectrum at lower altitude and temperature (shown in Fig 14a). This limb radiance is 1000 w/km^2 ster by day, which is an order of magnitude higher than the fundamental-sequence radiance from chemiluminescence with the yield estimated as ~3x that in the overtone sequence (refer to the discussion in Section 2.6.1), which would be ~90 w/km^2 ster. Considering the intensity and broadening of the calculated thermal emission in the NO fundamental, the airglow component of the sequence could be expected to be detectable in only a narrow wavenumber interval near 1700 cm^{-1} (5.9 μm), if at all.

As the concentrations of N and O_2 in the (non-auroral) thermosphere do not exhibit substantial irregularities over short periods and distances, little radiance structure viewing through the thick emitting layer would be expected. Although clutter is minimal, since the N-atom profiles are strongly dependent on solar zenith angle and geomagnetic activity (as shown in Ref's I-9 and I-10), the magnitude of this infrared background will vary with latitude and season, as well as diurnally.

SUMMARY

By day chemiluminescence in the nitric oxide overtone sequence is the dominant 2-1/2 - 3-1/2μm-band airglow at thermospheric limb intercepts. Its peak radiance is at least an order of magnitude less than that of the hydroxyl and sunlight scattering from H_2O and CO_2 molecules below ~100 km, so that it would not be readily detectable in zenith projections from below these layers. By night the NO-overtone limb background falls to less than 1 w/km^2 ster. Although the airglow's mean intensity varies with geophysical parameters, little short-period or short-wavelength structure is expected.

REFERENCES

I-1.   D. Strobel, J. Geophys. Res. $\underline{76}$, 2441 (1971).

I-2.   T. Degges and H.J.P. Smith, A High Altitude Infrared Radiance Model, AFGL-TR-77-0271 (30 Nov 77).

I-3.   T. Degges, Appl. Optics $\underline{10}$, 1856 (1971).

I-4.   D.F. Strobel, D.M. Hunten, and M.B. McElroy, J. Geophys. Res. $\underline{75}$, 4307 (1970).

I-5.   P.G. Richards, D.C. Torr, and M.R. Torr, J. Geophys. Res. $\underline{86}$, 1495 (1981).

I-6.   L.G. Jacchia, Smithsonian Astrophysical Report 375, Cambridge, MA (1977).

I-7.   D.W. Rusch, A.I. Stewart, P.B. Hays, and J.H. Hoffman, J. Geophys. Res. $\underline{80}$, 2300 (1975).

I-8.   S. Hayakawa, K. Ito, T. Matsumoto, H. Murakami, K. Noguchi, T. Ono, and K. Uyama, J. Geomag. Geoelectr. $\underline{32}$, 691 (1980).

I-9.   W. Kohnlein, D. Krankowsky, P. Lammerzahl, W. Joos, and H. Volland, J. Geophys. Res. $\underline{84}$, 4315 (1979).

I-10. M.J. Engebretson, J.A. DeFreese, and K. Mauersberger, J. Geophys. Res. $\underline{85}$, 2165 (1980).

APPENDIX II

INFRARED AIRGLOWS FROM O_3 AND NO_2

INTRODUCTION

In addition to the chemiluminescence of OH[†] (Section 3) and NO[†] (Appendix I) in the wavenumber regions indicated in Fig 3, some further short wavelength-infrared airglow is emitted in the intercombination and fundamental vibrational bands of O_3 and NO_2 molecules excited by exothermic reactions of upper-atmospheric species:

$$O + O_2 + M \rightarrow O_3^{†} + M \qquad + 1.05 \text{ eV}$$
$$NO + O \ (+ M) \rightarrow NO_2^{*} \ (+ M) \qquad + 3.12 \text{ eV}$$
$$NO + O_3 \rightarrow NO_2^{*,†} + O_2 \qquad + 2.07 \text{ eV.}$$
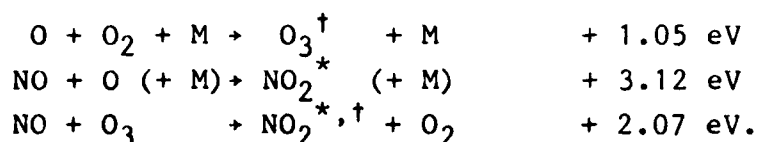
Little direct information exists on the spectral distribution and absolute photon yields from these reactions, or on the altitude dependence of effects of collisions; in fact the 2-1/2-7 µm airglows have not been detected in the atmosphere. Assessments of the chemiluminescent background intensities must further consider the natural -- and incompletely understood -- variability of the reactant concentrations, in particular NO, which varies diurnally and with solar activity and increases at high latitudes as a result of dissociation of N_2 molecules by auroral particles (Ref II-1; see also Fig 13). Because of these uncertainties calculations of spectral radiances of the zenith and limb infrared airglows from O_3 and NO_2 should be considered as largely speculative.

O_3 AIRGLOW

AFGL laboratory experiments (Ref II-2) have shown that the third body stabilized reaction of O with O_2 has a high efficiency

for production of vibrationally-excited $O_3(\nu_3)$, which was found
to radiate in the the ~ 9.5-11.5μm wavelength region. The
WOE code for computing backgrounds of the artificially-disturbed
upper atmosphere (Ref II-3; see also Fig A-1 of Ref II-4) predicts
that along with ~1 ν_3 (+ ν_1 near 9.1μm) photon from each re-
combination reaction, radiation is emitted in blends of O_3 inter-
combination bands with local broad maximums, as shown in Table
II-1. The offset of these emission peaks to wavenumbers below

Table II-1. O_3 Intercombination-Band Radiation (Model Predictions)

Wavelength of Peak	Wavenumber, FWHM	Band	Photons/Reaction
5.7 μm	1760 ± 80 cm^{-1}	$\nu_2 + \nu_3$ & $\nu_1 + \nu_2$	0.2
5.0 μm	2000 ± 100 cm^{-1}	$\nu_1 + \nu_3$ (?)	0.15
3.85μm	2600 ± 125 cm^{-1}	$\nu_1 + \nu_2 + \nu_3$	0.01

the band centers ($\nu_1 + \nu_3$ is at 2110 cm^{-1} and $\nu_1 + \nu_2 + \nu_3$ at
2779 cm^{-1}) is thought to be an effect of anharmonicity of the
O_3 molecule, which is assumed to be initially excited to a dis-
tribution of levels of each vibrational mode (Ref II-3).

The ~5.0-5.7μm feature was not detectable in the spectra
of the auroral limb taken from the HIRIS rocket, which clearly
showed (as did AFGL's SPIRE experiment) the ν_3 emission enhanced
over thermal (Ref II-5); and furthermore in the laboratory measure-
ments (Ref II-2) the O_3 ν_2 excitation (bands near 14μm)
was found to be weak compared to WOE's predictions. In con-
sequence of these observations (and in recognition of the fact

that WOE is a worst-case sky backgrounds model) we have chosen
to reduce the yields in the emission peaks centered at 5.0 and
5.7 μm to 0.1 photon per recombination reaction. The photon
emission rate in the feature near 3.8 μm would then be 1/10 that
of these longer-wavelength bands. As Fig 4 shows, the thermal
radiance of the atmosphere is small near 3.8 μm (2600 cm^{-1}) and
high in the ~5-6 μm (1600-2100 cm^{-1}) region.

The column emission rates in the zenith are then the sum
over altitude

$$(0.1 \text{ or } 0.01) \times \sum \{[O]\ [O_2]\ [M] \times 1.1 \times 10^{-34} \exp(510/T)\},$$

where T is again the temperature in K and the last term is the
recombination rate coefficient (Ref II-6). We cut off the
summation at 90 km altitude, below which $O_3{}^\dagger$ has a high probab-
ility of collisional deactivation by N_2 and O_2 (Ref II-5); that is,
we have taken the altitude dependence of total photon yield as the
same step function for each feature (although collisions would be
expected to change the spectrum distribution in the real atmosphere).
The zenith column intensity is moderately sensitive to the choice
of this cutoff altitude, as the rates are proportional to the
square of the atmosphere's density; the rate coefficient changes
slowly with altitude near 90 km, and the very sharp decrease in
[O] effectively cuts off chemiluminescent emission below 80 km.

Applying the concentration and temperature profiles from the
Jacchia 1977 model atmosphere (Ref II-7), we calculate a zenith
radiance of 1/2 w/km^2 ster in each of the larger spectrum peaks in
the O_3 airglow. Most of this emission originates from a ~5 km
altitude slice just above our assumed 90 km cutoff. While the
radiance of course depends on the O-atom concentration profile
selected, it does not vary significantly with solar elevation,
since the diurnal change in [O] is very small above 85 km altitude
(the other reaction parameters also do not change significantly).

As the largest van Rhijn path length increase from the narrow
emitting layer is of the order of 100, the highest limb radiances
in the spectrum peaks would be ~50 w/km^2 ster or ~0.2 w/km^2 ster-

cm^{-1} at 90 km tangent intercept altitude. This is comparable
to the thermal spectral radiance at 80 km (shown in Fig 4),
although well below the NO (1,0) band peak near 1800 cm^{-1} (5.4μm)
that lies between the two O_3 maximums. By 100 km intercept the
chemiluminescent limb radiances have decreased to 0.01 w/km^2 ster
cm^{-1}, which is about an order of magnitude below the thermal back-
grounds calculated in Ref II-8 (the source of Fig 4); and at 110 km
tangent altitude the three-body dependence of volume excitation rate
has reduced these airglow intensities by another two orders of
magnitude, so that they are far less than thermal. Thus with the
(uncertain) aeronomy model that we have adopted the ~5.0-5.7μm O_3
chemiluminescence would be a significant sky background over only
a narrow range of tangent altitudes.

Since the weaker emission near 2600 cm^{-1} lies in an atmos-
spheric window, despite its being a factor-10 less intense this
feature would be by far the dominant sky background at tangent
intercept altitudes from about 85 km to 120 km (where Ref II-8
shows some comparably intense thermal emission). Nonetheless its
radiance is below ~15 w/km^2 ster at all intercepts, which is
close to the minimum suggested in Section 1.2; compare the maximum
radiance of the OH fundamental-bands airglow, 1000 w/km^2 ster.

We note that the atmospheric-wave and atomic oxygen-trans-
port phenomena that underlie the short-period and short-spatial
wavelength irregularities in hydroxyl emission (Section 3.5) would
have generally similar effects on the radiances of these low-
altitude (i.e., originating below the turbopause) ozone airglow
bands.

NO_2 AIRGLOW

These atmosphere-dynamics and turbulent-mixing effects would
also cause stucturing of airglows from NO + O and NO + O_3 reactions.

The 2-1/2 - 7μm emission from NO_2 is described in Table II-2.
(These spectrum data come from more recent sources, and differ
substantially from the inputs to WOE (given in Ref II-4)).

Table II-2. NO_2 Intercombination and Fundamental
Radiation Spectrum (Predicted)

Reaction	Wavelength of Peak(μm)	Wavenumber, FWHM (cm^{-1})	Band	Photons/ Reaction
$NO + O$	3.76	$2655 + 185, -115$	$\nu_1 + \nu_3,\ 2\nu_3$	0.06 to 0.1[*]
$NO + O_3$	3.62	$2740 + 125, - 90$	sequences	0.37
$NO + O$	6.2	1618 ± 120	ν_3	1 to 1-1/2[*]
$NO + O_3$	6.2	1618 ± 120	fundamental	3

[*] In the unstabilized recombination reaction.

The yield from $NO + O$ in the vibrational band sequence near
3.7μm is taken from a laboratory measurement (Ref's II-9,II-10)
on third-body stabilized reactions known to have total quantum
efficiency very close to 1 for electronic band emission (the
"yellow-green afterglow"). This spectrum feature is believed to
be due principally to $\nu_1 + \nu_3$ (each $\Delta v = 1$) intercombination
bands, with possibly some ν_3 overtone (Ref II-10). We increased
the measured emission probability by a factor 1-1/2 in two-body
recombinations of NO with O, on the basis of theoretical indica-
tions that it should be somewhat larger when the collision
complex is unstabilized.

The rather high photon yield in the ν_3 fundamental bands
was estimated from two arguments (Ref II-11). First, the ν_3
radiative relaxation rates are large relative to $\nu_1 + \nu_3$
(147/sec for the 001 $\rightarrow$ 000 transition compared to 13/sec for
101 $\rightarrow$ 000) and $2\nu_3$. Second, virtually all the photons emitted
in electronic bands of NO_2 from the two reactions h..ve energies
less than the exothermicity (the short-wavelength cutoff for NO +
O is 0.3875μm), which indicates that the NO_2 molecules are left
with substantial vibrational excitation after radiating the well
known recombination "continuums." The laboratory emission near

3.7μm from NO + O_3 is shifted to shorter wavelengths (Ref II-10); since less energy is available for vibrational excitation, we have estimated a lower yield of v_3 fundamental photons from these reactions (93% of which result in NO_2 in the ground electronic state of NO_2, Ref II-12). In practice, NO + O_3 re-arrangement reactions make only a small contribution to the total infrared radiances.

The effective two-body rate coefficient for NO + O recombination decreases with pressure above ~50 km altitude (Ref II-13). In the absence of better information we adopt the (temperature)$^{-2}$ dependence observed in the high-pressure (third-body-stabilized) limit, and as noted we have also increased the photon yields from the unstabilized reactions. For NO + O_3, we apply the rate coefficient 2.1×10^{-12} exp[-1450/T] from Ref II-4. We adopt again the Jacchia model atmosphere, along with the altitude profiles of [NO] (which is an average of observations) and [O_3] (which differ by about an order of magnitude between day and night) that are used in AFGL's model of thermal radiance (Ref II-8). For reference, the input data for our calculation of NO_2 chemiluminescence are given in Table II-3 (the k's are rate coefficients for the two reactions). We used the "average" NO profile given in Ref II-8; the factors-10 variations about this mean that have been measured (as reviewed in Ref II-14) result in correspondingly large excursions from the mean airglow radiances calculated.

Zenith column emission rates in the two airglow peaks in Table II-2 are then again the sum over altitude
$\sum$[NO] {[O] x(Rate coefficient x photons/reaction from Table II-3)
+[O_3] x(Rate coefficient from Table II-3 x 0.37 or 3
photons/reaction) }.
In view of the low deactivation cross-sections reported in Ref II-10 collisional quenching can be neglected at the altitudes where NO_2 is produced. The emission is dominated by the NO + O

Table II-3.   Input Data for NO_2 Airglow Calculation

Altitude km	80	90	100	110	120	135
k -NO+O, cm^3/sec	6×10^{-17} (0.07)*	4×10^{-17} (0.08)	2×10^{-17} (0.09)	1×10^{-17} (0.1)	5×10^{-18} (0.1)	2×10^{-18} (0.1)
k -NO+O_3 cm^3/sec	2×10^{-15}	1×10^{-15}	1×10^{-15}	5×10^{-15}	3×10^{-14}	1×10^{-13}
[O], cm^{-3}	3×10^{10}	2×10^{11}	5×10^{11}	2×10^{11}	1×10^{11}	4×10^{10}
[NO], cm^{-3}	8×10^6	1×10^7	4×10^7	5×10^7	3×10^{7}**	8×10^{6}**
[O_3] night, cm^{-3}	2×10^8	2×10^8	3×10^7	2×10^6	2×10^5	2×10^4
[O_3] day cm^{-3}	2×10^7	4×10^7	5×10^6	3×10^5	3×10^4	3×10^3

*3.7μm-band photons per reaction.   The number of 6.2μm-band photons/reaction was similarly increased from 1.1 to 1.5 between 80 and 100 km.

**Night; noon daytime 5×10^7 and 3×10^7.

recombinations, NO + O_3 contributing less than 1/20 of the vertical column radiance from a flat excitation profile below 110 km.   Total zenith and maximum limb radiances (near 95 km tangent altitude) are

0.002 and 0.1 w/km^2 ster in the 3.7 μm peak   and
0.02   and   1 w/km^2 ster in the 6.2 μm peak.

These mean backgrounds are well below the 10 w/km^2-ster threshold suggested in Section 1.2.   On the other hand adopting the higher-concentration altitude profiles of NO and O, in particular those reported for high latitudes, would increase them by about

a factor 50, to 5 and 50 w/km^2 ster (or ~0.015 and 0.15 w/km^2-
ster cm^{-1}) respectively in the limb. Like the 3.8μm
(~2600 cm^{-1}) chemiluminescence of O_3, the shorter-wavelength NO_2
peak is weak compared to planned measurements experiments
thresholds but strong compared to the upper atmosphere's thermal
emission. With the yield of ν_3-fundamental photons adopted,
the airglow radiance in the 6.2μm band is more intense than
the thermal (largely, H_2O) emission shown in Ref II-8 above
~90 km tangent intercept altitude. Moreover, it would be substan-
tially brighter in the apparently not-infrequent cases that
[NO] and [O] are significantly enhanced over the averages listed
in Table II-3.

SUMMARY

Because of the large uncertainties in the photon yields and
emission spectra and the natural variability of reactant concen-
trations, intensities of the infrared airglows from O_3 and NO_2 can
only be approximated. Clearly, further data are needed on excita-
tation/deexcitation rates, species profile systematics, and
actual limb radiances. With the aeronomy and model atmosphere
that we have adopted, chemiluminescence from these molecules
results in limb backgrounds at least comparable to thermal
over broad wavenumber regions; in particular, both $O_3{}^\dagger$ and $NO_2{}^\dagger$
fill in the the atmospheric window near 2600 cm^{-1}.

Spatial and temporal irregularities of these relatively
low-altitude airglows at all scales would be expected to be
generally similar to those of hydroxyl. The NO_2 vibrational
band intensities are increased by auroral activity, with a
smaller effect on O_3 because charged-particle impacts result
in only a small fractional increase in concentration of O atoms.
The long time scales of the recombination-airglow reactions
(~days), however, washes out the initial structure of auroral-
particle input.

REFERENCES

II-1. J.C. Gerard and C.A. Barth, J. Geophys. Res. 82, 674 (1977).

II-2. W.T. Rawlins, G.B. Caledonia, and J.P. Kennealy, J. Geophys. Res. 86, 5247 (1981).

II-3. T.L. Stephens (Kaman-Tempo), Private communication (1982).

II-4. D.H. Archer, Further Requirements for Improved Prediction Capability: LWIR, DNA 5471F (31 Oct 80).

II-5. B.D. Green, W.T. Rawlins, and G.E. Caledonia, Physical Sciences, Inc., Report TR-296 (Feb 82).

II-6. R.E. Huie, J.J. Huron, and D.D. Davis, J. Phys. Chem 76, 2653 (1972).

II-7. L.G. Jacchia, Smithsonian Astrophysical Observatory Report 375, Cambridge, MA (1977).

II-8. T.C. Degges and H.J.P. Smith, A High Altitude Radiance Model, AFGL-TR-77-0271 (30 Nov 77).

II-9. M.F. Golde, A.E. Roche, and F. Kaufman, J. Chem, Phys. 59, 3953 (1973).

II-10. M.F. Golde and F. Kaufman, Chem. Phys. Lett. 29, 480 (1974).

II-11. F. Kaufman (University of Pittsburgh), Private communication (1982).

II-12. P.N. Clough and B.A. Thrush, Trans. Faraday Soc. 63, 915 (1967).

II-13. F. Kaufman, The Air Afterglow Revisited, in Chemiluminescence and Bioluminescence (ed's Cormier, Hercules, and Lee), Plenum, New York, 1973.

II-14. W. Swider in Proc. NATO Advanced Study Institute on Atmospheric Ozone (ed. A.C. Aikin), FAA-EE-80-20 (1980).

APPENDIX III

AURORAL INPUT-INTENSITY DISTRIBUTION DATA
FROM DYNAMICS EXPLORER

INTRODUCTION

As noted in Section 2, the spatial and temporal distribution of auroral-particle energy input into measurements sight paths is subject to considerable uncertainty because of the sparsity of observational data. (The extreme complexity of the underlying geophysics precludes development of plausible predictive models.) The data base to date consists principally of scanning-images excited by particle impact taken from the sun-synchronous DMSP satellites (the radiances are only semi-quantitative, and are restricted to the limited (night) time period during which the satellites pass over auroral latitudes), and from the ISIS satellites (also low earth orbiting and sensitive only at night); nadir UV radiometry from the S3-4 satellite (on which more presently); groundbased all-sky camera network photographs; some surveys from aircraft with all-sky cameras and ionosphere sounders; and energy spectrums of the incoming particles measured from low altitude orbiting satellites (including DMSP and ISIS).

A systematic and self-contained set of energy input flux data is now becoming available, from imaging photometers on NASA's Dynamics Explorer 1 Satellite (Ref's III-1, III-2). The critical features of the experiment are

1) a highly eccentric, Molniya-type orbit initially at 90° inclination, which maintains the satellite over high latitudes for most of each orbit when its apogee is near a geomagnetic pole;

2) measurement of radiance distributions over an angular field larger than that subtended by the auroral oval in six auroral emission bands, including some in the ultraviolet from

163

which particle energy input rates in the
sunlit atmosphere can be determined.
This combination of image field and spacecraft location provides
nearly continuous (actually, "time-lapse", as ~10 min is needed
to compose an image) monitoring of the particle energy input
occurrences and their spatial correlation over most or all of
the oval, albeit at some sacrifice of spatial resolution. The
duration of the measurements is determined by the selected
satellites orbital precession and expected lifetime.

PERFORMANCE CHARACTERISTICS

Dynamics Explorer is a followon to NASA's Atmospheric Explorer
and International Sun-Earth Explorer satellite programs. It is
designed to probe simultaneously the magnetosphere and ionosphere,
to study coupling between the two regions and in particular the
mechanism by which the energetic charged particles that excite
optical and infrared aurora are injected into the atmosphere.
The two spatially-coordinated DE spacecraft were launched from
Western Test Range at 0255 PDT on 03 Aug 81; DE-2 is in a low
altitude ("ionosphere") orbit (1012 x 305 km, ~101 min period),
and DE-1 ("magnetosphere") in a coplanar 23,100 km (4.6 earth
radii) x 570 km orbit with ~440 min period.

Three $1/4°$ x $1/4°$-IFOV photometers on DE-1 (Spin-Scan
Auroral Imagers, or alternatively, Global Auroral Imaging Photo-
meters, described in Ref III-2) compose $30°$ x $120°$-field radio-
metrically calibrated images. They are programmed for sensitivity
to the $0.3914\mu m$ N_2^+ First Negative bands, $0.5577\mu m$ OI line, $0.6300\mu m$
OI line, $0.1216\mu m$ hydrogen Lyman-α, OI permitted lines between
0.130 and $0.136\mu m$, or N_2 Lyman-Birge-Hopfield bands between about
0.13 and $0.17\mu m$. (Other wavelength-isolating filters can be
cycled into position to perform non-auroral measurements.) The
sunlit-sky background in the last two vacuum ultraviolet-
sensitivity bands is sufficiently low and spatially unvarying

(at least away from the atmosphere's limb) that particle energy fluxes are measurable by day.

Intensity threshold without coadding picture elements is about 1 kilorayleigh (10^9 photons/sec cm^2-column). Spatial resolution -- footprint of the photometers' fields -- is is 40 km when DE-1 is at 10,000 km altitude and 115 km (which is 1° of latitude) at apogee. Thus spatial and intensity resolution have been traded off against maintaining nearly continuous coverage of the auroral oval (when apogee is over high latitudes). Some early DE-1 scanning images of substorm development that were presented at an AGU meeting (Ref III-1), clearly show the instrument's expected low spatial resolution and wide angular coverage.

DE-1's apogee was placed initially over the north geographic pole. Its orbit processes south at about 0.3° of latitude per day, which moves the apogee over the south pole by April 1983. Since the spatial distribution of charged particle input is similar in conjugate hemispheres, occurrence statistics from the southern auroral oval apply also to the northern oval. Occurrence data will be available for all local times, as the orbital period is not commensurate with the length of a day. We note that a three-year lifetime of DE-1 would allow it to survey auroral input distributions over about one quarter of a solar cycle.

COMPLEMENTARY DATA FROM S3-4

UV atmospheric emissions have also been recently measured by narrow-field photometers and spectrometers on USAF's polar-orbiting satellite S3-4 (Ref III-3), at wavelengths at which daytime aurora is detectable. These data have much higher spatial and intensity resolution because of the vehicle's low orbital altitude (<260 km); however, they are limited to the times of its sun-synchronous crossings of the ovals and of course lack the longitudinal coverage provided by DE-1's cross-

track scan. (That is, like particle counters the photo-
meters compose only one-dimensional "images."). Since S3-4
crosses the ovals near 1030 and 2230 LT it returns information
on the probabilities of input flux on both the dayside and the
(better-known) local midnight sector. It is also a source of
data on spatial structure at <1 km scale, which complement the
lower-resolution, more continuous radiance distributions from
Dynamics Explorer.

The auroral input flux rate is closely proportional to the
column intensities of the N_2 Lyman-Birge-Hopfield bands as
well as the N_2^+ First Negative bands. The First Negative bands
are of course detectable only at night, and their radiance distri-
bution is contaminated by backscattering from the lower atmosphere
and earth's surface. In contrast the ultraviolet L-B-H bands from
aurora become detectable against the zenith-sunlit sky when the
particle input rate is greater than about 2000 w/km^2, and
their radiances have only a negligible backscatter component.
Further, the relative intensities of individual L-B-H bands (and
of the OI lines) provide a measure of the characteristic energy
of the incoming particles (Ref III-4; because of the wavelength
dependence of VUV absorption by atmospheric O_2). At night
mean emission altitudes (for measuring energy input into into
slant sight paths) can be determined from the 0.6300 μm/0.3914 μm
column intensity ratios, as described in Section 2.4.1. Similarly,
the altitude profiles of energy deposition in the daytime can be
assessed from DE-1's ultraviolet image data.

ADMINISTRATIVE, SUMMARY

The Dynamics Explorer program is managed by NASA/Goddard
Space Flight Center. Data from the Spin-Scan Auroral Imager will
be treated separately from those from the 14 in-situ measuring,
non-imaging instruments on the two satellites; they are to be
preprocessed as described in Ref III-2 and put on microfilm (and

other formats) for distribution to the program scientists. An
analysis of these imaging-photometer data from periods when
DE-1's apogee is at high northern or southern latitudes would
serve to determine probabilites of occurrence of auroral input
flux with time resolution of a few min and spatial resolution
(footprint) about 1 degree square at virtually all magnetic times.

REFERENCES

III-1. Trans. Am. Geophys. Un. 61, (1980) (general description
        of satellites); Trans. Am. Geophys. Un. 62, 995-6 (1981)
        (Fall 1981 meeting abstracts outlining preliminary results).

III-2. L.A. Frank, J.D. Craven, K.L. Ackerson, M.R. English,
        R.H. Eather, and R.L. Carovillano, Space Sci. Inst. 5,
        369 (1981).

III-3. R.E. Huffman, F.J. LeBlanc, J.C. Larrabee, amd D.E. Paulsen,
        J. Geophys. Res. 85, 2201 (1980).

III-4. D.J. Strickland, J. R. Jasperse, and J.A. Whalen, Trans.
        Am. Geophys. Un. 62 977 (1981).

DATE
LME